Chapter 23

Coherent Radio Emissions Associated with Solar System Shocks

Iver H. Cairns

Abstract Shock waves are associated with multiple powerful coherent radio emissions within the heliosphere and local interstellar medium. The radio emissions definitely driven by shocks include interplanetary type II (solar radio) bursts,"foreshock" emissions from upstream of Earth's bow shock, and rare emissions from corotating interaction regions (CIRs). Emissions likely driven by shocks, but without definitive observational evidence, include coronal type II bursts, the 2–3 kHz emissions from the outer heliosphere, and drifting pulsating structures from the deep corona. Analogous emissions are also predicted, but not yet observed, for mini-magnetospheres and associated bow shocks on the Moon and for moons like Ganymede, the foreshocks of other planets, particularly Mercury and Jupiter, and supernovae. All these emissions are produced near the electron plasma frequency f_{pe} and/or $2f_{pe}$ via the so-called "plasma emission" mechanism or linear mode conversion, two of the four coherent radio emission mechanisms observed to date. In each case the theoretical interpretation requires coupling of multiple physical processes from microscales to macroscales. Microscale physics includes the time-varying magnetic overshoots of reforming shocks, electron reflection and acceleration at shocks, growth of Langmuir waves in the upstream foreshock, and the linear or nonlinear conversion of Langmuir energy into radio emission at f_{pe} and/or $2f_{pe}$. Intermediate scale physics includes the creation of ripples on the shock on scales of order the decorrelation length of the magnetic field, as well as scattering of the radiation by density irregularities. Macroscale physics includes 3D spatiotemporal variations of the plasma and the shock motion, as well as integration of emission from individual shock ripples over the entire shock. This chapter is a comprehensive review of the field, starting with observations of the emissions definitely and probably driven by shocks. Existing theory is then summarized in some detail, followed by detailed reviews of the observation and theory of type II bursts (both coronal and interplanetary) and the 2–3 kHz emissions from the outer heliosphere, including descriptions of the unresolved issues. The discussion focuses on limitations of the theory and existing observations and ways to address them. The overall conclusions are that the basic theory (electron shock acceleration, development of an electron beam, growth of Langmuir waves, and production of f_{pe} and $2f_{pe}$ radiation for a macroscopic, rippled, shock) appears to explain the primary observations semiquantitatively, that many observational details and theoretical limitations remain unresolved, and that the next ten years ought to be an exciting time that sees theory and observations brought together quantitatively.

23.1 Introduction

Energy releases in plasmas are observed to have multiple effects, including the acceleration or heating of some of the plasma particles and, sometimes, bulk motion of the entire plasma. Via coherent and incoherent processes, accelerated and heated particles can produce radiation across the electromagnetic spectrum, from X-rays to radio waves, that can escape the

I.H. Cairns (✉)
School of Physics, University of Sydney, Sydrey, NSW 2006, Australia
e-mail: i.cairns@physics.usyd.edu.au

M.P. Miralles, J. Sánchez Almeida (eds.), *The Sun, the Solar Wind, and the Heliosphere*, IAGA Special Sopron Book Series 4, DOI 10.1007/978-90-481-9787-3_23, © Springer Science+Business Media B.V. 2011

source plasma and propagate large distances to remote observers. They can also produce plasma waves that do not escape the plasma, such as electrostatic waves near the electron plasma frequency and low-frequency magnetohydrodynamic (MHD) waves, whose energy can be channelled into escaping radiation and into heating and/or accelerating other plasma particles. Shocks are produced if the bulk plasma motion is faster than the group speed of a wave mode subject to nonlinear steepening, waves in this mode are driven by the flowing plasma interacting with another plasma, and the system allows sufficient time for nonlinear steepening into a shock.

Shocks are fundamentally important in laboratory, space, and astrophysical plasmas. They accelerate and reflect some plasma particles, with multiple consequences including: (i) production of high energy particles relevant to space weather, solar flares, and cosmic rays; (ii) particle distributions that drive (iii) high levels of plasma waves via instabilities and (iv) radio emissions, sometimes via coherent processes and sometimes by incoherent processes like gyrosynchrotron emission. Shocks also heat the plasma, in part directly by the steady-state electric field associated with the shock structure (Scudder et al. 1986; Burgess 1995; Hull et al. 1998, 2000; Krasnoselskikh et al. 2002) and in part by damping of waves excited by particles moving through the shock or accelerated by it (Tidman and Krall 1971; Kennel et al. 1985; Burgess 1995; Lembege et al. 2004; Scholer and Matsukiyo 2004; Matsukiyo and Scholer 2006; Hellinger et al. 2007; Yuan et al. 2009; Lembege et al. 2009). Depending on the temperature, heating can produce optical, UV, and X-ray signatures observable remotely. Shocks also introduce spatial and temporal inhomogeneities in the density, velocity, temperature, electric field, and magnetic field in the plasma, often by factors of 4 or more. They also change the plasma's entropy. This chapter focuses on items (i)–(iv) above in connection with coherent radio emissions produced by shocks in our solar system. More details of the physics of shock waves are provided in Section 23.2 below.

Two of the solar system's three most powerful radio emissions are associated with shock waves. The most powerful are the 2–3 kHz radio emissions observed by the Voyager spacecraft: they are believed to be produced beyond the heliopause by a shock wave driven in front of coronal mass ejections (CMEs) and other solar disturbances that have combined into a so-called Global Merged Interaction Region (GMIR) (Kurth et al. 1984; Gurnett et al. 1993; Cairns and Kaiser 2002; Cairns 2004). The heliopause is the plasma discontinuity between the solar wind's "termination shock" and the solar system's "bow shock" (or bow wave) that separates the shocked solar wind plasma from the (likely shocked) plasma of the very local interstellar medium (VLISM) (Zank 1999). Type II solar radio bursts, the weakest of the three, are produced in the Sun's corona and the solar wind (Wild and McCready 1950; Wild et al. 1963; Cane et al. 1982; Nelson and Melrose 1985; Cairns 1986a; Reiner et al. 1998; Reiner 2000; Robinson and Cairns 2000; Cane and Erickson 2005). Interplanetary type IIs are definitely associated with shocks driven ahead of fast CMEs (Bale et al. 1999), while coronal type IIs are believed to be produced by either blast wave shocks (associated with flares) or CME-driven shocks. The last of the three, type III solar radio bursts, are produced in the corona and solar wind by fast streams of electrons accelerated in solar flares and have no known association with shocks (Wild and McCready 1950; Wild et al. 1963; Suzuki et al. 1985; Robinson and Cairns 2000; Cane et al. 2003). At least another five observed or predicted solar system radio emissions are associated with shocks and discussed below. These include the f_p and $2f_p$ radiation associated with Earth's bow shock, formed as a result of the solar wind's interaction with Earth's magnetosphere, which is likely the emission most amenable to definitive observational testing of theory.

The nonthermal radio emissions of interest in this review are produced by coherent mechanisms. One line of evidence for this is provided by the brightness temperature T_b of the radiation being larger than the electron temperature T_e of the emitting plasma. Here

$$T_b = \frac{v_\phi^2}{2k_B f^2}\frac{F(f)}{\Delta\Omega}\,, \tag{23.1}$$

where v_ϕ is the phase speed of the waves ($\approx c$ except when the wave frequency $f \lesssim 2f_p$), k_B is Boltzmann's constant, $F(f)$ is the flux density (in W m^{-2} Hz^{-1}), and $\Delta\Omega$ is the solid angle of the radio source. The second line of evidence is that the emissions are narrowband, thereby not having the broadband spectrum over orders of magnitude in frequency expected for synchroton and other single-particle emission mecha-

nisms when observed at intensities much larger than the instrumental detection thresholds.

The basic model for coherent radio emissions associated with shocks, which applies to both type II bursts and the 2–3 kHz outer heliospheric radio emissions, is illustrated in Fig. 23.1 in the rest frame of the shock. The plane in Figure 23.1, defined by the upstream plasma flow velocity **u** and magnetic field vector $\mathbf{B}_u$, is a cut of the three-dimensional (3-D) source. The "foreshock" regions are found upstream of the shock but downstream from the magnetic field line tangent to the shock (the so-called tangent line). As explained below, electrons reflected by (or leaked upstream from) the shock are found in the foreshock regions and naturally develop "beam" distributions which are peaked at a non-zero velocity parallel to the magnetic field (more properly the "reduced" distributions, which are integrated over perpendicular velocity space). These beam distributions are unstable to the growth of electrostatic Langmuir waves (Filbert and Kellogg 1979; Cairns 1986a, 1987a, 1987b; Fitzenreiter et al. 1990). Langmuir waves have frequencies close to the electron plasma frequency

$$f_{pe} = \frac{1}{2\pi}\left(\frac{n_e e^2}{m_e \varepsilon_0}\right)^{1/2}, \qquad (23.2)$$

where n_e is the electron number density, e the electron charge, m_e the electron mass, and ε_0 the permittivity of free space. Langmuir waves propagate at relatively low speeds, are reflected by higher density regions, and are subject to significant damping (especially as their wavenumbers increase when entering lower density regions), and so cannot efficiently escape the source region and reach remote observers. Further details on the reflection of electrons from the undisturbed solar wind into the foreshock (and the leakage of heated electrons from downstream of the shock), the development of beam distributions there, and the growth of Langmuir waves are deferred to Section 23.5 below.

The basic model involves coupling of some Langmuir wave energy into radio emission near f_p and $2f_p$, which then propagates to remote observers. The emission processes considered are two of the four known coherent emission processes: so-called "plasma emission" near f_p and $2f_p$ by nonlinear Langmuir wave processes, and so-called "linear mode conversion" (LMC) of Langmuir waves into radio emission near f_p at density gradients. Today the standard processes for the nonlinear plasma emission mechanism are: the electrostatic (ES) decay $L \rightarrow L' + S$ to produce backscattered Langmuir waves L' and ion acoustic waves S from the beam-driven Langmuir waves L; the electromagnetic (EM) decay $L \rightarrow T(f_p) + S'$ to produce radio waves T just above f_p and ion acoustic waves S', stimulated by the ES decay products S; and the coalescence $L + L' \rightarrow T(2f_p)$ of beam-driven L and backscattered L' Langmuir waves to produce radio waves just

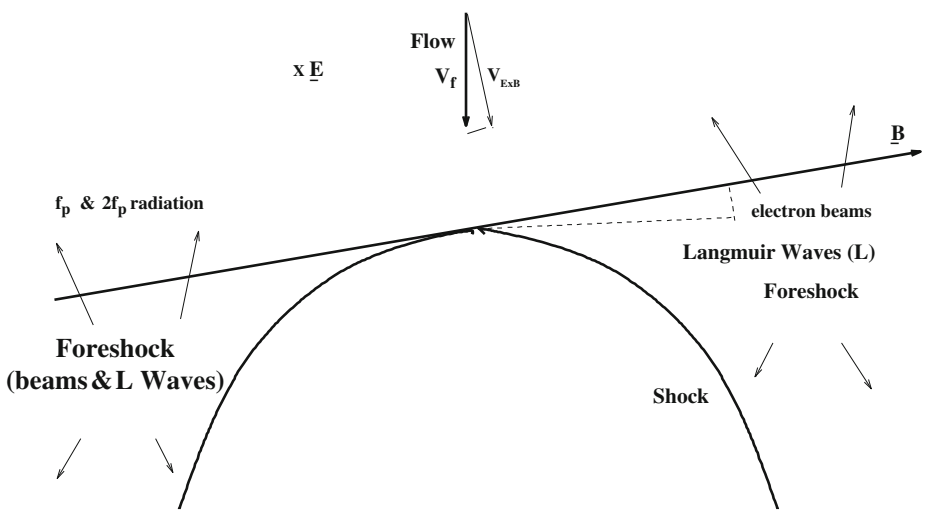

Fig. 23.1 Basic context and model for coherent radio emission associated with shocks, shown in the shock rest frame for a plane defined by the upstream flow velocity **u** and magnetic field vector $\mathbf{B}_u$ that cuts through the 3-D source. Downstream of the magnetic field line tangent to the shock but upstream from the shock, the foreshock regions contain beams of fast electrons (reflected by the shock) which drive high levels of Langmuir waves and radio emissions near f_p and $2f_p$

above $2f_p$ (Cairns and Melrose 1985; Cairns 1988; Robinson and Cairns 1998; Li et al. 2008a, b). These processes conserve frequency (energy) and wavevector (momentum) for the participating waves. In contrast, LMC involves the fact that the L and T modes are not connected in frequency – wavevector ($\omega - \mathbf{k}$) space in a homogeneous plasma, but are connected in $\omega - \mathbf{k}$ space in a density gradient (Budden 1985; Forslund et al. 1975; Yin et al. 1998; Cairns and Willes 2005; Kim et al. 2007, 2008). The connections are restricted to a narrow "radio window" in $\omega - \mathbf{k}$ space as the waves propagate into the density gradient and are subject to damping. For LMC the wave frequency and the component of $\mathbf{k}$ perpendicular to the density gradient are conserved.

Plasma emission is widely favored for f_p and $2f_p$ radiation from Earth's foreshock, type II and III solar bursts, and the 2–3 kHz outer heliospheric emissions (Wild et al. 1963; Kurth et al. 1984; Nelson et al. 1985; Suzuki et al. 1985; Cairns and Melrose 1985; Cairns 1986a, 1988; Gurnett et al. 1993; Robinson and Cairns 1998; Cairns and Robinson 2000; Robinson and Cairns 2000; Knock et al. 2001). Originally discounted because the high observed brightness temperatures were interpreted in terms of nonlinear processes, LMC has enjoyed a renaissance of interest in recent years (Yin et al. 1998; Cairns and Willes 2005; Kim et al. 2007, 2008) and should be considered in detail. Radiation produced at $2f_p$ by the oscillating fields of localized Langmuir wavepackets (Malaspina et al. 2010), proposed in the last year, also needs to be examined fully.

Of course shocks can produce radio emissions by other mechanisms. Incoherent emission of X-ray, UV, optical, and infrared radiation from the regions downstream of shocks, including those associated with stellar winds and bow shocks (which are analogous to the heliosheath region for the 2–3 kHz outer heliospheric emissions) are not considered here. Of interest though is the direct generation of radio emission by "linear" instabilities of the shock-reflected electrons (Wu et al. 1985; Farrell 2001). These mechanisms are very similar to a known fundamental mechanism for coherent radio emissions, the so-called cyclotron maser mechanism (Wu and Lee 1979), but observational evidence for these processes does not yet exist (see Sections 23.3.2 and 23.8 below for more discussion). These mechanisms also appear to require strong tuning of the electron beam parameters to produce radiation near f_p or $2f_p$, rather than over a broadband between these frequencies, and do not appear to be very attractive at this time. In addition, electrons can radiate via the incoherent gyrosynchrotron, synchrotron, or bremsstrahlung mechanisms. An example is the weak gyrosynchrotron emission observed recently from downstream of some CME shocks (Maia et al. 2000; Bastian et al. 2001), while supernova shocks produce radio emission downstream. An aside on this latter context is that the theoretical levels of f_p and $2f_p$ emission produced upstream of supernova shocks should be predicted and compared with observations.

Many of this chapter's topics have been reviewed before, but it appears as though this is the first unified and general review of radio emissions associated with solar system shocks. For instance, previous reviews exist for type II solar radio bursts (Wild et al. 1963; Wild and Smerd 1972; Nelson et al. 1985; Bastian et al. 1998; Reiner 2000; Robinson and Cairns 2000), the 2–3 kHz outer heliospheric radiation (Gurnett and Kurth 1996; Cairns and Zank 2001; Cairns 2004), solar system radio phenomena in general (Wild and Smerd 1972; Gurnett 1995; Cairns and Kaiser 2002), and the radio emission mechanisms (Melrose 1980; Cairns and Robinson 2000). Kellogg (2003) has reviewed Langmuir waves at collisionless shocks. Shock physics and solar system shocks are reviewed elsewhere (Tidman and Krall 1971; Kennel et al. 1985; Russell 1985; Burgess 1995; Lembege et al. 2004; Vrsnak and Cliver 2008).

The foregoing text provides arguments that radio emission associated with shocks involves fundamental plasma physics and is widely important. The chapter proceeds as follows. Section 23.2 summarizes the physics of shocks and identifies unresolved issues that are believed relevant to radio emission. Section 23.3 describes three classes of coherent solar system radio emissions that are definitely observed to be produced by shock waves, including interplanetary type II bursts, focusing on summaries of the observational evidence and the important qualitative theoretical aspects. Section 23.4 describes three classes of observed radio emissions that are believed, but not definitively observed, to be associated with shock waves. Again the focus is on observations and qualitative theoretical aspects. A detailed summary of the standard theory for coherent radio emissions produced by shocks is provided in Section 23.5,

together with unresolved issues. Section 23.6 reviews the observations and theory of type II solar radio bursts, focusing on detailed applications of theory to the observations and on unresolved issues. The detailed theory and unresolved observational and theoretical issues for the 2–3 kHz outer heliospheric emissions are reviewed in Section 23.7. The discussion in Section 23.8 focuses on limitations of the theory and on future applications, including to other planetary foreshocks, mini-magnetospheres for moons and unmagnetized planets, and supernova shocks. Section 23.9 contains the chapter's conclusions.

23.2 Relevant Shock Physics

Macroscopic shocks observed thus far in our solar system, whether "travelling" shocks in the solar wind or "bow shocks" that deflect the solar wind or magnetospheric plasma around a planet or moon, respectively, are nonlinearly steepened waves in the fast magnetosonic or whistler modes (Scudder et al. 1986). Since the fast MHD and whistler modes are connected at high frequencies, they are called "fast mode" shocks.

An ideal fast mode shock has discontinuous changes in the plasma parameters across it. Working in the shock's rest frame, upstream of the shock the plasma flows towards the shock at a speed v_u larger than the fast mode speed v_{ms}, which depends on the Alfven speed V_A, sound speed c_s, and angle θ_{bn} between the upstream magnetic field vector $\mathbf{B}_u$ and the (local) normal direction to the shock surface (Russell 1985; Burgess 1995). Downstream of the shock the plasma's flow speed v_d relative to the shock is smaller than v_{ms}. Defining the fast mode or magnetosonic Mach number of a flow with relative speed v_u by $M_{ms} = v_u/v_{ms}$, upstream of the shock $M_{ms} > 1$ exceeds 1 while $M_{ms} < 1$ downstream. Figure 23.2 illustrates the context.

Conservation of mass, momentum, energy, the tangential component of the electric field, and the normal component of the magnetic field across the local shock surface in a fluid (MHD) model leads to the Rankine-Hugoniot or "jump" conditions for the plasma parameters across the shock (Kennel et al. 1985; Melrose 1985; Burgess 1995). For instance, combining the faster flow speed upstream of the shock than downstream (in the shock rest frame) with mass conservation immediately implies that the downstream

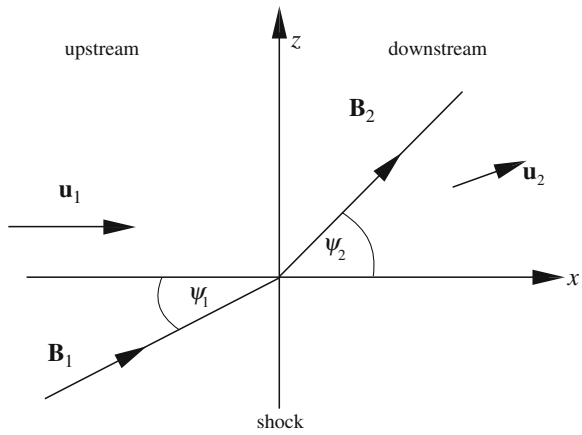

Fig. 23.2 Schematic of the flow velocity and magnetic field vectors upstream and downstream of the shock, in a frame in which the shock is stationary and the upstream flow velocity **u** is oppositely directed to the local shock normal (Burgess 1995). The angle $\psi_1 = 180° - \theta_{bn}$

and upstream densities are related by $n_d/n_u = v_u/v_d$. The increase in density downstream is the counterpart of the flow slowing. It can also be shown that the tangential component and overall strength of the magnetic field and the temperature increase downstream of the shock. The conventional physical picture is that the ram pressure $n_u v_u^2$ of the upstream flow, which is the dominant contribution to the total pressure in the high Alfven and sonic Mach number regime, is primarily balanced by the increased thermal pressure downstream in a time-steady state.

The Rankine-Hugoniot conditions predict that the maximum increase in n_d and B_d (and decrease in v_u) across the shock is a factor of 4 relative to the upstream quantities. In detail these compression ratios (e.g., n_d/n_u or B_d/B_u) increase almost linearly with M_A and M_{ms} for low Mach numbers but asymptote towards 4 once the Mach numbers exceed about 4. However, it is emphasized that the Rankine-Hugoniot analysis does not treat the shock transition region directly but instead assumes that suitable temporal and (macroscopic) spatial averages can be taken such that mass, energy, momentum, the tangential electric field, and the normal magnetic field are conserved across the shock.

The increased strength and more perpendicular orientation of the magnetic field downstream of the shock, compared with upstream, acts like a magnetic mirror. At the simplest level, then, electrons and ions inside the "loss cones" defined by conservation of magnetic

moment and energy will go straight through the magnetic mirror and enter the downstream region. Correspondingly, particles outside their loss cone will be reflected back upstream. The mass difference between electrons and ions leads to different gyroradii and it turns out that the thermal electron gyroradius r_{ge} is typically small compared with the shock transition's thickness L, while thermal protons and other ions typically have gyroradii r_{gi} that are comparable to or larger than L. Accordingly, the electrons are well described by standard orbit theory while the ions see the shock as an abrupt discontinuity. This difference in the behavior of electrons and ions leads to a cross-shock electrostatic potential ϕ_{cs}, which affects the electron loss cone and requires a two-fluid (rather than MHD) approach for development of an accurate shock theory. The electron fluid momentum equation can be rearranged to yield

$$\mathbf{E}_{cs} = -\nabla\phi_{cs} = -\frac{1}{en_e}\nabla P_e - \mathbf{v}_e \times \mathbf{B}\,. \qquad (23.3)$$

ignoring the inertia term, where P_e is the electron pressure tensor. In the shock's de Hoffman-Teller frame, in which the electron velocity $\mathbf{v}_e$ is parallel to $\mathbf{B}$ and there is no convection electric field, the $\mathbf{v}_e \times \mathbf{B}$ term vanishes and the cross-shock potential depends only on the electron pressure and density profiles. Under various circumstances (primarily involving the magnetic, density, and perpendicular electron temperature profiles being stepwise continuous and proportional) Eq. (23.3) simplifies to (Hull et al. 1998; Kuncic et al. 2002)

$$\phi_{cs} = 2k_B\Delta T_e = 2k_B T_{e\perp 1}\frac{\Delta B}{B_u}\,, \qquad (23.4)$$

where Δ identifies the change across the shock (from upstream to downstream), k_B is Boltzmann's constant, T_e is the total electron temperature, and $T_{e\perp u}$ is the upstream perpendicular (to $\mathbf{B}$) electron temperature.

The cross-shock potential has fundamental consequences for shocks with high enough M_{ms}. Since the shock heats the electrons (Scudder et al. 1986), ϕ_{cs} must be positive. Accordingly, the cross-shock potential attracts electrons downstream but resists the motion of ions across the shock: indeed, it reflects ions with incident energies less than ϕ_{cs} (Leroy et al. 1982). These reflected ions are then specularly reflected, with their initial reflected normal velocity the opposite of their incoming normal velocity. This reflection represents a significant energization, since the ions start off at a speed $\approx 2u$ relative to the upstream ions, and leads to the ions having a ring in perpendicular velocity space. The ion gyromotion allows the ions to gyrate upstream approximately half a gyroperiod before coming back towards the shock with sufficient energy to surmount the potential and move downstream. The ring is unstable to the growth of waves both upstream and downstream, leading to additional thermalization.

Crucially, the reflected ions have a considerable current, leading to an increase in magnetic field in the "foot" region upstream, an overshoot just downstream of the main ramp, and then a periodic undershoot-overshoot pattern in the magnetic field profile. Figure 23.3 illustrates the characteristic magnetic and potential profiles across a "supercritical" shock for which ion reflection is important.

Electrons moving through the spatially varying magnetic and electric fields of the shock can

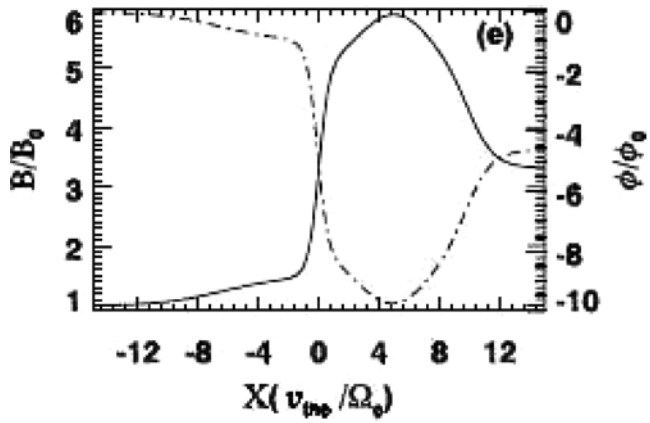

Fig. 23.3 Model spatial profiles for the normalized magnetic field (*solid line*) and cross-shock potential (*dash-dot line*) (Yuan et al. 2008a). The upstream is to the left, with the foot located where $-12 < X < 0$, the ramp centered at $X = 0$, and the overshoot peaking at $X = -5$

be reflected or transmitted, because the increasing magnetic field from upstream to downstream acts as a magnetic mirror that is partially counteracted by the cross-shock potential pulling electrons downstream. Accordingly, as detailed in Section 23.5 below, these profiles are vital in this paper because they determine (1) which (upstream) electrons are reflected back upstream into the foreshock and (2) which (downstream) electrons are able to leak upstream into the foreshock. The cross-shock potential also has a role in heating the downstream electrons and driving waves inside the shock structure, since it creates a void at low energy in the electron distribution function $f(v_{\parallel},v_{\perp})$ of upstream electrons moving downstream and reflects downstream electrons that attempt to move upstream but have insufficient energy (Scudder et al. 1986; Hull et al. 1998). Waves should then grow to fill in the void and remove unstable features in $f(v_{\parallel},v_{\perp})$, thereby resulting in at least parallel electron heating. Strong levels of electrostatic waves, presumably driven by these electron-ion and electron-electron drifts, are indeed observed in the ramp and downstream region of the shock (Rodriguez and Gurnett 1975; Onsager et al. 1989). It is recognized that the void feature caused by the cross-shock potential can, when partially relaxed, resemble an electron beam (Scudder et al. 1986): these beams have been observed by Feldman et al. (1983) and Fitzenreiter et al. (2003) in the near vicinity of the shock ramp. However, this beam is rapidly removed by wave growth and associated quasilinear relaxation to produce the "flat top" electron distributions found throughout the macroscopic regions downstream of shocks (Feldman et al. 1983; Scudder et al. 1986; Fitzenreiter et al. 2003). Only quasithermal levels of Langmuir waves are found within the ramps and downstream regions of shocks (Rodriguez and Gurnett 1975; Onsager et al. 1989).

With observable electron beams not produced in the macroscopic regions downstream of shocks (but only in the very near vicinity of the shock ramp), the foreshock region is the natural place to look for electron beams and associated Langmuir waves. These are indeed widely observed throughout the macroscopic foreshock regions. The natural mechanism to develop and recreate beam features in $f(v_{\parallel},v_{\perp})$ for (upstream) electrons reflected back upstream into the foreshock is detailed in Section 23.4, as is the beam instability which often drives intense Langmuir waves there.

Above it is assumed that the shock structure remains constant in time. Here we focus on the facts that (1) the magnetic overshoot in Fig. 23.2 can significantly exceed the maximum (of 4 relative to B_u) predicted by the Rankine-Hugoniot conditions and (2) the temporal and spatial averages required for the Rankine-Hugoniot analysis do not require a time-steady shock structure. Indeed, for a long time it has been predicted based on simulations that shocks become unsteady at high enough M_A and M_{ms}, undergoing continuous self-reformation processes rather than being constant in time (Leroy et al. 1982; Lembege et al. 1987; Krasnoselskikh et al. 2002; Hellinger et al. 2002, 2007; Yuan et al. 2009; Lembege et al. 2009). The reformation appears to be correlated with the specularly reflected ions as they gyrate first upstream and then downstream (Leroy et al. 1982; Hellinger et al. 2007; Yuan et al. 2009; Lembege et al. 2009), with reformation corresponding to a group of gyrating ions driving waves which steepen into a new shock front upstream of the old one, which then decays. Both the magnetic overshoot and reformation thus appear to be associated with the gyrating ions. Thus far observational evidence of reformation remains elusive and indirect (Lobzin et al. 2007).

An important aspect of reformation is that the magnetic compression ratios need not be limited by the Rankine-Hugoniot conditions but can instead be larger at some stages of the reformation cycle: this would lead to cyclic variations in the properties and number of electrons being reflected back (and leaked) into the foreshock. Such cyclic variations of the reflected electrons have been demonstrated for reforming shocks and shown to be material (e.g., factors of 2–4 in the reflected fraction, depending on the shock parameters) and likely important to type II bursts (Yuan et al. 2007, 2008b).

The foregoing review of shock physics has only touched on some aspects of active research. Other current research addresses the physics of reformation for fast mode shocks and the nature of the dissipation and wave growth processes at them (Lembege et al. 2004; Scholer and Matsukiyo 2004; Matsukiyo and Scholer 2006; Hellinger et al. 2007; Yuan et al. 2009; Lembege et al. 2009), but is not reviewed here.

23.3 Definite Shock-Driven Radio Emissions

This section presents observational data and associated theoretical interpretations for three classes of solar system radio emissions that have been definitively associated with shocks: interplanetary type II bursts, radiation from Earth's foreshock, and radiation from some shocks bounding corotating interaction regions (CIRs).

23.3.1 Interplanetary Type II Bursts

Interplanetary type II bursts were discovered by Cane et al. (1982) and immediately interpreted in terms of f_p and $2f_p$ radiation associated with a shock. Figure 23.4 provides an example of an interplanetary type II and illustrates several important aspects. First, interplanetary type IIs are often very intermittent and fragmented, rather than continuous. Second, these bursts often have a fundamental (or F) band (f_p radiation) and a harmonic (H) band ($2f_p$ radiation) during the event as a whole, but often only one band or indeed no emission is observable at a given time. Figure 23.4 shows a clear H band only around 1800 on 25–26 August, with evidence for both F and H emission only prior to about 0600 on 25 August.

The third, and perhaps most important, aspect is that the type II emission is well organized by the lines labelled F and H in this $1/f - t$ dynamic spectrum (Reiner et al. 1998; Reiner 2000; Lobzin et al. 2008). These lines are defined by assuming that: (i) the solar wind density obeys $n_e(r) \propto r^{-2}$, as expected for a constant speed, time-steady, spherically symmetric wind; (ii) the shock speed v_{sh} is constant, and (iii) the emission is at $f_p(r(t))$ and $2f_p(r(t))$ upstream of the shock. Then the shock location is $r(t) = r_0 + v_{sh}(t - t_0)$, where r_0 and t_0 are the heliocentric distance and time when the emission starts, and it is easy to show using Eq. (23.1) that (Reiner et al. 1998; Reiner 2000)

$$\frac{1}{f(t)} = \frac{1}{mf_p(r(t))} = Av_{sh}(t - t_0)\,. \tag{23.5}$$

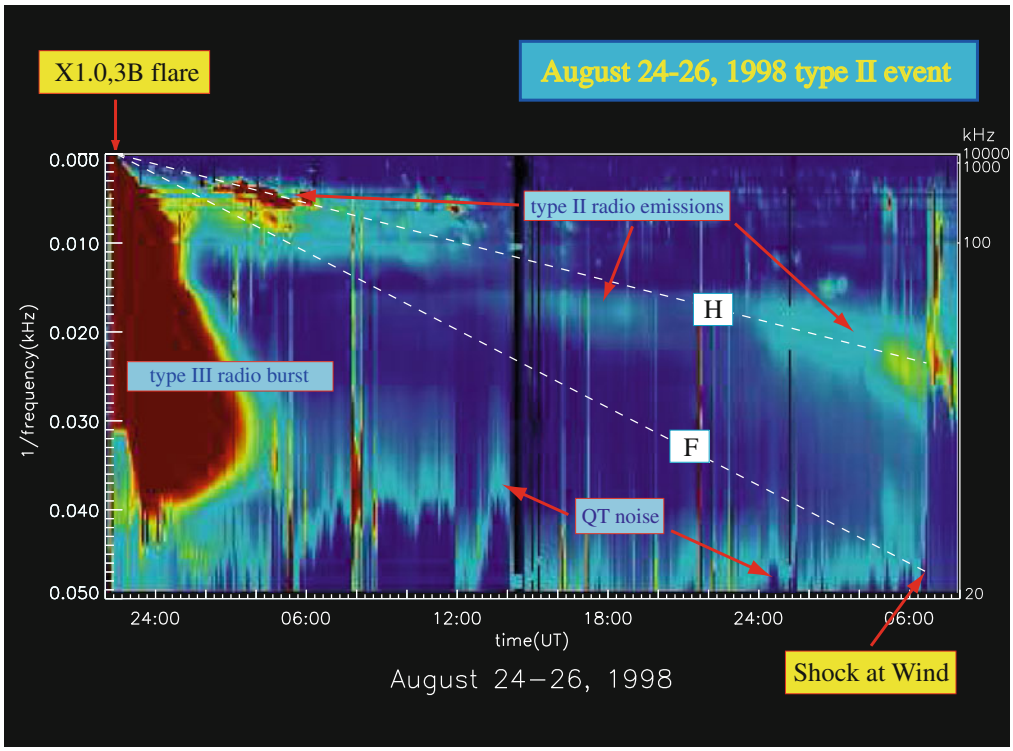

Fig. 23.4 Dynamic spectrum in $1/f - t$ space of an interplanetary type II burst, as well as an interplanetary type III burst and quasithermal plasma noise at f_p (Reiner 2000). The type II radiation is well organized by the two lines F and H discussed in the text. The type II shock arrived near 06:40 on 26 August

Here $m = 1$ or 2 for F or H radiation, respectively, and the constant A is determined by the density at 1 AU when the shock arrives at Earth: the only free parameter then is v_{sh}. Thus, the organization of the type II radiation along two straight lines in Fig. 23.4's $1/f - t$ dynamic spectrum provides a very strong argument that the radiation is indeed produced at f_p and/or $2f_p$ upstream of the shock wave. Moreover, the slope of the line provides a way to estimate v_{sh}.

Definitive evidence that interplanetary type II bursts are produced upstream of a shock, in foreshock regions filled with electrons reflected and accelerated at the shock and with Langmuir waves driven by the electrons, is provided by Fig. 23.5 (Bale et al. 1999). The bottom two panels show clearly the shock's magnetic and density signatures, with the downstream region entered about 0640:30 UT. The top panel is a $f - t$ dynamic spectrum of the electric field fluctuations detected by the Wind spacecraft's WAVES instrument: it shows strong levels of radio waves just above the local f_p and near $2f_p$ (prior to 0638:30 UT), intense Langmuir waves near f_p from about 0638:30 UT until

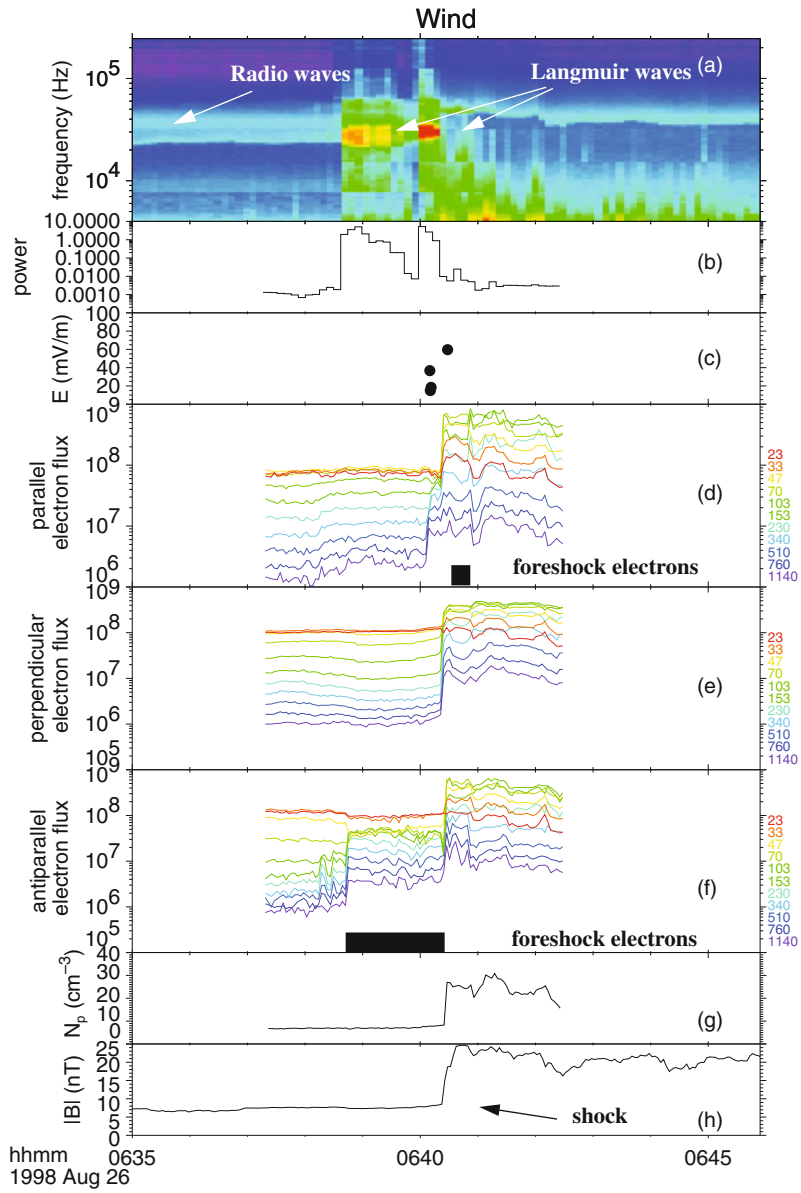

Fig. 23.5 Detailed radio and in situ observations of the source region of an interplanetary type II burst on 26 August 1998 (Bale et al. 1999). Described more in the text, the panels from top to bottom contain **a** an electric field spectrogram, **b** the power in Langmuir waves, **c** the times of TDS capture events, **d** –**f** the fluxes in different energy bands (colors) of electrons moving parallel, perpendicular, and anti-parallel, respectively, to **B**, and **g** and **h** n_e and B, respectively, as functions of time

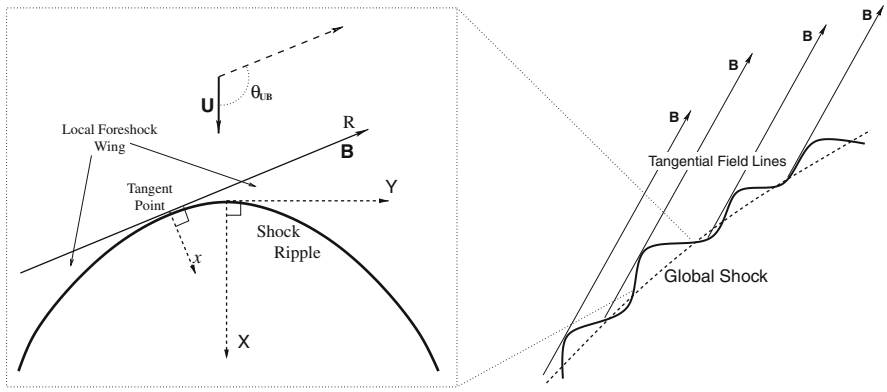

Fig. 23.6 Schematic (Knock et al. 2003b) that (*left*) defines the parameters of a ripple and (*right*) shows how multiple ripples on the macroscopic shock can explain qualitatively the electron and Langmuir observations in Fig. 23.5

0640:30 UT upstream of the shock, and then quasithermal plasma noise at the downstream f_p after the shock. The next two panels show the Langmuir wave power and the times of particularly intense Langmuir waves captured by the Time Domain Sampler subinstrument, respectively. The fourth to sixth panels show the fluxes of electrons with different energies (colored lines) moving parallel, perpendicular, and antiparallel to **B**, respectively. Large increases in the flux of electrons moving parallel and anti-parallel to **B** are observed in the foreshock, consistent with reflection back upstream of accelerated electrons, while the simultaneous increase in perpendicular electron fluxes at all energies marks the shock transition (and the observation of the denser, shock-heated downstream electrons). During the upstream period **B** remained essentially constant in direction.

In Fig. 23.5 it is crucial to note the absence of three vital signatures in the downstream region. First, there are no strong (or even significantly nonthermal) Langmuir waves downstream of the shock (e.g., after 0640:30 UT). Second, no radio emissions at twice the downstream f_p (at about four times the upstream f_p) are observed. Third, changes in the downstream electron fluxes tend to occur simultaneously in all three panels, thereby providing no evidence for any processes that might produce beams of electrons in the downstream region rather than just the shock-heated downstream electrons. Thus, for this event at least, there is no evidence for any processes that might produce f_p or $2f_p$ radiation downstream of the shock.

It should be questioned how the shock can produce (Fig. 23.5) enhanced levels of upstream electrons moving anti-parallel to **B** for several minutes at the spacecraft and then simultaneously have electrons reach the spacecraft moving parallel to **B**, with **B** essentially constant in direction for the whole period. A planar shock cannot produce this signature, so Bale et al. (1999) interpreted the signature in terms of the shock having a ripple or indentation (Fig. 23.6), so that as the shock moved outward the spacecraft observed electrons first from one side of the ripple and then from both sides just before the shock crossing.

This ripple is evidently at intermediate scales between the scale of the macroscopic shock (of order 0.2 – 1 AU) and those for the microphysics of the shock and the electron – Langmuir wave – radiation interactions. Bale et al. (1999) estimated that the ripple had a characteristic height (or distance along the radial direction) in the directions parallel and antiparallel to **B** of $\approx 1.4 \times 10^8$ m and $\approx 2.5 \times 10^7$ m, respectively. More accurate analyses of the Bale et al. shock and two others yield (Fitzenreiter et al. 2003; Pulupa and Bale 2008) heights and distances along $\pm$**B** in the ranges $(1-7) \times 10^7$ m and $(8-14) \times 10^7$ m, respectively. A recent theoretical model for type IIs (Knock et al. 2003b; Knock and Cairns 2005; Cairns and Knock 2006) assumes that the entire shock has ripples with characteristic scales of order the decorrelation length l_b of the magnetic field in the solar wind, $\approx 10^9$ m or 0.01 AU at the orbit of Earth. Intuitively the shock should have ripples on this scale since the shock surface will depend sensitively on the spatially-varying fast mode speed, which will certainly vary on scales of order l_b. Observations show such ripples (Neugebauer and Giacalone 2005).

Other inhomogeneities and structures exist in the solar wind, including shocks associated with previous CMEs or outbursts and those associated with corotating interaction regions. Interactions between a

fast CME-driven shock driving a type II burst and other shocks that are travelling more slowly, or more likely the regions with increased numbers of accelerated and heated electrons associated with these earlier shocks, might then be expected to lead to more intense type II emission and fine structures. Gopalswamy et al. (2001, 2002) have interpreted the fine structures observed in interplanetary type IIs with interactions of a faster CME-driven shock with a previous, slower, CME-driven shock ("CME cannibalism"), while Reiner et al. (1997, 2001) and Hoang et al. (2007) have interpreted observed fine structures in terms of a CME-driven shock interacting with CIR shocks. Theoretical calculations also demonstrate that fine structure should be produced by the shock moving through such interaction regions and the spatially inhomogeneous corona and solar wind (Knock and Cairns 2005; Cairns and Knock 2006), as shown in Section 23.6 below. Returning to the observations, the type II – CIR associations of Reiner et al. (1997, 2001) and Hoang et al. (2007) are based on "direction finding": as a spacecraft rotates, an antenna in the spin plane detects a time-varying, periodic, signal, which maximises when the antenna is perpendicular to the source direction (in the spin plane) for a radio signal. Direction finding with two widely separated spacecraft allows the (assumed common) radio source to be triangulated and then associated with the predicted location of the CIR.

More generally theory predicts that the properties of the accelerated electrons, Langmuir waves, and radio emissions should depend on the shock speed and 3-D locus, the spatially varying **B** field, and the properties of the spatially varying upstream plasma, e.g., n_e, **u**, T_e, and T_i (Holman and Pesses 1983; Cairns 1986a; Knock et al. 2003a, b). Thus, solar wind inhomogeneities should induce fine structures into the type II burst (Knock et al. 2003b; Knock and Cairns 2005). The degrees to which inhomogeneities and other structures in the solar wind, as opposed to ripples and 3-D inhomogeneities in the macroscopic shock, induce the observed fine structures and variabilities in type II bursts will be addressed partially in Section 23.6 below and in future work.

Until quite recently the interplanetary type II in Fig. 23.5 and Bale et al. (1999) was the only one whose source region had been definitively observed by spacecraft and analysed in detail. Recently, however, Fitzenreiter et al. (2003) and Pulupa and Pulupa and Bale (2008) presented observations of upstream Langmuir waves and reflected electrons for five additional events, at least two with local type II emission. Fitzenreiter et al. (2003) found beams in the upstream reduced electron distribution for 4 events. Pulupa and Bale (2008) showed for three events (2 plus the August 1998 type II) that the reflected electrons have weak loss cone features and bumps in the reduced electron distribution function (integrated over perpendicular velocity space), and obey inverse velocity dispersion (i.e., faster electrons arrive before slower electrons). Furthermore, in all three cases the electron observations were consistent with the shock surface being rippled, with electrons being detected both parallel and anti-parallel to **B** in the original Bale et al. event and one other. While the three observed events may be anomalous, this would be most unlucky and the observed properties are consistent with those for Earth's foreshock, described next. Accordingly the simplest interpretation is adopted here: that the type II source observations to date are typical. Moreover, to the best of this reviewer's knowledge, significantly nonthermal Langmuir waves are never observed downstream of shocks (except perhaps sometimes in the shock ramp itself as the beam induced by the cross-shock potential is relaxed into a flat-top distribution – see Section 23.2 for more detail), but instead only upstream.

23.3.2 f_p and $2f_p$ Radiation from Earth's Foreshock

Radio signals at twice the solar wind plasma frequency near Earth were first observed in 1974 and have been studied extensively since (Dunckel 1974; Gurnett 1975; Hoang et al. 1981; Cairns and Melrose 1985; Cairns 1986b; Burgess et al. 1987; Reiner et al. 1997; Kasaba et al. 2000). The radiation was interpreted almost immediately by analogy with type II and III bursts in terms of electrons accelerated at the bow shock and then associated Langmuir waves and radio emissions at $2f_p$. Cairns (1986b) first claimed the existence of f_p radiation and showed definitively that the $2f_p$ signals are transverse electromagnetic radiation in the free-space modes, using (1) the simultaneous observation of harmonic

radiation from regions with different densities present simultaneously in the foreshock, (2) the persistence of these signals into the undisturbed solar wind and other regions of the foreshock, (3) the inability of electrostatic modes to propagate significant distances, and (4) the free-space mode being the only essentially undamped mode significantly above f_p in a stable plasma like the solar wind (Fig. 23.7). He also showed that occasionally radiation at $3f_p$, $4f_p$, and $5f_p$ is observable, as subsequently claimed for a type II solar radio burst (Kliem et al. 1992). Burgess et al. (1987) showed definitively that f_p radiation is also produced in Earth's foreshock (Fig. 23.8), using the same arguments as (1)–(5) above but for f_p radiation. At times, then, f_p and $2f_p$ radiation from different parts of the foreshock are observable.

Another argument for the radiation source being the (3-D) foreshock is based on "direction finding", as explained above for interplanetary type IIs. Early workers (Hoang et al. 1981; Cairns 1986b) used a single spacecraft to establish consistency with the foreshock, while Reiner et al. (1997) used direction-finding with two spacecraft to triangulate the radio source and found it to be in the foreshock.

A final argument for $2f_p$ radiation being generated in the foreshock comes from the observed spatial variations in intensity. Specifically, Lacombe et al. (1988) and Kasaba et al. (2000) found that the $2f_p$ radiation has its largest fields relatively close to the upstream boundary of the foreshock, in approximate coincidence with the largest fields of Langmuir waves, and not in the solar wind or the deep foreshock. This is expected if the radio source lies in the foreshock and is associated with the Langmuir waves or their driving electron beams.

The foreshock regions of Earth's bow shock are observed routinely and found to contain high levels of Langmuir waves and energetic electrons streaming away from the bow shock (Filbert and Kellogg 1979; Anderson et al. 1981; Bale et al. 1997; Cairns et al. 1997; Bale et al. 2000). When the solar wind properties and shock location are almost con-

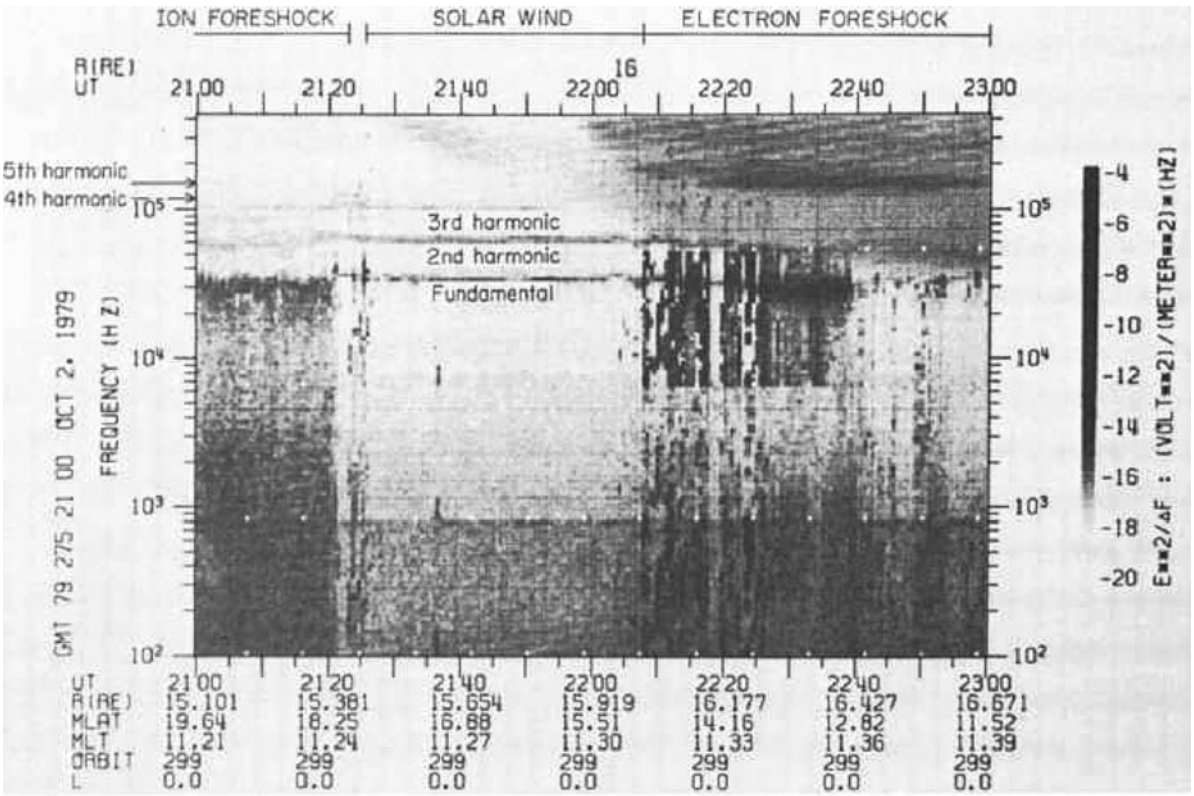

Fig. 23.7 Electric field spectrogram of ISEE-1 spacecraft data clearly showing f_p, $2f_p$, and $3f_p$ radiation in the solar wind (2 October 1979) and the foreshock (Cairns 1986b). Fine structures in the $2f_p$ radiation are associated with regions of different density being simultaneously present in the foreshock

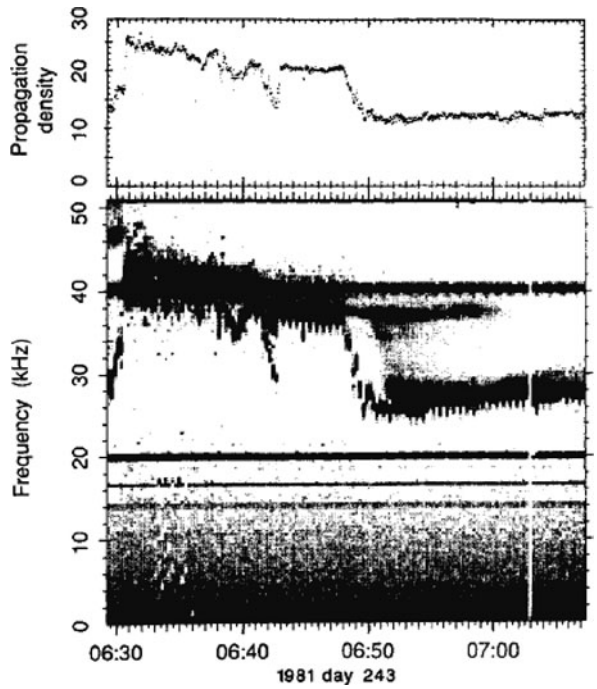

Fig. 23.8 Electric field spectrogram of ISEE-1 spacecraft data showing fine structures in f_p and $2f_p$ radiation associated with regions of different density being simultaneously present in the foreshock (Burgess et al. 1987). This establishes the electromagnetic free-space mode character of the f_p signals

stant in time a spacecraft entering the foreshock from the solar wind first observes small numbers of very energetic electrons and then larger numbers of slower electrons. This "inverse" velocity dispersion, meaning fast electrons closest to the upstream foreshock boundary and slow ones well downstream from the boundary, is characteristic. It leads naturally to beam distributions of electrons (Fig. 23.9), as observed in foreshock regions where the relative beam number density is highest and the beam speed varies slowly with position (Fitzenreiter et al. 1984; Fitzenreiter et al. 1990). The velocity dispersion and development of electron beams is explained physically in terms of "cutoff" and "time-of-flight" effects in Section 23.5 below, based on the research of Filbert and Kellogg (1979) and Cairns (1987a). The electron beams show clear evidence of loss cone effects, consistent with conservation of the magnetic moment in the reflection process at the shock, which is sometimes called fast Fermi acceleration (Wu 1984).

The properties of the Langmuir waves also vary with position relative to the foreshock boundary: the waves are quasithermal in the solar wind but their average fields first increase with increasing penetration into the foreshock, rising to a peak downstream of but relatively close to the foreshock boundary, before decreasing with increasing distance downstream from the boundary. The waves are intrinsically bursty, with fields that vary rapidly in time at a given location and also vary rapidly with position. Some wavepackets have very strong fields of order 40 mV/m although fields of order $0.01 - 10$ mV/m appear more typical (Anderson et al. 1981; Bale et al. 1997; Cairns et al. 1997; Bale et al. 2000; Kasaba et al. 2000; Henri et al. 2009; Malaspina et al. 2009, 2010). Very recent observations from the STEREO spacecraft suggest that some Langmuir wavepackets are actually eigenstates of density depressions (Ergun et al. 2008; Malaspina et al. 2009, 2010), while others are beam-driven wavepackets. The threshold field for the ES decay $L \rightarrow L' + S$ depends on the beam speed v_b and its spread, as well as on other properties, thereby varying with location throughout the foreshock. Values between 0.1 and 20 mV m^{-1} have been calculated for various locations in the foreshock (Robinson and Cairns 1995; Cairns et al. 1997), thereby suggesting that many observed wavepackets are above the ES decay threshold and that the ES decay should proceed. Very recent observations and associated simulations for type III bursts, complementing earlier observations and theory (Cairns and Robinson 1995), provide an independent argument by analogy that ES decay pro-

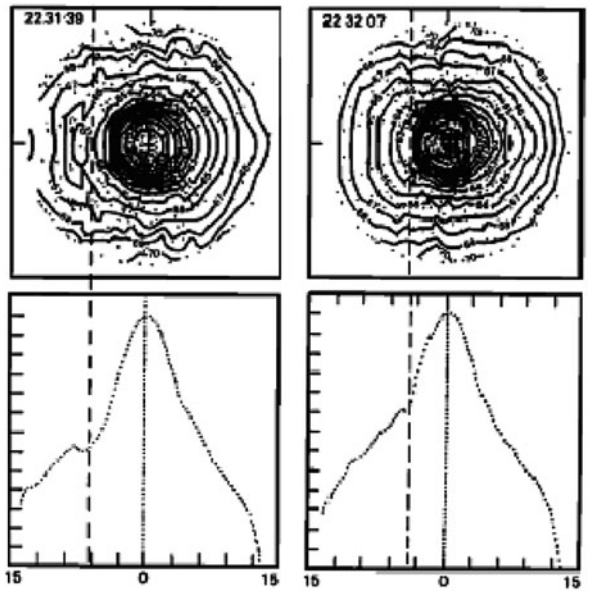

Fig. 23.9 Examples of electron beams observed in Earth's foreshock by the ISEE-1 spacecraft (Fitzenreiter et al. 1990): the *top panels* show the gyrotropic 2D distributions $f(v_\parallel, v_\perp)$ and the *bottom panels* the reduced distributions $f_r(v_\parallel)$. *Dot symbols* show the locations of the phase space regions sampled and contours are spaced by 1 in units of $\ln f$. Note the clear evidence for loss cone features in $f(v_\parallel, v_\perp)$ and for beams in $f_r(v_\parallel)$ for these well-chosen examples

ceeds in Earth's foreshock for wavepackets with large enough fields (Henri et al. 2009).

The waves have field statistics consistent with quasithermal plasma noise in the solar wind and thermal waves subject to an instability just inside the foreshock boundary (Cairns et al. 2000), before then developing lognormal statistics consistent with stochastic growth theory (SGT) deeper in the foreshock (Cairns and Robinson 1997, 1999; Sigsbee et al. 2004; Krasnoselskikh et al. 2007). When ES decay is important, the probability distribution of wave (envelope) fields should be reduced below the lognormal prediction at fields above the threshold. While this has been observed for Langmuir waves in the source regions of type III bursts it has not been observed in the foreshock statistics. Nevertheless, since an SGT state is very close to marginal stability, the observed field statistics (Fig. 23.10) provide strong justification for assuming that the electron distribution is close to marginal stability, that SGT applies for fields below the ES decay threshold, and that the ES decay proceeds as needed for the radio emission processes.

Plotted in Fig. 23.10 (left) are the electric fields of bursty Langmuir waves in Earth's foreshock as a function of the distance D_f of the spacecraft downstream from the tangent magnetic field line measured along the solar wind velocity, otherwise known as the DIFF parameter of Filbert and Kellogg (1979). The intrinsic burstiness of the waves is clear. On the right is the probability distribution $P(X)$ of the scaled wave electric field variable $X = (\log E - \mu(D_f))/\sigma(D_f)$, where each wave field sample E is compared with the mean value $\mu(D_f)$ and standard deviation $\sigma(D_f)$ of the logarithm of the field at the location D_f for the sample. SGT predicts that E should be lognormally distributed, so $\log E$ should be Gaussian distributed and X should be Gaussian distributed with zero mean and unit standard deviation. Both the wave fields and distribution $P(X)$ are for a period when the solar wind was unusually stable and the spacecraft's time-varying location in the foreshock could be calculated with great certainty (Cairns et al. 1997). Power-law mod-

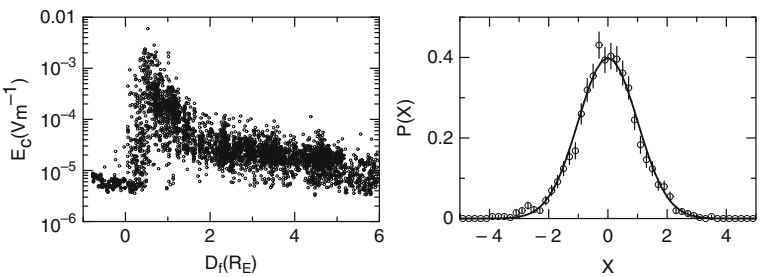

Fig. 23.10 (*Left*) Bursty Langmuir wave fields measured as a function of the distance D_f in Earth's foreshock (Cairns and Robinson 1999). (*Right*) Corresponding field statistics for Langmuir waves in Earth's foreshock (Cairns and Robinson 1999), presented in terms of the probability distribution $P(X)$ described in the text. The *solid line* shows the SGT prediction. Excellent agreement is apparent

els for $\mu(D_f)$ and $\sigma(D_f)$ were obtained, consistent with the raw field data, by minimizing χ^2 between the predicted and observed distributions $P(X)$ and so placing strong constraints simultaneously across most of the foreshock. Excellent agreement with the SGT prediction is apparent in Fig. 23.10 (right). Subsequent work shows similar results (Sigsbee et al. 2004; Krasnoselskikh et al. 2007). The small differences (Krasnoselskikh et al. 2007) are attributable to inadequate consideration of spatial variations in $\mu(D_f)$ and $\sigma(D_f)$ and to sampling on fast timescales commensurate with or smaller than the timescales of the stochastic fluctuations in the growth rate considered explicitly by SGT (Robinson et al. 1993; Cairns and Robinson 1997). SGT appears to apply widely in space and astrophysical wave phenomena (Robinson et al. 2006).

Other mechanisms than plasma emission have been proposed for foreshock f_p and $2f_p$ radiation. For instance, Wu, Gaffey, Farrell, and others (Wu et al. 1985; Farrell 2001) proposed cyclotron maser emission from a relativistic ring-beam distribution of electrons leaving the shock. This mechanism is predicted to produce radiation with fine structures spaced by close to the electron cyclotron frequency f_{ce}. The mechanism also requires careful tuning of the beam parameters (including rather large perpendicular speeds for the ring) for the radiation to be close to $2f_p$ rather than near $1.5f_p$ or other frequencies. This tuning and the typical absence of radiation except very close to f_p and $2f_p$ are strong arguments against such cyclotron maser mechanisms being relevant for foreshock radiation, as is the absence of a detailed theoretical mechanism for the ring-beam. The reason for making this last point is that while mirror reflection indeed yields a loss-cone, it appears that the conditions for significant emission requires the ring-beam to be centered near pitch-angles of about 45° (Farrell 2001) whereas mirror reflection for typical shocks yields loss-cone angles less than 20° (Yuan et al. 2008a).

When the electron cyclotron frequency f_{ce} is unusually large ($\geq$ 400 Hz) fine structures regularly spaced by $f_{ce}/2$ are sometimes observed in f_p radiation and the corresponding electrostatic waves (Cairns 1994). Intuitively these phenomena might lead to $2f_p$ radiation with fine structures spaced by f_{ce}, but this has not yet been observed for the foreshock's $2f_p$ radiation: if so, then this splitting may be relevant to split-band fine structures in coronal type II bursts (Cairns 1994), as discussed in Section 23.4.1.1 below. It is noted that the loss cone features expected on the reflected electron distribution (Fitzenreiter et al. 1990), due to conservation of the magnetic moment in the reflection process, can lead theoretically to fine structure near f_{ce} in electrostatic waves below f_p when the electron beam speed is very slow (Lobzin et al. 2005). These theoretical calculations have not been extended yet to the faster electron beams with $v_b/V_e \geq 3-20$ of primary interest here. This should be done, focusing on frequency fine structures in the Langmuir waves caused by loss cone features that might survive into radio emissions near f_p and $2f_p$ produced by nonlinear processes, as well as linear instabilities for the radio waves. Similarly, more observations are encouraged of fine structures in f_p and $2f_p$ radiation and associated electrostatic waves near f_p for Earth's foreshock and other radio emissions associated with shocks. The reason is that these observations may place strong constraints on the mechanisms responsible for the radiation. It is probably worthwhile stating here, though, that multiple mechanisms may exist for f_p and $2f_p$ radiation, with some occurring under some conditions but not others. Accordingly, different radio emissions may have different detailed mechanisms, while a single source might have different mechanisms active simultaneously, e.g., in distinct spatial regions of the source.

Finally, very recently Malaspina et al. (2010) calculated the $2f_p$ emission resulting from the nonlinear currents of Langmuir eigenstates, finding that it may be significant and even dominate the nonlinear Langmuir processes considered above. This novel mechanism needs to be evaluated in detail.

In summary, strong evidence exists that Earth's f_p and $2f_p$ radiation are associated with high levels of Langmuir waves driven by electron beams (perhaps with loss cone features) produced at Earth's bow shock. Direct generation of the radiation appears implausible at this time, leaving nonlinear Langmuir processes and linear mode conversion as the favored mechanisms.

23.3.3 Radio Emission from Corotating Interaction Regions

Hoang et al. (1992) presented Ulysses observations of Langmuir waves and radio emissions associated with

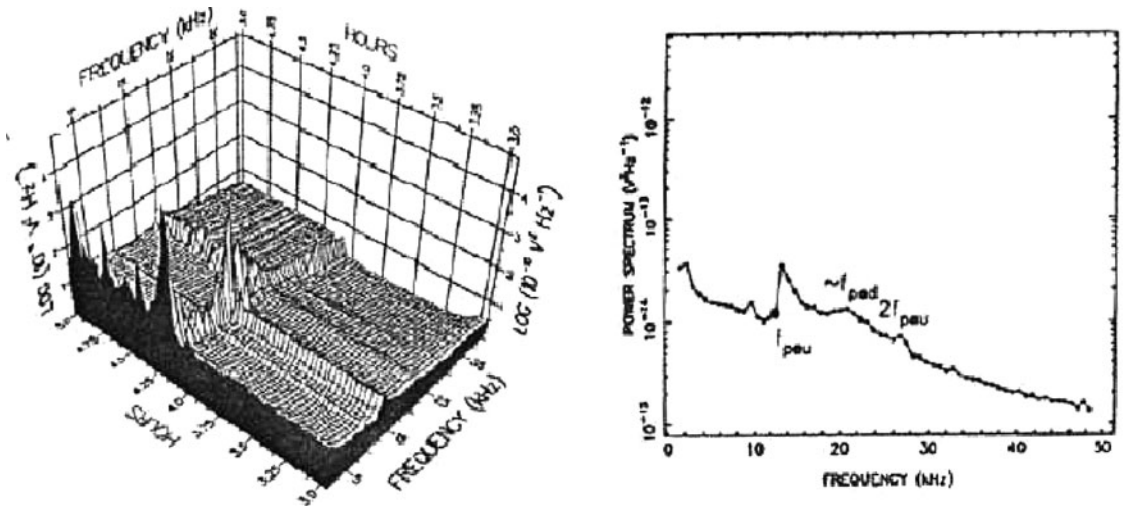

Fig. 23.11 Ulysses electric-field observations before and after the forward CIR shock of 27 May 1991 reported by Hoang et al. (1992): **a** Time-series of electric field spectra; **b** Spectrum near 03:56 UT in the upstream region. Here f_{ped} and f_{peu} refer to the values of f_p downstream and upstream, respectively, of the shock.

corotating interaction regions (CIRs) beyond 1 AU. They found Langmuir waves upstream of three of four forward CIR shocks, including the two with the largest simultaneous values of M_A $(2.9 - 3.6)$ and θ_{bn} $(\geq 65°)$, and noted that the period observable with Langmuir waves increased with θ_{bn}. Figure 23.11 shows the wave and radio data for the strongest shock, on 27 May 1991. Hoang et al. did not report nonthermal Langmuir waves downstream of the forward shocks or in the vicinity of their three reverse shocks, neither upstream nor downstream.

For the two strongest shocks described above Hoang et al. (1992) observed radiation at twice the local upstream value of f_p, when upstream of the shock; e.g., the signal near 27 ± 2 kHz in Fig. 23.11. The signal near $f_p \approx 14 \pm 1$ kHz is the combination of quasithermal plasma noise, nonthermal Langmuir waves, and perhaps foreshock f_p radiation, dominated by the first. This represents the first detection of $2f_p$ radiation generated upstream of a CIR shock.

Controversially, Hoang et al. (1992) suggested that the broad signal near 20 kHz might be fundamental radiation from downstream of the shock. This "downstream" source model is the opposite of the standard "upstream foreshock" model and would require a comprehensive reevaluation of the standard theory. However, strong arguments against this interpretation are advanced here based on the same observations reported by Hoang et al. (1992). First, the authors state that the signal was observed for more than 1 day before the shock crossing, as opposed to less than 30 min for the upstream $2f_p$ radiation, and had a much smaller frequency drift than typical type II bursts. Second, significantly nonthermal Langmuir waves were observed upstream but not downstream of the shock and, third, the shock does not appear to be unusual. Accordingly, much simpler interpretations of the data are that the long-lived signal near 20 kHz is either (i) coming from remote upstream source regions where f_p or $2f_p$ is close to 20 kHz or (ii) not related to the CIR but is instead coming from a distant and unrelated source. It is not known whether so-called planetary continuum radiation from Jupiter, Saturn, and Earth, have been ruled out as a possible source of the 20 kHz signal.

Thus, Hoang et al. (1992) observations and analyses establish that CIR shocks can stimulate $2f_p$ radiation from upstream foreshocks with Langmuir waves, thereby generalizing the phenomenon beyond CME shocks and bow shocks. However, their work does not establish the generation of radio signals near f_p and $2f_p$ in the region downstream of CIR shocks. Instead, the one event reported in which a radio signal was observed upstream of a CIR shock at a frequency near the downstream value of f_p is much more simply interpreted in terms of f_p or $2f_p$ emission from a remote upstream foreshock source, that happens to be near f_p downstream of the shock crossing, or an unrelated

background source (e.g., Jovian continuum radiation). Generation of coherent radiation in the regions downstream of shocks is therefore not considered further below.

23.4 Possible Shock-Driven Radio Emissions

This section addresses solar system radio emissions that are believed to be associated with shocks, but for which definitive evidence of the shocks does not exist. The sources range from the solar corona to the outer boundaries of the solar system.

23.4.1 Coronal Shocks: Type II Bursts

Coronal type II bursts were discovered almost 50 years ago at metric wavelengths as the slow drift counterpart to the fast-drift emissions categorized as type III bursts (Wild 1950; Wild and McCready 1950). Figures 23.12 and 23.13 show modern examples of coronal type II bursts. Type IIs were rapidly interpreted in terms of f_p and $2f_p$ emission associated with a shock, since the "exciter" speeds inferred from the frequency drift rates and standard coronal density models obtained from eclipse data (Baumbach 1937; Allen 1947) were of order 500−2,000 km s^{-1} and so commensurate with a low multiple of the Alfven speed (Wild 1950). In contrast, type IIIs have exciter speeds of order 0.1−1 times the speed of light. Shocks are therefore the most plausible exciters of type II bursts.

Identification of type II bursts is not always easy, or even consistent between people interpreting the same data set or the same event observed by different instruments (Cane and Erickson 2005). Many reasons exist, including (1) the frequent superposition of multiple radio bursts in large events (see the schematic of solar activity in Fig. 23.14), especially type IIIs onto a type II, (2) multiple type IIs sometimes occur simultaneously during an event, with overlapping signatures in frequency-time space, including fine structures, (3) the frequency domains of groups of weak type IIIs sometimes drift at a similar rate to a metric type II and can be misidentified as a type II event (Cane et al. 2003), and (4) it is very difficult to identify weak intermittent emissions, events with large intensities that saturate the standard data displays, and weaker emissions during intense events, all of which can apply to type IIs. Moreover, while the existence of multiple classes of fine structures on metric type II bursts sometimes makes event identification simpler, these fine structures can sometimes complicate event interpretation instead. Figure 23.13 shows a coronal type II event with several overlapping sets of bands, changing drift rates, fine structures, and other radio bursts.

Cane and Erickson (2005) state that they definitely identify metric type IIs by requiring harmonic structure for an event with a suitably slow drift rate and duration (e.g., 2–10 min in the frequency range ≈ 300–30 MHz), supplemented if required by the fine structures defined below. This rests on the work of Roberts (1959) and Prestage (1994). Roberts stated "Harmonic structure is clearly visible in 60 percent of the bursts recorded and in an even higher percentage

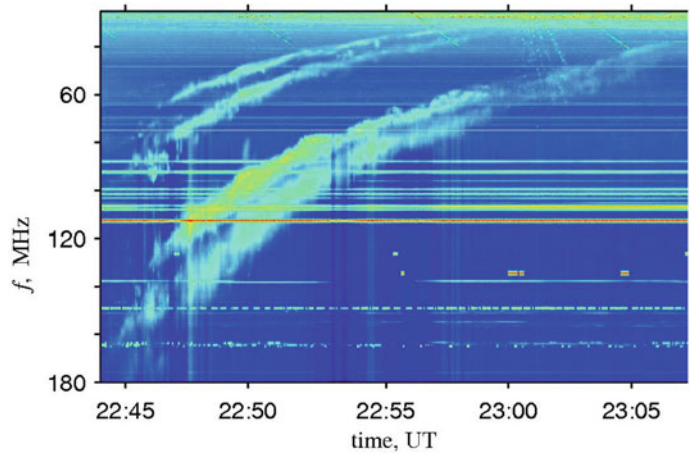

Fig. 23.12 A metric split-band type II solar radio burst (Lobzin et al. 2008) generated in the solar corona. Both fundamental and harmonic bands are clearly evident, each split in two, and the emission in a given band is significantly time variable and blobby

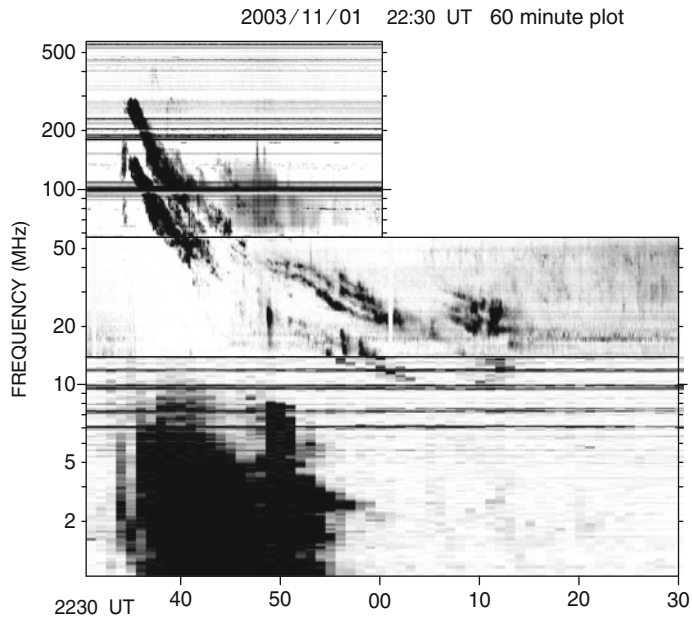

Fig. 23.13 A type II event with two main sets of bands (note the second set starting near 2310 UT), split-band fine structure, and significant changes in drift-rate (Cane and Erickson 2005). The emission in a given band is significantly time variable (blobby). Type III solar bursts are visible near 2235 UT for 80–180 MHz and for the period 2235 – 2300 below 10 MHz

of those bursts which are of at least moderate intensity and consist of well defined ridges". Prestage (1994) characterized all 69 type II bursts observed by the Culgoora digital spectrograph from June 1992 to June 1994, whence Cane and Erickson (2005) concluded: (1) 83% of the events had both fundamental and harmonic bands and (2) none of the remaining events were very intense and more than half occurred at low enough frequencies that the fundamental band was likely below Culgoora's observing limit. Accordingly it appears that harmonic structure is a crucial criterion for identifying an event as a metric type II burst.

While metric type IIs were rapidly interpreted in terms of f_p and $2f_p$ radiation produced by the plasma emission mechanism by electrons accelerated at a shock wave (Wild 1950; Wild and Smerd 1972; Nelson et al. 1985), more detailed models were developed slowly. The first detailed qualitative model for why the shock-accelerated electrons should form beam distributions that drive Langmuir waves and so f_p and $2f_p$ radiation is the foreshock model of Cairns (1986a). It involves "cutoff" distributions produced by time-of-flight effects, exactly as for Earth's foreshock (Filbert and Kellogg 1979; Cairns 1987a) and interplanetary type II bursts (Knock et al. 2001). Exten-

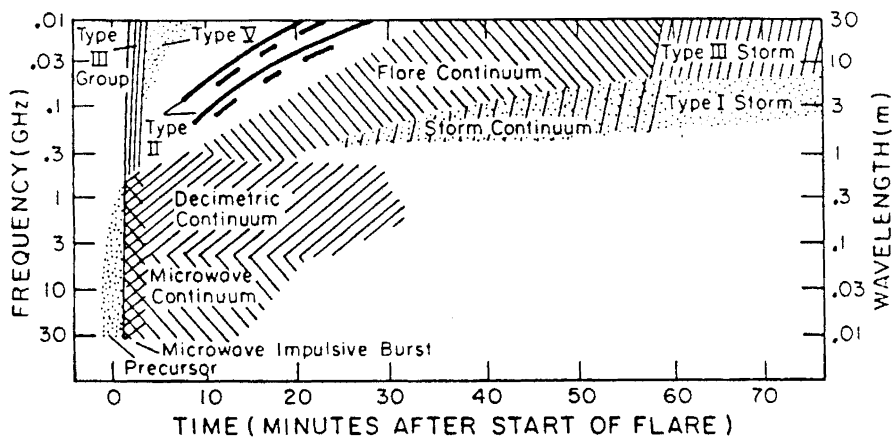

Fig. 23.14 Schematic of the classes of solar radio bursts (Suzuki et al. 1985)

sions of the foreshock theory are presented in detail in Section 23.6, for both coronal and interplanetary type IIs, and are not discussed further in this subsection. Instead, the remainder of this subsection addresses the fine structures of metric type IIs, the origin of the shock waves, the connections between coronal and interplanetary type IIs, and recent work on metric type IIs.

23.4.1.1 Fine Structures of Metric Type IIs

There are several accepted fine structures for metric type IIs. First, "split-bands" in which the fundamental and harmonic bands of a type II are each split in 2, with a frequency difference of order 10–20% (meaning $\Delta f/f \approx 0.1$–0.2) and close mimicking of variations in the corresponding split fundamental and harmonic band. Figure 23.12 shows a classic split-band event. Second, "multiple lane" events in which multiple sets of type II-like bands exist with different frequency separations, drift rates, and start and end times. Third, "herringbone bursts" are sometimes superposed onto the type II band (or "backbone"), comprising bursts that start on the type II band and drift rapidly towards higher and/or lower frequencies with drift rates commensurate with type III bursts (Roberts 1959; Cane et al. 1981). Herringbone bursts have a different frequency-time shape than type IIIs, with decreasing duration at increasing frequency difference from the type II band, whereas the duration of a type III burst increases with increasing frequency offset from its starting frequency (Cairns and Robinson 1997).

Split-bands are sometimes interpreted in terms of plasma emission from both upstream and downstream of the shock, with the frequency difference allowing the shock's Alfven Mach number to be constrained (Smerd et al. 1974; Vrsnak et al. 2002). However, as pointed out above, there is no accepted theoretical model or observational evidence for plasma emission from the downstream region. Another simple interpretation is that the bands arise from distinct spatial regions with slightly different plasma density encountered by the shock (McLean 1967). Explicit calculations show that the foreshock theory of type II bursts can indeed account for some split-band features in this way (Knock and Cairns 2005). However, finding that the splitting is commonly $\Delta f/f \approx 0.1$–0.2 and does not appear to have a larger range of observed values is a difficulty for this interpretation due to the corona being strongly inhomogeneous.

Another interpretation, based on observations of fine-structures regularly spaced at $f_{ce}/2$ in f_p radiation upstream of Earth's foreshock (Cairns 1994), is that split-bands involve splitting by $f_{ce}/2$ for the fundamental band (e.g., the split bands are close to f_p and $f_p + f_{ce}/2$) and f_{ce} for the harmonic band (e.g., bands at $2f_p$ and $2f_p + f_{ce}$) (Cairns 1994). If correct, then the frequencies of split-band type IIs contain information on the spatial profiles of both $n_e(\mathbf{r})$ and $B(\mathbf{r})$ in the corona. The standard 10–20% splitting of type II bursts then implies $f_{ce}/f_p \approx 0.05$–0.2 in the source region, which appears reasonable and might provide a qualitative explanation for the limited range of values $\Delta f/f$ for the splitting. This interpretation is discussed further in Section 23.6 below.

Multiple-lane events are simply interpreted in terms of emission from distinct source regions on the macroscopic shock (McLean 1967; Cairns and Knock 2006). These source regions then can have different plasma densities, propagation speeds, and Alfven Mach numbers for the shock, allowing the emissions to sometimes appear separate and drift at different rates and sometimes drift at the same rate but with an offset in frequency. In addition, several distinct shocks could be produced in an event, including a blast-wave shock and one driven in front of a CME, and produce multiple sets (or lanes) of emission features.

A widely-accepted and detailed theoretical interpretation for herringbone bursts does not exist. Qualitatively, however, they are accepted to involve fast streams of electrons accelerated at the shock and radiating via the plasma emission mechanism. One model involves unusual values of θ_{bn} (Holman and Pesses 1983) while another involves interaction of the shock with a localized coronal structure (e.g., a current sheet) which leads to impulsive, short-duration, acceleration of unusually large numbers of electrons by a localized region of the shock (Cairns and Robinson 1997).

In addition to these fine structures, type IIs are sometimes interpreted in terms of multiple shocks moving through the corona. These can produce emissions that sometimes overlap and cross in frequency-time space but sometimes follow one another in time along similar tracks (see Fig. 23.13). Usually these are not regarded as a fine structure but instead simply as separate type II bursts.

Another fine structure that is obvious in metric type IIs, but rarely discussed as a fine structure, is the intermittent and blobby nature of the emission. Sometimes type IIs appear "wispy", with intermittent broadband emission in multiple separated time periods that form the envelope of the type II band (e.g., Klassen et al. 1999; Mel'nik et al. 2004). This fine structure is clear in Figs. 23.12 and 23.13. It requires explanation.

The last fine structure sometimes considered is emission at the third and higher harmonics, as observed rarely for Earth's foreshock radiation (Cairns 1986b). Although this is controversial, Kliem et al. (1992) make a good case for third harmonic structure (in conjunction with fundamental and second harmonic bands) in one very strong type II burst. Arguably, however, definitive evidence for this fine structure does not yet exist.

Finally, consider the observations that (1) groups of weak type IIIs sometimes drift at a similar rate to a metric type II and can be misidentified as a type II event (Cane et al. 2003) (2) some low-frequency events identified as type IIs appear to contain fast-drift fine structures reminiscent of type IIIs (Mel'nik et al. 2004), and (3) some type IIIs show significant changes in intensity when their frequency-time tracks cross a type II burst and the type III electrons cross the type II shock (an increase-decrease-increase profile with decreasing frequency) (MacDowall 1989). New qualitative interpretation for these three phenomena are: (i) Some type IIIs become detectable only when the beam electrons reach the near vicinity of a radio-quiet shock that is unable to produce type II emission, so that repeated beam injections lead to repeated fast drift bursts whose observable envelope drifts in $f - t$ space at the rate corresponding to the shock, thereby mimicking a type II burst but being composed of fast-drift elements; (ii) Other type IIIs will be detectable before the electrons encounter the shock, but will have changes in intensity as the electrons move from the downstream region into the upstream plasma, being directly relevant to MacDowall's events (MacDowall 1989). Recent simulations of type III bursts (with quasilinear electron-Langmuir wave physics and the standard nonlinear processes discussed in Section 23.5) show strong intensity variations when beam electrons enter localised increases or decreases in T_e or T_i (Li et al. 2010). Further work is required to confirm or reject these interpretations.

23.4.1.2 Origin of Shocks and Connections to Interplanetary Type IIs

Two classes of shocks have been proposed to produce observable metric type II bursts: (1) blast wave shocks associated with flares and other explosive events, and (2) "piston-driven" shocks ahead of CMEs. It is now accepted that essentially all interplanetary type IIs are associated with CMEs (Cane and Stone 1984; Cane et al. 1987; Reiner et al. 1998; Reiner 2000; Gopalswamy et al. 2000; Gopalswamy 2006; Vrsnak and Cliver 2008). However, the situation for metric type IIs is not clear.

An important issue is that the term CME is usually defined in terms of coronagraph observations, which often do not cover the height range $< 2 \times 10^8$ m $\approx 0.3 R_S$ (where $R_S = 7 \times 10^8$ m is the solar radius) of flare sites or metric type II bursts. Note that $f_p > 100$ MHz for $r < 1.5 R_S$ for the Baumbach-Allen density model, for instance. Moreover, shocks take time to develop and become observable (Vrsnak and Cliver 2008). A blast-wave shock is also expected to weaken and eventually become unobservable, as it propagates and loses energy by heating and accelerating the downstream plasma.

Clear evidence exists for large amplitude waves with speeds $\approx 1{,}000$ km s^{-1} excited by flares, in the form of Moreton waves in the chromosphere (Moreton 1960) and their counterparts in the corona at EUV, X-ray, and other wavelengths (Moses et al. 1997; Thompson et al. 1998; Narukage et al. 2002; Khan and Aurass 2002; Vrsnak and Cliver 2008). Case studies of multiple sets of events observed at multiple wavelengths (Warmuth et al. 2004a, b) argue for a common flare origin. Moreover, the classic Uchida "sweeping skirt" model accounts for Moreton waves as the chromospheric signature of a fast-mode blast-wave MHD shock that produces the associated metric type II burst (Uchida 1974).

Arguments exist for and against type IIs being associated with blast wave shocks or CME-driven shocks. These arguments are reviewed in detail elsewhere (Cane and Erickson 2005; Cliver et al. 1999, 2004; Mancuso and Raymond 2004; Vrsnak and Cliver 2008) and no attempt is made here to review or justify them. For example, though, arguments against all metric type IIs having CME-driven shocks include the metric emission often apparently coming from behind the leading edges of CMEs, the exciter speeds inferred

from the drift rates of metric type IIs differing greatly from the speeds of associated CMEs, and the absence sometimes of observable CMEs for a given type II (Cane and Erickson 2005; Vrsnak and Cliver 2008). Similarly, arguments against all metric type IIs having a blast-wave shock include the high correlations between metric type IIs and fast CMEs and the poor correlation between flare size and type II occurrence (Cliver et al. 1999; Cane and Erickson 2005). It is noted that there are significant difficulties in removing projection effects, viewing, and obtaining speeds for Earth-directed CMEs (Mancuso and Raymond 2004), while the shock speeds extracted from radio data depend heavily on the density model adopted. In addition, the regions of the shock emitting observable radiation need not be at the nose of the shock, but instead near the flanks (Stewart and Magun 1980), since it is regions where **B** is close to perpendicular to the local shock normal that are favoured (Stewart and Magun 1980; Holman and Pesses 1983; Cairns 1986a; Knock et al. 2001). Coupling the foreshock type II theory with simulations of shocks evolving in data-driven models of the inhomogeneous solar corona, and then comparing the predicted dynamic spectra with observations, will help resolve this issue. Progress on such simulations is described in Sections 23.5 and 23.6 below.

Perhaps the clearest argument as to whether all metric type IIs are produced by CME-driven shocks, as interplanetary type IIs are accepted to be, would be if it was routine for the shock to continuously produce radio emission into the interplanetary medium so that the metric type II burst can be followed continuously through the decametric band (e.g., 100 – 1 MHz) into an interplanetary type II burst. Multiple observational searches for this have occurred and it is now clear that this must be exceedingly rare, if it ever happens. Figure 23.15 shows a metric type II band from ≈ 180 MHz near 2248 UT that extends down to 2259 UT near 38 MHz and an interplanetary type II that starts near 9 MHz at 2252 UT (Cane and Erickson 2005). It is evident that the coronal and interplanetary type IIs do not connect in this event, due to simultaneous emission at widely different and non-harmonically related frequencies. This event therefore requires two separate shocks for the coronal and interplanetary emissions and argues against a CME-driven explanation for both phenomena (Cane and Erickson 2005).

As a counterpart to Fig. 23.15, consider Fig. 23.16: it shows a metric type II that continues from ≈ 80 MHz (not shown) near 0515 UT down to at least ≈ 1.8 MHz near 0720 UT (Cane and Erickson 2005), also studied by Cliver et al. (2004). An emission interpretable

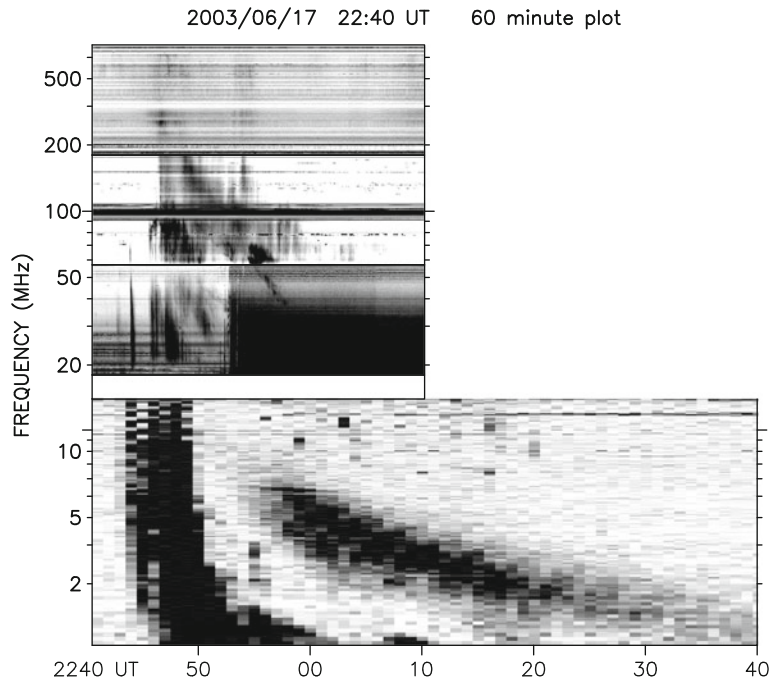

Fig. 23.15 A coronal type II and a interplanetary type II that do not connect (Cane and Erickson 2005). See the text for more details

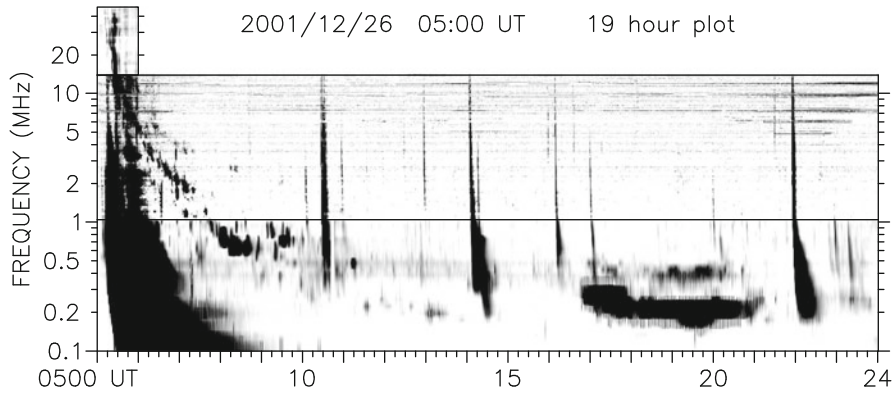

Fig. 23.16 Emissions that are interpretable as a coronal type II and a interplanetary type II and which are at least close to overlapping in frequency and time (Cane and Erickson 2005). The connection and interpretation of the emissions are discussed in the text

as an interplanetary type II is present from ≈ 0730 UT at a frequency just above 1 MHz, continuing intermittently until about 1000 UT, then between 1130 and 1400 UT and then between 1700 and 2130 UT. Cane and Erickson (2005) believe that the "interplanetary" emission after about 0720 is not connected to the metric emission, because the interplanetary event clearly starts at a measurably lower frequency than the last remnant of metric emission. Here the difference in frequency is less than a factor of 2, arguably being about a factor of 1.5 in Cane and Erickson's Fig. 12 (as opposed to their Fig. 13 shown here as Fig. 23.16), but they interpret the initial interplanetary emission as harmonic rather than fundamental as for the metric type II. On the other hand Cliver et al. (2004) interpret the same event as clear evidence of continuation of a metric type II into an interplanetary type II.

Detailed inspection of Fig. 23.15 shows many similarities between the metric and interplanetary type II emission present, including their intermittent and blobby nature and their organization into fundamental and harmonic bands. In this reviewer's opinion, however, the detailed relationship between the two emissions is not clear. The two emissions arguably overlap in time. However, if these data were clearly in the metric domain then the obvious interpretations would be in terms of either multiple lanes or two contemporaneous shocks. It would be good to perform detailed analyses of these data in inverse frequency – time space (i.e., $1/f - t$ space), as in Reiner et al. (1998), Reiner (2000), and Lobzin et al. (2008), so as to test these two interpretations. However, this reviewer's opinion is that the single (CME-driven) and two shock (CME-driven and blast wave) interpretations both remain viable for this event and cannot be ruled out, contrary to both earlier claims.

In summary, at this time no consensus exists on how to resolve these issues and the apparently contradictory arguments as to whether any metric type IIs continue into the solar wind, whether all type IIs (coronal and interplanetary) are produced by CME-driven shocks, and whether both. Perhaps, however, it is time to dispense with the either/or approach, favored though it is by Occam's Razor, and consider whether both types of shocks can occur and produce observable emission (i.e., be "radio-loud") in events, usually one at a time but occasionally both simultaneously. Put another way, might some metric type IIs be produced by blast-wave shocks, some by CME-driven shocks, and some involve multiple nearly simultaneous bands associated with one (or more) shock of each type? Perhaps the strongest arguments for this approach are that on one hand it appears certain that only very rarely, if ever, does a metric burst continue directly into an interplanetary type II burst, while on the other hand all interplanetary type IIs are accepted to be driven by CMEs. Even if one argues that the conditions for production of observable type II radiation are rarely met in the corona and solar wind, consistent with theory (Holman and Pesses 1983; Nelson et al. 1985; Knock et al. 2001, 2003a, b; Knock and Cairns 2005; Cairns and Knock 2006) summarized in Sections 23.5 and 23.6, the evident rarity of type IIs continuing from the corona into the solar wind is prima facie evidence for two different classes of shocks in most events, while the strong correlation with CMEs is prima facie evidence for CME-driven shocks playing a strong role.

23.4.2 Drifting Pulsating Structures

High-frequency observations (600 – 2,000 MHz) reveal intense solar radio emissions in association with flares and associated magnetic reconnection events, including the ejection of plasmoids (Karlicky 2003; Karlicky and Barta 2004). Many additional emissions are observed from 1 to 20 GHz, e.g., Wang et al. (2001) and Yan et al. (2001). Figure 23.17 shows multiple radio and microwave events covering the domain 4.5 GHz – 40 MHz, in association with a soft X-ray event that started near 0939 UT, peaked near 1,028 UT, and ended near 1049 UT (Karlicky 2003). A strong metric type II burst is evident below about 300 MHz from about 1016 – 1023 UT, implying a shock is present. Multiple fast-drift type III-like emissions are observed across the domain 200 – 4,500 MHz from about 1014 – 1023 UT, but attention is focused here on two so-called drifting pulsating structures: the first from 1016:00 – 1017:30 UT for 450 –1,000 MHz and the second stronger event from 1017:20 – 1022:00 UT in the range 450 –1,500 MHz (Karlicky 2003; Karlicky and Barta 2004). The intense portion of the second event has a clear drift in frequency, albeit with several weaker broadband bursts that extended to higher frequencies and appear to be superposed. The intense portion of this event is strongly reminiscent of the contemporaneous metric type II burst, only at about 6 times the frequency. Significant circular polarizations were sometimes observed, particularly at higher frequencies.

At a glance it is attractive to interpret the intense portions of the drifting pulsating structures, especially the second which strongly resembles the contemporaneous type II burst, in terms of a travelling shock. The interpretation adopted (Fig. 23.18) involves magnetic

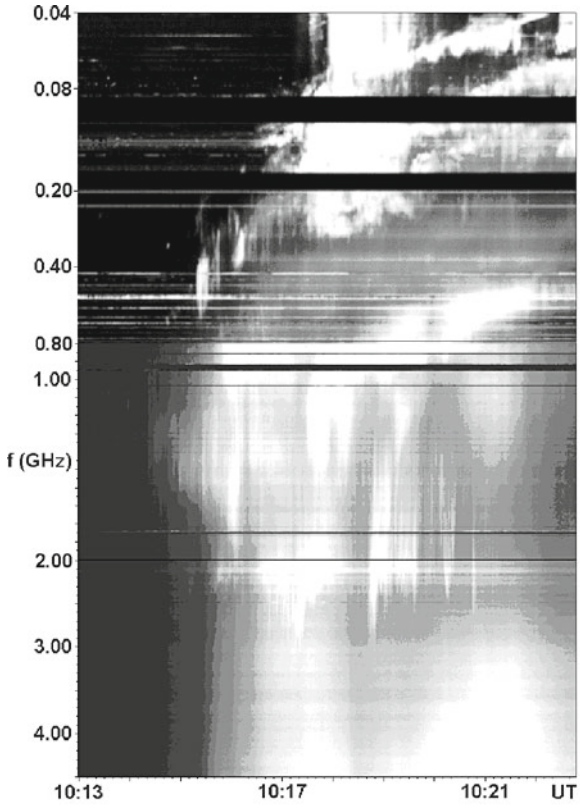

Fig. 23.17 Metric and decimetric spectra of the 12 April 2001 event of Refs. Karlicky (2003); Karlicky and Barta (2004). A type II burst is observed above 400 MHz and two drifting pulsating structures are observed in the range 450 – 1,500 MHz, the second of which strongly resembles the type II burst. See text for details

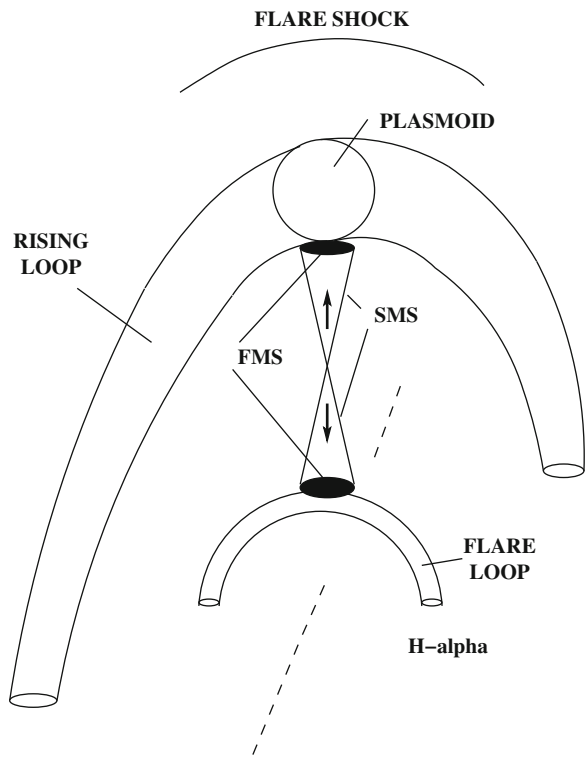

Fig. 23.18 Model of Karlicky and Barta (2004) for interpreting drifting pulsating structures. Fast outflows from magnetic reconnection regions, which develop at current sheets between rising and flare loops, are shown with arrows. SMS refers to a slow mode MHD shock and FMS to a standard fast-mode MHD shock

reconnection at multiple current sheets between an underlying flare loop and higher loops, leading to fast outflows (Karlicky and Barta 2004). Slow mode shocks are predicted to be formed as part of the standard structure of the reconnection outflow region, along the "side" boundaries, while fast mode shocks develop where the reconnection outflows impact the rising and flare loops (called "termination" shocks). A plasmoid may develop as part of the reconnected rising loop. The frequency drift of the decimetric emissions is interpreted in terms of one or more loops or the plasmoid rising, with associated motions of the shocks and the reconnection sites. With loops participating in the reconnection process the structure can continue to rise and produce drifting radio emission, with fine structures related to the time variations in the multiple-loop system. Karlicky and Barta (2004) specifically point out that one event (their Fig. 18) had fine structures that strongly resemble herringbone fine structures on type II bursts, a further argument that a shock is involved.

Karlicky and Barta (2004) state that the radiation is produced by the plasma emission mechanisms as a result of fast electron beams accelerated at these shocks. They then used the radiation frequency to constrain the plasma density in the multiple-loop system. These authors did consider several models for radio fine structures, most involving upper hybrid waves driven by temperature anisotropies and then linear mode conversion, rather than the standard "plasma emission" mechanisms involving electron beam-driven Langmuir waves and nonlinear radiation processes involving Langmuir waves. Extension of the Knock et al. model for type II bursts (Knock et al. 2001; Knock and Cairns 2005) to these emissions would be useful in establishing the need for non-standard emission mechanisms and in quantitatively modelling drifting pulsating structures and other decimetric emissions.

23.4.3 Outer Heliospheric Radio Emissions

In 1983 the two Voyager spacecraft were beyond the orbit of Saturn and separated by several astronomical units (AU) when they observed radio emissions at frequencies $f \approx 2$–3 kHz with very similar dynamic spectra (Kurth et al. 1984). Figure 23.19 is a recent dynamic spectrum of these emissions from 1982 until July 2009, showing the emission frequency versus time with the intensity color coded. It was obtained from the Voyager Plasma Wave Subsystem (PWS) site http://www-pw.physics.uiowa.edu/w̃sk/vgr/recent.html, courtesy of D.A. Gurnett and W.S. Kurth, and is similar to figures in other publications (Kurth et al. 1987; Gurnett et al. 1993, 1998). The intense and continuous red band near 2.4 kHz is interference from Voyager 1's power supply system. The signals below 1 kHz at all times, and the diffuse light blue signals below 2 kHz from 1982 to mid-1992, are dominated by interference from other instruments and spacecraft and systems. The signals of interest here are the three relatively intense, longlasting episodes of emission from ≈ 1.8–3.6 kHz (1983–1984, 1992–1995, and 2003–2004), together with weaker events (e.g., early 1986, late 1989, and late 1991) in the same frequency range. Note that these major episodes are separated by an approximately 9–10 year period, reminiscent of the solar cycle, and that the third outburst started in mid-2003 and was relatively short-lived.

Figure 23.20 summarizes the plasma regions and discontinuities expected in the outer heliosphere (Zank 1999; Izmodenov et al. 2004). The superalfvenic, supersonic solar wind plasma undergoes a shock transition at the termination shock, as recently observed by Voyagers 1 and 2 at heliocentric distances of 91 and 84 AU, respectively (Stone et al. 2005, 2008). The inner heliosheath contains shocked solar wind plasma, which is slowed to speeds ≈ 100 km s^{-1}, compressed by a factor ≈ 2–4, heated to temperatures $\approx 10^6$ K, deflected in direction, and the magnetic field amplified and rotated, at the termination shock. Analogous to the terrestrial magnetopause, the heliopause is a rotational discontinuity between the inner and outer heliosheaths that separates the shocked solar wind plasma from interstellar plasma. Finally, if the solar system moves superalfvenically or supersonically, then the VLISM plasma will be shocked at a bow shock, and modified similarly to the solar wind at the termination shock. The outer heliosheath contains the VLISM plasma processed by the bow shock (or a bow wave if the flow is subsonic and subalfvenic).

Kurth et al. (1984) interpreted the radio waves as originating in the outer heliosphere and, most likely, a signature of the solar wind's interaction with the very

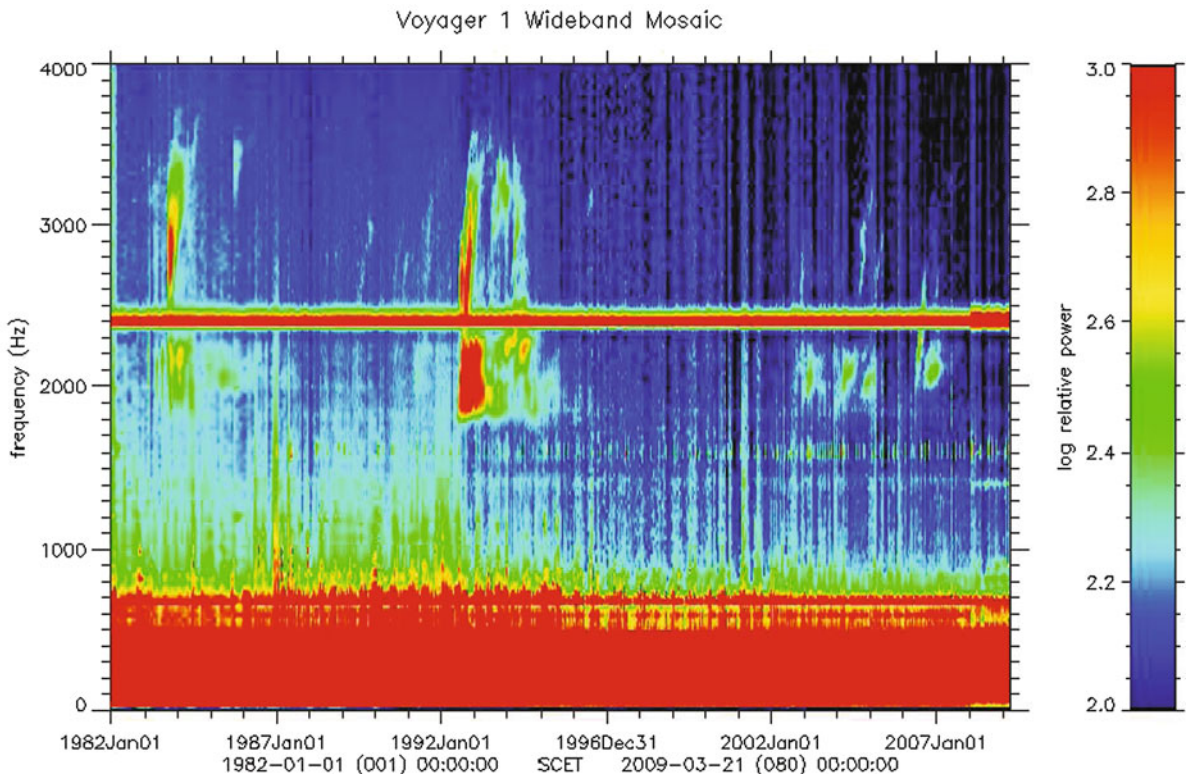

Fig. 23.19 Voyager 1 dynamic spectrum for the period 1982–2009. Major episodic radiation events are visible, as well as weak drifting events. See the text for more details

local interstellar medium (VLISM). Now the favored interpretation is that the radiation is produced beyond the heliopause by shocks moving away from the Sun in front of global merged interaction regions (GMIRs) resulting from solar activity (Gurnett et al. 1993; Gurnett and Kurth 1996; Cairns and Zank 2001, 2002; Mitchell et al. 2004).

The Voyager emissions can be categorized into two classes (Kurth et al. 1987; Cairns et al. 1992; Gurnett et al. 1993), as illustrated by Figures 23.19 and 23.21: (1) The "2 kHz component", which remains in the frequency range 1.8–2.6 kHz, is longer lasting ($\approx$ 3 years), and does not drift significantly in frequency. (2) "Transient" or "drifting" emissions which drift up in frequency, have a range of starting and ending frequencies within the domain 1.8–3.6 kHz, frequency drift rates in the range $\approx$ 1–3 kHz/year, and last for $\approx$ 100–300 days.

Clear evidence exists for frequency fine structures in both the 2 kHz component and the transient emissions, particularly for the latter. For instance, Fig. 23.19 and 23.21 show that the transient emissions during 1994 often occurred as pairs of signals with very similar drifts that are offset in frequency. This "pairing" characteristic is not understood but is reminiscent of split-band and multiple-lane type II solar radio bursts (Wild et al. 1963; Nelson and Melrose 1985) discussed in Section 23.4.1 above. Possible interpretations include the shock moving across 2 regions with slightly different densities or the splitting being an intrinsic feature of the emission process. It is worth pointing out that the density profiles in the heliosheath and heliopause are predicted to be asymmetric about the relative VLISM-Sun velocity vector $\mathbf{v}_{VLISM}$, due to the influence of the interstellar magnetic field (Pogorelov et al. 2009; Opher et al. 2009a). These density asymmetries may be directly relevant to the observed pairing. If, however, the splitting is assumed to be intrinsic and at half the electron cyclotron frequency, as for some rare events of f_p emission in Earth's foreshock (Cairns 1994), then the inferred magnetic field is $\approx$ 20 nT. This appears to be unrealistically large.

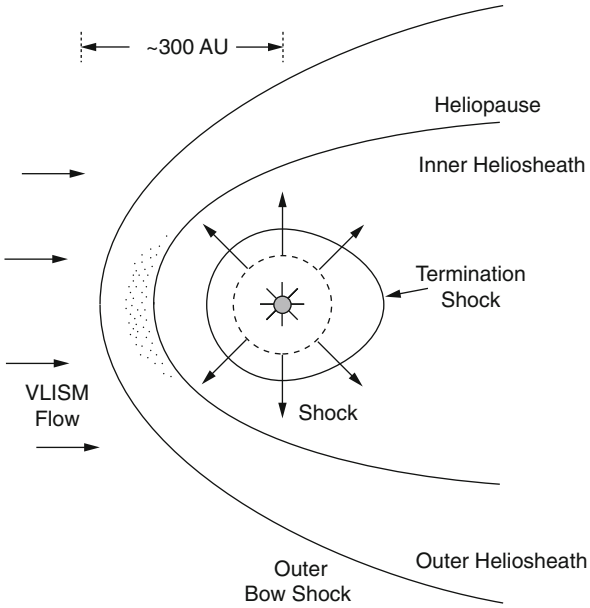

Fig. 23.20 Major plasma regions and boundaries expected for the solar wind – VLISM interaction. The *dashed line* denotes a GMIR shock moving outwards. The *dotted region* shows the source region predicted for the Voyager emissions by the GMIR model and Priming/GMIR theory (Cairns and Zank 2002)

Following earlier work on event triggers (McNutt 1988; Grzedzielski and Lazarus 1993), Gurnett et al. (1993) postulated that the episodic radio bursts are produced when global merged interaction regions (GMIRs) cross the heliopause. GMIRs are formed by the merging of multiple interacting CMEs and other fast plasma flows produced by solar activity into a global disturbance of the plasma density, magnetic field and flow speed that propagates outwards faster than the ambient solar wind. Figure 23.22 shows when multiple spacecraft observed the shock driven by the GMIR associated with the 1992–1994 radiation event, as well as the Forbush decreases in cosmic ray flux caused by cosmic rays being reflected and scattered by the enhanced and disturbed magnetic field of the GMIR material. Detection of these signatures by the widely separated Voyager and Pioneer spacecraft confirms that the disturbance was truly global.

Figure 23.23 confirms the association between large GMIRs and the major radio outbursts (Gurnett and Kurth 1995): the 1983–1984 and 1992–1994 outbursts are associated with the two largest Forbush decreases observed in the Deep River Neutron Monitor data. Moreover, the time-lag between the Forbush decreases at Earth and the radio onsets at Voyager are consistent, at 415 ± 4 days, and the two GMIR propagation speeds to Voyager were consistent at $\approx 830 \pm 20$ km s^{-1}. Using these speeds and time-lags, together with plausible estimates for shock slowing, Gurnett et al. (1993) estimated the source to be at a radial distance $R \approx$ 140–190 AU. These are plausible distances for the heliopause.

Recently Kurth and Gurnett (2003) combined GMIR time-of-flight effects with direction-finding and an amplitude-dependent triangulation technique to constrain further the distance and direction to

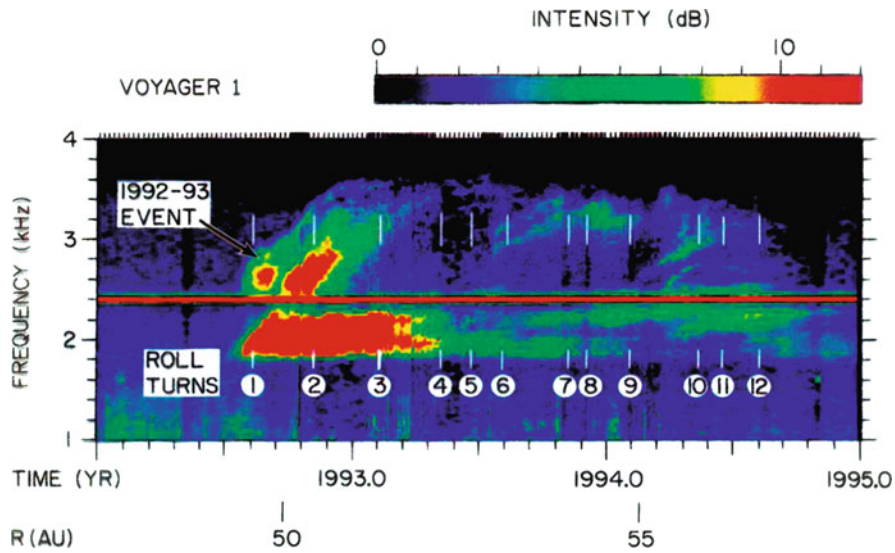

Fig. 23.21 Two classes of radiation event are demonstrated here for the 1992–1994 event (Gurnett et al. 1998): the "2 kHz component" and drifting "transient emissions". *Numbers* show the times of spacecraft rolls and associated direction-finding analyses discussed below

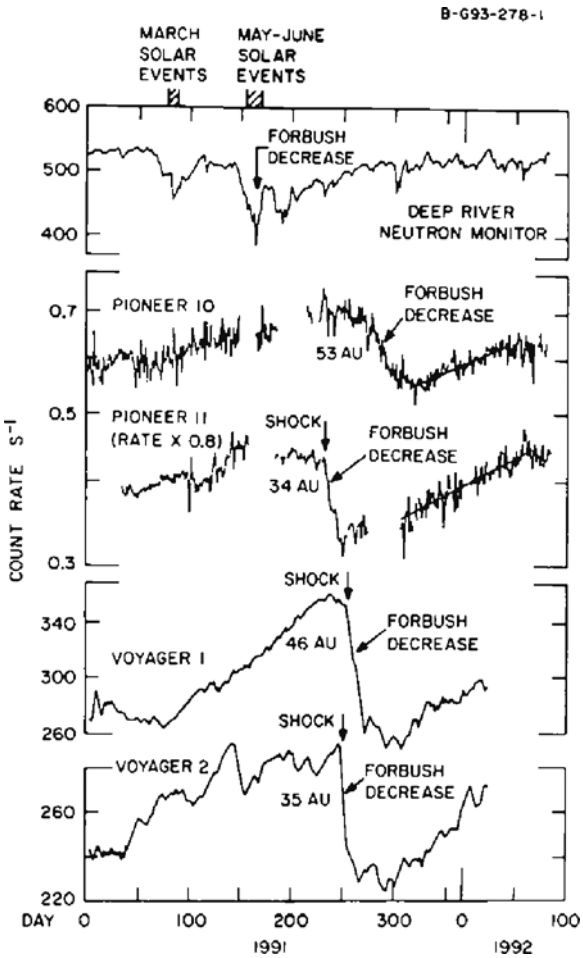

Fig. 23.22 Forbush decreases in cosmic rays caused by the GMIR and its shock at Earth and various widely separated spacecraft in the outer heliosphere for the 1992–1994 radio event (Gurnett et al. 1993)

the radiation source, extending earlier work (Gurnett et al. 1993, 1998). The three techniques yield simultaneous solutions for multiple observations of the transient emissions during the 1992–94 event, as shown in Fig. 23.24 as a function of galactic latitude and longitude (Kurth and Gurnett 2003). The results are clear. First, the source of the transient emissions is initially very close to the nose direction for the heliopause. Second, the source direction changes with time but lies along a line closely parallel to the galactic plane. Third, the source generally moves away from the nose direction and the modulus of its ecliptic latitude typically increases with time. The first and third of these results confirmed earlier analyses (Gurnett et al. 1993, 1998). A detailed physical explanation for these results was not attempted. However, it was speculated that the second result arises because the apparent source axis is aligned with **B** in the outer heliosheath, implying that **B** is parallel to the galactic plane. More recent work suggests a different interpretation (Gurnett et al. 2006; Cairns et al. 2006).

The radio emission is widely accepted to be f_p or $2f_p$ radiation produced upstream of a shock wave (Kurth et al. 1984; Gurnett et al. 1993; Cairns and Zank 2001, 2002). This means that the observed radiation frequency is a remote measure of the source density, thereby also constraining the source location. It is widely accepted that the observed radiation frequencies are inconsistent with f_p or $2f_p$ emission from the solar wind or inner heliosheath, but that a source in the outer heliosheath or VLISM is viable.

Before proceeding it is emphasized that a GMIR shock is not a sufficient condition by itself to obtain observable radio emission. The reason is that the Voyager spacecraft do not observe any local radio emission when the GMIR shocks pass over the Voyager spacecraft. Instead two conditions (or triggers) are required, first that a suitable GMIR shock exists, and second that the shock enters a plasma region where it is able to excite observable radio emission (Cairns and Zank 2001, 2002).

In summary, although in situ observations of the shock in the radio source do not yet exist, the observational evidence for the GMIR shock stimulating the emission beyond the heliopause is very strong. Current theory and interpretations of the 2–3 kHz emissions all involve this model, due originally to Gurnett et al. (1993). A review of theoretical research is provided in Section 23.7 below.

23.5 Theory

This section summarizes the standard theory for radio emission at f_p and $2f_p$ produced by shocks. It proceeds first by discussing the reflection and acceleration of electrons, then the formation of beam distributions, then the growth of and power flux into the Langmuir waves, and finally the production of f_p and $2f_p$ radio emission by specific nonlinear Langmuir wave processes. Each of these steps is illustrated with examples from either Earth's foreshock or interplanetary type II bursts.

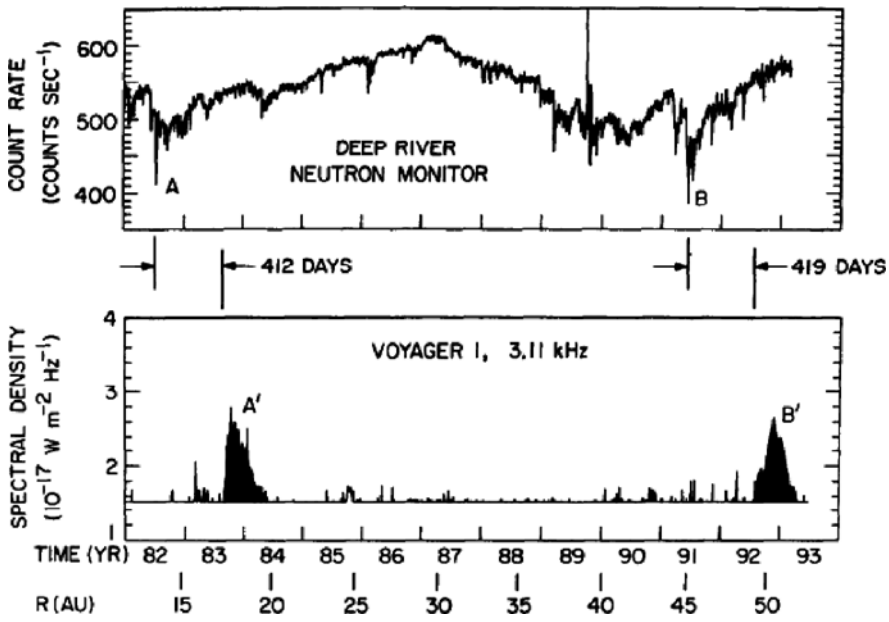

Fig. 23.23 Correlation between the largest Forbush decreases at Earth (A and B) and the major 2–3 kHz radio events (A′ and B′) (Gurnett and Kurth 1995)

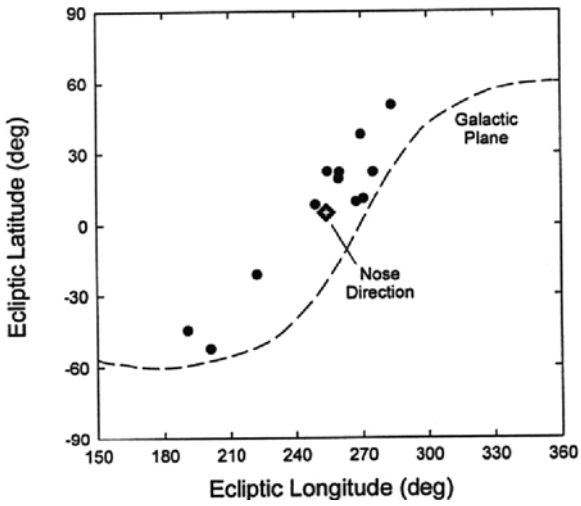

Fig. 23.24 Source directions of transient emissions as functions of [1950] ecliptic latitude and longitude derived from analyses of roll modulations, relative amplitudes between Voyagers 1 and 2, and GMIR-radio timelags (Kurth and Gurnett 2003). Sources start near the heliopause nose and typically move away with increasing time

23.5.1 Electron Motion, Reflection and Acceleration

In Figs. 23.1 and 23.6 the shock is stationary and the upstream plasma moves towards the shock at velocity $\mathbf{u}$, carrying magnetic field lines across an observer fixed relative to the shock. Accordingly, a convection electric field $\mathbf{E}_u = -\mathbf{u} \times \mathbf{B}_u$ exists in general (except when $\mathbf{u}$ and $\mathbf{B}$ are parallel): it acts on all charged particles and causes them to move with a mass and charge-independent drift velocity $\mathbf{v}_d = \mathbf{E}_u \times \mathbf{B}_u/|B_u|^2$ with $v_d = u|\sin\theta|$ where θ is the angle between $\mathbf{B}_u$ and $\mathbf{u}$. Put another way, $\mathbf{v}_d$ is the component of $\mathbf{u}$ perpendicular to $\mathbf{B}_u$.

Electron reflection is best described in the de Hoffman-Teller frame (Toptyghin 1980; Wu 1984; Ball and Melrose 2001), where the convection electric field vanishes. This frame moves along the shock front with speed $v_d \tan\theta_{bn}$, where θ_{bn} is the angle between the local shock normal and $\mathbf{B}_u$. Conservation of the magnetic moment and energy are assumed, the latter subject to the cross-shock potential $\phi_{cs}(\mathbf{r})$:

$$\frac{v_\perp^2(\mathbf{r}_1)}{B(\mathbf{r}_1)} = \frac{v_\perp^2(\mathbf{r}_2)}{B(\mathbf{r}_2)}\,, \tag{23.6}$$

$$m_e\left(v_\parallel^2(\mathbf{r}_1) + v_\perp^2(\mathbf{r}_1)\right) - 2e\phi_{cs}(\mathbf{r}_1)$$
$$= m_e\left(v_\parallel^2(\mathbf{r}_2) + v_\perp^2(\mathbf{r}_2)\right) - 2e\phi_{cs}(\mathbf{r}_2)\,, \tag{23.7}$$

respectively, where $\mathbf{r}_1$ and $\mathbf{r}_2$ are two locations. The magnetic field $\mathbf{B}(\mathbf{r})$ and potential ϕ_{cs} are then specified by a model, e.g., Eq. (23.4). Conservation of the

magnetic moment leads to a loss cone in the reflected electron distribution, which depends on the magnetic compression at the shock, as predicted by Wu (1984) and Fitzenreiter et al. (1990), among others.

The shock model used in applications to type II bursts, Earth's foreshock, and the 2–3 kHz emissions ignores the shock foot and overshoot/undershoot structures, instead assuming a simple linear ramp between the upstream and downstream states (Knock et al. 2001; Kuncic et al. 2002; Mitchell et al. 2004) specified by the Rankine-Hugoniot conditions (Kennel et al. 1985; Melrose 1985; Burgess 1995). Of particular relevance then are the magnetic mirror ratio B_d/B_u and corresponding change in ϕ_{cs} via Eq. (23.4), which depend upon the Alfven Mach number M_A, sonic Mach number M_S, and θ_{bn}. The potential modifies the shock's loss cone, determined by B_d/B_u, and makes it more difficult to reflect electrons with low $v_\parallel$ since it attracts all electrons downstream.

An important future extension of existing models is to include the effects of the magnetic and potential overshoots, which increase the magnetic compression ratio to a ratio $B_m/B_u > B_d/B_u$, decrease the loss cone, and result in significantly more reflected electrons. Yuan et al. (2007, 2008a) found factors of 2–4 increase in the number of reflected electrons for shocks with overshoots compared with non-overshoot shocks.

In the de Hoffman-Teller frame electrons with initial speed $v_\parallel^i$ upstream are reflected with parallel speed $v_\parallel^r = -v_\parallel^i$. Then, moving into the shock rest frame of Figs. 23.1 and 23.2 one finds

$$v_\parallel^r = 2v_d \tan\theta_{bn} - v_\parallel^i \,. \tag{23.8}$$

The associated change in energy is large when θ_{bn} is close to 90°. This increase in energy can be understood in terms of the shock's magnetic mirror reflecting the electron analogously to a ping-pong bat accelerating a ball, so the acceleration is sometimes called mirror reflection or fast Fermi acceleration (Wu 1984). Alternatively, in the shock's rest frame it is understood in terms of the electrons undergoing a ∇B plasma drift in the direction anti-parallel to the convection electric field, leading to the name shock drift acceleration (cf. Toptyghin 1980; Ball and Melrose 2001).

23.5.2 Formation of Electron Beams

Electron beams are formed in the foreshock by two effects (Cairns 1987a). The first is determined by the shock's effective speed along the magnetic field lines, leading to a minimum "escape cutoff" speed for which electrons can enter the foreshock (Cairns 1987a). The second is a time-of-flight effect that relates to motion of charged particles in the foreshock (Filbert and Kellogg 1979).

The escape cutoff forms beams because the shock moves along the magnetic field lines at an effective speed $v_\parallel = v_d \tan\theta_{bn}$, in the shock rest frame of Fig. 23.1. Accordingly only particles with

$$v_\parallel > v_c = v_d \tan\theta_{bn} \tag{23.9}$$

can outrun the shock and escape into the foreshock. This constraint determines a minimum cutoff speed $v_\parallel = v_c$, equal to the de Hoffman-Teller speed, for electrons to be able to leave the shock: this therefore naturally forms a beam of electrons with $v_\parallel > v_c$ upstream of any shock (Cairns 1987a), provided only that any electrons are able to escape upstream (which requires $v_c < c$).

The time-of-flight mechanism relies instead on the motion of charged particles in the foreshock. The kinematic motion of a charged particle in a locally homogeneous magnetized plasma can be described by

$$\mathbf{v}(t) = \mathbf{v}_\parallel + \mathbf{v}_g(t) + \mathbf{v}_d \,. \tag{23.10}$$

This particle moves with constant speed $v_\parallel$ along $\pm\mathbf{B}_u$, has the standard gyromotion $\mathbf{v}_g(t)$ with gyro speed v_g, and is subject to a constant drift velocity $\mathbf{v}_d$ perpendicular to $\mathbf{B}_u$ due to the convection electric field. Each particle then moves in a plane defined by $\mathbf{u}$ and $\mathbf{B}_u$, so the full 3-D problem of a set of particles moving in the 3-D foreshock can be broken into a set of calculations in a stack of 2-D planes, with each particle moving in a 2-D plane defined by $\mathbf{u}$ and $\mathbf{B}_u$.

Put another way, the particle gyrocenter moves along the line defined by $\mathbf{v}_\parallel + \mathbf{v}_d$. The slope of this line is defined by the ratio of $v_\parallel$ to v_d, with lines of larger $v_\parallel/v_d$ being more closely parallel to $\mathbf{B}$. Now consider a point (R, x) in the foreshock, where R is the distance along the tangent field line and x is the perpendicular distance along $\mathbf{v}_d$. The fastest electrons reaching

that point from the shock move approximately along a line parallel to **B**, while the slowest ones move along the line tangential to the shock that passes through (R, x). Even slower electrons cannot come from the shock, so the particle kinematics directly impose a a minimum $v_\parallel$ for shock-accelerated electrons reaching (R, x), thereby again imposing a cutoff on the electron distribution function and implying that a beam feature exists. For fast beams relatively close to the foreshock boundary the equation for the line directly gives (Filbert and Kellogg 1979; Cairns 1987a)

$$v_{\parallel,min} \approx v_d \frac{R}{x} = v_d \tan\theta_{bn} = v_c \,, \tag{23.11}$$

consistent with Eq. (23.9). Alternatively, this can be seen from the tangential nature of the path, which means that the particle path is parallel to the local shock surface and so $v_\parallel = v_c$.

Thus, electrons reaching a location in the foreshock from the shock, whether reflected upstream electrons or electrons leaked from the shock's downstream region, naturally have a beam distribution. This is imposed by two effects, the escape cutoff at the shock itself and the cutoff imposed by particle kinematics (time-of-flight effects) in the foreshock itself. Both yield the same cutoff in $v_\parallel$, as argued above. It should be recognized, however, that the electron reflection can cause the peak in the reduced electron distribution function $f_r(v_\parallel) = \int dv_\perp v_\perp f(v_\perp,v_\parallel)$ to be well above $v_\parallel = v_c$: the two cutoff effects impose a minimum $v_\parallel$ and beam character on $f_r(v_\parallel)$ but multiple beams are possible.

The variation of v_c along the shock surface and the spatial variation in v_c with R and x in Eq. (23.11) results in a significant variation in the foreshock beam speed. This speed is large near the foreshock boundary but $< c$ (there is actually a region downstream of the foreshock boundary that contains no reflected electrons, since $v_c > c$ there, if gyromotion effects are ignored) and decreases monotonically with increasing x and depth $DIFF = x/\sin\theta$. Thus the fastest beams are expected near the foreshock boundary, with the slowest beams deep inside the foreshock.

The kinematic cutoff effect can lead to electron beams rebuilding in the foreshock, particularly when faster electrons nearer the foreshock boundary are slowed by wave-particle interactions. Consider a group of such electrons: they leave their effective source region near the foreshock boundary with a reduced $v_\parallel = v_1$ and now move on particle paths (lines) that are more highly inclined relative to **B** than their original path, crossing the trajectories of some electrons with higher $v_\parallel$ that are coming directly from the shock and forming a beam at lower $v_\parallel$. This movement of electrons to foreshock regions they cannot access without energy loss corresponds to an effective rebuilding of the electron beam at speeds close to but below v_c (Cairns and Fung 1988) and might lead to multiple unstable beams at a given location.

As well as having beam-like character, foreshock electron distributions also should have loss cone features in the reflected electrons (imposed by the conservation of magnetic moment and energy in the de Hoffman-Teller frame, as discussed in Section 23.5.1), while leaked electrons will be found inside the loss cone (Fitzenreiter et al. 1990). Figure 23.9 shows the electron distributions in Earth's foreshock to have both beam and loss cone features [Fitzenreiter et al. 1984], as discussed in Section 23.3.2. The combination of a loss cone and a cutoff in $v_\parallel$ can form a well-defined ring-beam distribution, as found explicitly by Yuan et al. (2007, 2008a) using test-particle simulations.

The electron distribution functions $f(v_\perp,v_\parallel)$ and $f_r(v_\parallel)$ can be calculated using Liouville's Theorem (Cairns 1987a; Fitzenreiter et al. 1990; Knock et al. 2001; Kuncic et al. 2002). This involves tracing particle paths back to the shock, calculating B_d/B_u and ϕ_{cs} (without or with overshoots) on the spatially varying shock, unfolding the effects of the shock acceleration using Eq. (23.8), equating $f(v_\parallel^r,v_\perp)$ to the assumed upstream distribution $f_{in}(v_\parallel^i,v_\perp)$ (or the downstream distribution for leaked electrons), and then integrating over $v_\perp$ to obtain the f_r.

Figure 23.25 illustrates the reduced electron distributions $f_r(v_\parallel, R, x)$ at 4 locations upstream of Earth's bow shock, as well as bow shock and the particle paths to the 4 locations for the cutoff velocity and the maximum $v_\parallel$ calculated. Spatial coordinates (R, x) are used, with $\mathbf{B}_u$ oriented along the $+R$ axis and $\mathbf{v}_d$ oriented along the $+x$ axis. The top and bottom panels also state the average beam speed v_b, effective thermal width Δv_b, and number density n_b of the beam relative to the background electron number density. These are calculated by taking appropriate moments of f_r. Spatial

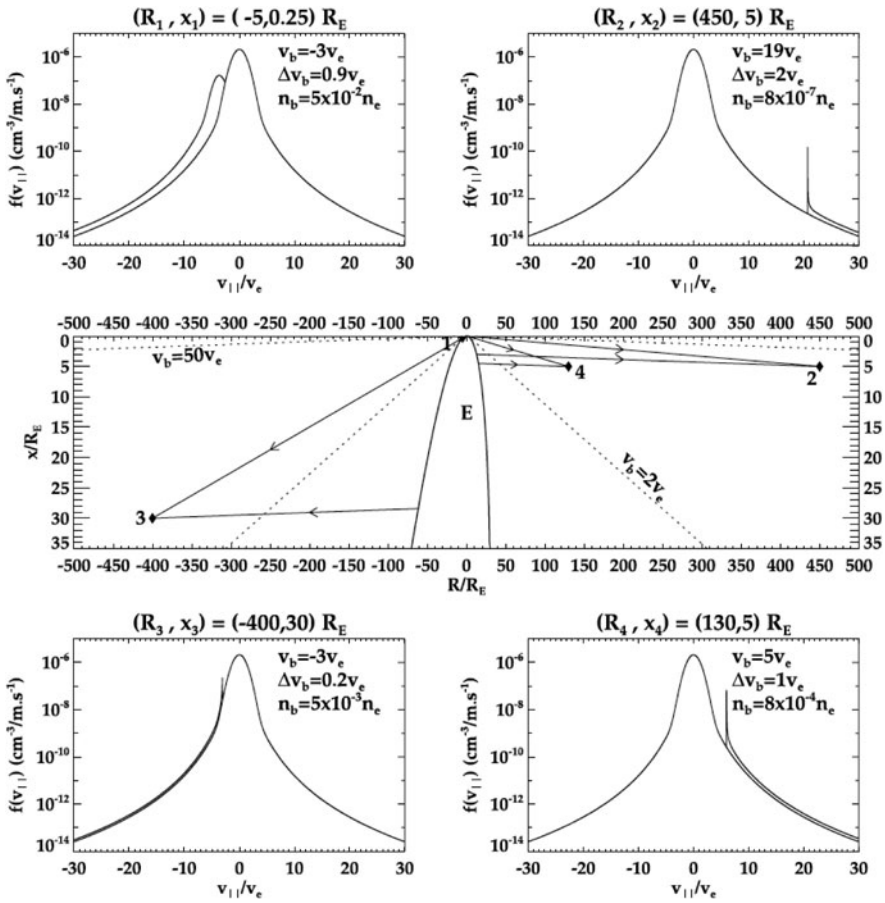

Fig. 23.25 Reduced electron distributions (*top* and *bottom panels*) at four locations in Earth's foreshock (Kuncic et al. 2004). The *middle panel* shows the Earth, bow shock, and particle paths corresponding to the cutoff speed and maximum $v_{\parallel}$ calculated, in (R, x) coordinates. The beam quantities v_b, Δv_b, and n_b quoted in the *top* and *bottom panels* are defined in the text

variations in v_c are evident, increasing with increasing R and decreasing x as predicted by Eq. (23.11), while n_b varies dramatically, being largest closer to the shock and for $v_b \leq 5V_e$, where V_e is the electron thermal speed. Beams are clearly evident in all 4 cases: the cutoff is dominant in determining the beam's character in all but the top left case, where variations in reflection efficiency along the shock determine the location of the peak in f_r.

Spatial variations in the $n_b(R, x)$, $v_b(R, x)$, and $\Delta v_b(R, x)$ have been calculated based on Liouville's equation and the above electron reflection and leakage physics (Fitzenreiter et al. 1990; Cairns et al. 1997). These are also used in Sections 23.5.3 and 23.5.4 below and existing predictions for type II bursts, Earth's foreshock, and the 2–3 kHz emissions (Knock et al. 2001; Knock and Cairns 2005; Cairns and Knock 2006; Florens et al. 2007; Kuncic et al. 2002, 2004; Cairns et al. 2004; Mitchell et al. 2004, 2005, 2009). In brief, $n_b(R, x)$ varies with v_b, R, and x, being zero at the upstream foreshock boundary, then increasing to a peak where $v_b \approx 3V_e$ for Earth's foreshock, and then decreasing again as v_b decreases and x increases for a given R. This is because the maximum energy gain for mirror reflection is limited to about a factor of 10 (Ball et al. 2001), so there is a balance between the energy gain factor via Eq. (23.8), its variation over the shock surface, and the fraction of incoming upstream electrons able to be accelerated to speeds of v_b or greater. In addition, n_b decreases as R increases, due to dilution of the total number of reflected electrons into an increasingly large foreshock volume. The fraction of the foreshock filled with beams fast enough and dense enough to drive significant Langmuir waves and radio emission, is therefore relatively small and typically found close to the tangent field lines, a $v_b \geq 3V_e$, and relatively close to the shock.

23.5.3 Growth of Langmuir Waves

Cutoff electron distributions thus naturally have a beam-like enhancement at high $v_\parallel$ and can drive Langmuir waves via the conventional electron beam or "bump-on-tail" instability (Filbert and Kellogg 1979; Cairns 1987b). The instability is driven by a positive gradient $\partial f_r(v_\parallel)/\partial v_\parallel$ of the reduced electron distribution function f_r and the growth rate is proportional to $\partial f_r(v_\parallel)/\partial v_\parallel$ evaluated at the wave phase speed. The characteristic growth rate γ_K of Langmuir waves resonant with the beam (meaning those with parallel phase speeds near v_b) is given by (Melrose 1985)

$$\gamma_K = \frac{n_b}{n_e}\left(\frac{v_b}{\Delta v_b}\right)^2 \omega_p. \tag{23.12}$$

Here n_e is the background electron number density (assumed $>> n_b$), $\omega_p = 2\pi f_p$, and small constants of order unity are neglected. Thus large growth rates are predicted for beams that are relatively dense, fast, and cold.

The energy for the Langmuir waves to grow comes from the electron beam, causing the electrons to move towards lower kinetic energy and $v_\parallel$. Quasilinear theory (e.g., reviews by Grognard 1985 and Melrose 1985) treats quantitatively the relaxation of the electron distribution function and the growth of the waves. Homogeneous quasilinear theory for a delta function beam (Melrose 1985) predicts that the system evolves to a state in which 2/3 of the initial beam kinetic energy $1/2 m_e n_b v_b^2$ goes to the waves and 1/3 is retained by the electrons, whose distribution function is flattened into a plateau in $v_\parallel$ space. This plateau has $\partial f_r/\partial v_\parallel = 0$ and so has zero growth rate for Langmuir waves. Warm beams have less energy available for wave growth, now $1/2 m_e n_b v_b \Delta v_b$ (Melrose 1985).

Spatial inhomogeneities significantly affect quasilinear relaxation. One effect is due to reabsorption (or damping) of Langmuir waves by slower electrons. Qualitatively, it arises as follows for a spatiotemporally localized pulse of electrons: faster electrons outrun slower electrons to a given location, forming a beam in $f_r(v_\parallel)$ and driving Langmuir waves at relatively high phase speeds v_ϕ, which are subsequently reabsorbed by slower late-arriving electrons (since then $\partial f/\partial v_\parallel < 0$ at $v_\parallel = v_\phi$), thereby moving energy back into the beam and reducing its energy loss from the homogeneous prediction. It was proposed that inhomogeneous effects limit quasilinear relaxation and the beam instability in Earth's foreshock for example, allowing high levels of Langmuir waves to persist with electron distributions that are only partially quasilinearly relaxed and sometimes still have beam features present (Cairns 1987b). This proposal is supported by some numerical simulations for Earth's foreshock (Klimas and Fitzenreiter 1988).

Stochastic growth theory (SGT) takes the ideas of inhomogeneities and incomplete quasilinear relaxation several steps further by assuming that a wave-particle system is very close to a state of marginal stability (averaged over time and volume) and that the wave gain $G(t) = \ln(E(t)/E_0) = \int_{-\infty}^{t} \gamma(t)$ is a stochastic variable. Here $E(t)$ is the wave electric field at time t, E_0 is a reference field, and $\gamma(t)$ is the growth rate. The stochastic nature of G then predicts, by itself, the crucial qualitative point that the waves should be intrinsically bursty. Similarly, the logarithmic dependence of G on the wave field enables SGT to explain qualitatively the production of waves with a wide range of wave fields, from quasithermal to those approaching or exceeding the thresholds for nonlinear processes. Provided that many fluctuations in γ occur during some characteristic time for the waves then the Central Limit Theorem predicts that the probability distribution of E will be lognormal (meaning that $\ln E$ is Gaussian distributed). Figure 23.10 provides strong evidence that Langmuir waves in Earth's foreshock are in a SGT state. Indeed, SGT appears to apply widely, accounting for the wave properties in over 14 applications to date (Robinson et al. 2006).

One model for how an SGT state is achieved for electron beam-driven Langmuir waves involves the beam moving through an inhomogeneous plasma which has multiple evolving sites where wave growth is favored, leading to enhanced localized growth and modification of the particle distribution inside the sites, while the beam rebuilds between growth sites due to faster electrons outrunning slow ones and increasing $\partial f_r/\partial v_\parallel$ (Robinson et al. 1993; Cairns and Robinson 1997). Indicative calculations suggest that the model is viable for Earth's foreshock (Cairns and Robinson 1997) but have not yet been performed for other foreshock sources.

As well as providing an explanation of the bursty nature of the Langmuir waves, SGT provides a ratio-

nale for assuming that the waves are near marginal stability (suitably averaged over time and space) and for making a quantitative prediction for the amount of energy entering the Langmuir waves irrespective of the details of the wave growth and saturation. Specifically, the power flux entering the Langmuir waves equals the total time derivative of the free energy available from quasilinear relaxation of the electron beam, yielding in steady-state (Knock et al. 2001)

$$\frac{d}{dt}W_L = \mathbf{v}.\frac{\partial}{\partial \mathbf{r}}\left(\frac{n_b v_b \Delta v_b}{3}\right) \approx \frac{n_b v_b^2 \Delta v_b}{3l}\,. \qquad (23.13)$$

Here $W_L = \epsilon_0 E_L^2/2$ and the factor of 3 comes from multiplying the quasilinear prediction that 2/3 of the initial available kinetic energy reaches the waves with the 1/2 for the definition of kinetic energy. The derivative is now usually approximated by v_b/l, as in the rightmost form of Eq. (23.13), where $l = (R^2 + x^2)^{1/2}$ is the distance from the shock to the observer location along the trajectory for $v_\parallel = v_b$ (Knock et al. 2001).

Figure 23.26 illustrates the spatial variations in the beam quantities that enter Eq. (23.13) for a single ripple of an interplanetary shock with properties similar to the Bale et al. (1999). The beam properties furnished by the Liouville calculation of electrons reflected from the shock are subjected to quasilinear flattening, resulting in a plateau in the range $v_- \le v_\parallel \le v_+$ that connects the background thermal distribution to the accelerated electron component with no positive slope regions. Here $v_b = (v_+ + v_-)/2$, $\Delta v_b = (v_+ - v_-)/2$, and n_b is defined by conserving electron number. The combination of Eq. (23.13) and calculations like those in Fig. 23.26 predict robustly that the power inflow into Langmuir waves varies substantially with

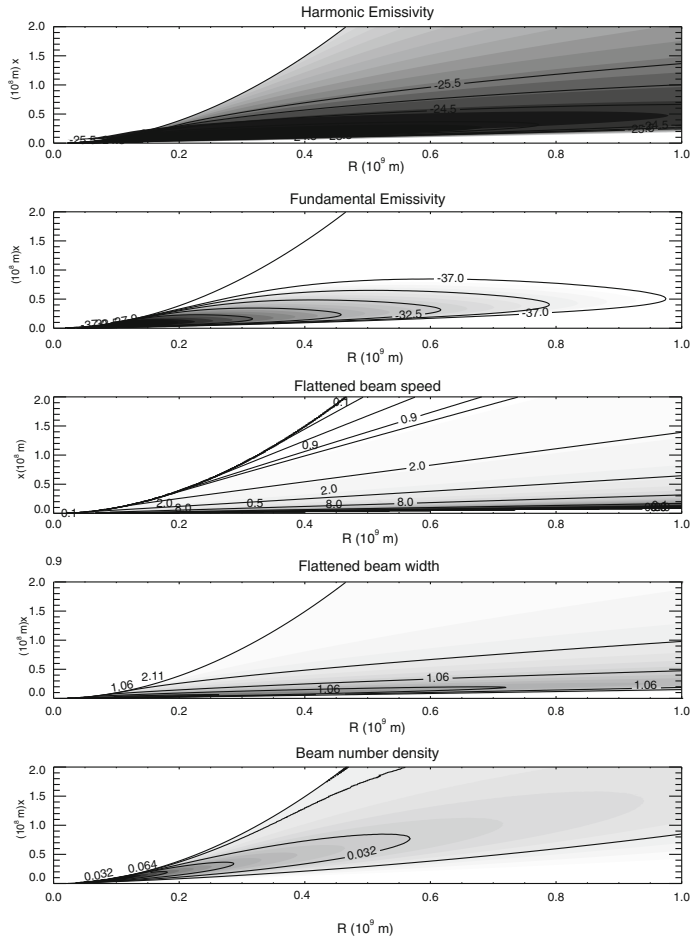

Fig. 23.26 Prediction of the quasilinearly-relaxed electron beam properties n_b/n_e, $\Delta v_b/v_b$, and v_b/V_e as a function of R and x in the top three panels, similar to Fig. 23.4 of Knock et al. (2001), for a ripple on an interplanetary type II shock with properties similar to the Bale et al. (1999) event. These allow prediction of the power flux into the Langmuir waves, via Eq. (23.13), and into radio waves (bottom two panels), as $\log_{10}(j_M)$ with j_M in units of W m^{-3} via Eqs. (23.16) and (23.18)

position in the foreshock, rising from negligible values for the fastest beams (with very low n_b) very close to the foreshock boundary, to a peak for beams with moderate speed but much larger n_b, before decreasing again for the very slow but dense and relatively narrow beams in the deep foreshock.

It is pointed out that retaining the vector nature of the derivative in Eq. (23.13) leads to spatial gradients with respect to both R and x individually, rather than just l, and that these gradients can compete and change sign (Kuncic et al. 2002). Specifically, Kuncic et al. (2002, 2004) found that the full derivative leads to the power flux being negative in regions where $v_b \lesssim 3V_e$ and the gradient in the available free energy with respect to x becomes negative as the shock become less efficient in producing accelerated electrons. That is, while wave growth still occurs for $v_b \leq 3V_e$ due to SGT effects, the net effect is of damping in the deep foreshock. More complete evaluation of these effects is needed.

It is possible to predict the average Langmuir field $\langle E_L(\mathbf{r}) \rangle$ as a function of position using Eq. (23.13) as a starting point and using the standard wave growth equation

$$\frac{d}{dt} W_L = \alpha - \gamma W_L \,, \tag{23.14}$$

where α is the energy input from spontaneous emission and other effects not dependent on W_L, and γ is the net damping rate. Combining this equation and Eq. (23.13) yields

$$\alpha_{spon} + \Lambda_{beam} = (\Gamma_L + \Gamma_{scat} + \Gamma_{ES}) \langle W_L \rangle \,. \tag{23.15}$$

Here $\langle W_L \rangle = \epsilon_0 \langle E_L \rangle^2/2$, α_{spon} is the average rate for spontaneous emission (Melrose 1985), Λ_{beam} is the average rate of power input into the beam given by the right hand side of Eq. (23.13), Γ_L is the average net Landau damping rate (set to zero because the system is near marginal stability on average), Γ_{scat} is the nonlinear rate for diffusive scattering of the Langmuir waves out of resonance with the beam due to refraction by ambient density fluctuations, and Γ_{ES} is the nonlinear rate for the electrostatic decay process $L \rightarrow L' + S$. These quantities can all be specified using analytic theory, the Liouville and reflection analysis (for Λ_{beam}), experimental quantities, and reasonable assumptions

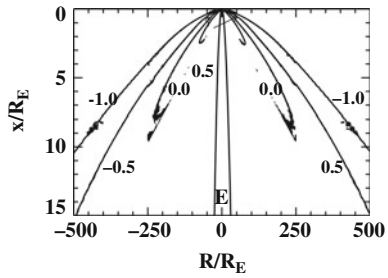

Fig. 23.27 Predictions for $\langle E_L(\mathbf{r}) \rangle$ as a function of R and x for Earth's foreshock, in contours of $\log_{10} [\langle E_L \rangle / (1\text{mV m}^{-1})]$ (Malaspina et al. 2009)

for the levels and wavenumbers of the ambient density fluctuations (Kuncic et al. 2004; Malaspina et al. 2009). Note that the nonlinear damping associated with the coalescence $L + L' \rightarrow T$ is not included in Eq. (23.15) since it is much smaller than Γ_{ES}.

Using refined expressions for Γ_{ES} and the vector approach to the convective derivative in Eqs. (23.13) and (23.14), Fig. 23.27 predicts $\langle E_L(\mathbf{r}) \rangle$ in the foreshock for a set of reasonable foreshock parameters applicable to a specific data period (Malaspina et al. 2009). The maximum $\langle E_L \rangle$ is now 10 mV m^{-1} and occurs for beams with $v_b/V_e \approx 5$–10, not right at the foreshock's upstream edge. These values are not inconsistent with observations (Anderson et al. 1981; Bale et al. 1997; Cairns et al. 1997; Bale et al. 2000; Kasaba et al. 2000; Malaspina et al. 2009) and are predicted by Kuncic et al. (2004) and Malaspina et al. (2009) to vary substantially with the solar wind parameters as the shock's reflection ability and the wave damping terms vary. It is emphasized that these predictions allow the fall-off with r to be estimated, yielding a power-law dependence $\langle E_L \rangle \propto r^p$ with index $p = -1.0 \pm 0.2$ that agrees very well with the index -1.01 ± 0.12 obtained from recent STEREO spacecraft observations (Malaspina et al. 2009).

23.5.4 Radiation Processes

The standard nonlinear processes considered to produce f_p and $2f_p$ radio emission are the following: The electrostatic (ES) decay $L \rightarrow L' + S$ to produce backscattered Langmuir waves L' and ion acoustic waves S from the beam-driven Langmuir waves L; the electromagnetic (EM) decay $L \rightarrow$

$T(f_p) + S'$ to produce radio waves T just above f_p and ion acoustic waves S', stimulated by the ES decay products S; and the coalescence $L + L' \rightarrow T(2f_p)$ of beam-driven L and backscattered L' Langmuir waves to produce radio waves just above $2f_p$(Cairns and Melrose 1985; Cairns 1988; Robinson and Cairns 1998; Li et al. 2008a, b). A general reason for favoring decay processes over coalescence processes is that decay processes require only a single population of nonthermal waves to produce nonthermal product waves, while coalescence processes require both participating populations to be nonthermal (Melrose 1985; Cairns and Melrose 1985).

The coalescence $L + L' \rightarrow T(2f_p)$ is the simplest known emission process for $2f_p$ radiation and previous analyses show that it can produce levels of emission comparable to those observed (Cairns 1988; Knock et al. 2001; Kuncic et al. 2002; Mitchell et al. 2004). It requires nonthermal levels of both L and L' waves to produce nonthermal $2f_p$ radiation (Cairns and Melrose 1985; Melrose 1985) and the ES decay is the fastest and most robust known nonlinear Langmuir process that can produce the required backscattered Langmuir waves. Specifically ES decay dominates scattering off thermal ions in almost all circumstances (Cairns 2000). (The exception is when the exponential growth time becomes smaller than the inverse of the ion sound wave frequency, a situation not expected in Earth's foreshock or realistic solar system environments; Cairns 2000.) Strong evidence also exists that ES decay proceeds for Langmuir waves in type III source regions and Earth's foreshock (Anderson et al. 1981; Cairns 1988; Cairns and Robinson 1995; Robinson and Cairns 1995; Henri et al. 2009), and it is directly relevant that the S waves produced by ES decay can stimulate the EM decay that produces f_p radiation (Robinson et al. 1994). Finally, EM decay is faster than scattering off thermal ions (with a similar proviso expected to that above for ES decay) and is the fastest known three-wave nonlinear Langmuir process for producing f_p radiation.

Standard analytic plasma theory yields the efficiencies with which energy is converted from beam-driven Langmuir waves into the L' waves ($\phi_{L'}$), f_p radiation (ϕ_F), and $2f_p$ radiation (ϕ_H). These are then combined with the power flux into the Langmuir waves to yield the volume emissivities j_M of radiation (the power output per unit volume and solid angle) throughout the foreshock (Robinson et al. 1994; Robinson and Cairns 1998; Dulk et al. 1998; Knock et al. 2001; Mitchell et al. 2004):

$$j_M = \frac{\phi_M}{\Delta\Omega_M} \frac{m_e n_b v_b^3}{3r} \frac{\Delta v_b}{v_b} , \tag{23.16}$$

$$\phi_F = 72\sqrt{3} \frac{\gamma_{L'}}{\gamma_S} \left(\frac{V_e}{c}\right)^3 \frac{v_b}{\Delta v_b} \frac{e^{-u_c^2}}{u_c\sqrt{\pi}} \zeta_F , \tag{23.17}$$

$$\phi_H = \frac{18\sqrt{3}}{5\gamma} \sqrt{\frac{m_i}{\gamma m_e}} \frac{v_b^2 V_e^3}{c^5} \frac{v_b}{\Delta v_b} \zeta_H . \tag{23.18}$$

Here $M = F$ or H, $\Delta\Omega_F = 2\pi$, $\Delta\Omega_H = 4\pi$, and the radiation is produced into bandwidths $\Delta f_F = 3(V_e/v_b)^2(\Delta v_b/v_b)$ and $\Delta f_H = 12(V_e/v_b)^2(\Delta v_b/v_b)$ that are dependent on the local beam parameters. The quantities $\gamma_{L'}$ and γ_S are the damping rates for the L' and S waves, respectively, $\gamma = 1 + \eta T_i/T_e$ is specified by Cairns (2000) as

$$\eta = \frac{T_e}{2T_i} \left(\sqrt{1 + \frac{12T_i}{T_e}} - 1 \right) \tag{23.19}$$

and relates to the phase speed of ion acoustic waves, T_e and T_i are the electron and ion (proton) temperatures, and m_e and m_i are the electron and ion masses, respectively. The quantities ζ_F and ζ_H are the overlap fractions of Langmuir waves that are able to contribute to fundamental and harmonic emission, respectively, and are defined by (Robinson et al. 1994; Dulk et al. 2008) as

$$\zeta_F = \exp - \left[\frac{4\gamma m_e}{45 m_i} \left(\frac{v_b}{\beta \Delta v_b} \right)^2 \left(\frac{3}{2} \sqrt{\frac{m_i}{\gamma m_e}} - \frac{v_b}{V_e} \right)^2 \right] \tag{23.20}$$

$$\zeta_H = \frac{c}{2v_b} \sqrt{\frac{\pi}{6}} \frac{\beta \Delta v_b}{v_b} \left[\operatorname{erf} \left(\frac{\frac{\sqrt{3}V_e}{c} + \frac{2}{3}\sqrt{\frac{\gamma m_e}{m_i}}}{\frac{V_e}{c}\frac{\sqrt{2}\beta\Delta v_b}{v_b}} \right) + \operatorname{erf} \left(\frac{\frac{\sqrt{3}V_e}{c} - \frac{2}{3}\sqrt{\frac{\gamma m_e}{m_i}}}{\frac{V_e}{c}\frac{\sqrt{2}\beta\Delta v_b}{v_b}} \right) \right] . \tag{23.21}$$

Fundamental radiation is produced very close to the local f_p and so is strongly scattered and diffused by density irregularities in the source. It is also subject to loss by linear mode conversion, this time from electromagnetic radiation to Langmuir waves (most of whose

energy is subsequently damped and not re-emitted as radiation). The expressions involving u_c in Eq. (23.17) are the escape factor for fundamental radiation (Robinson and Cairns 1998), with the value $u_c \approx 2$ found to be typical.

The flux density of radiation into the mode M is given by integrating Eqs. (23.17) and (23.18) over the source and accounting for propagation of the radiation from the source to the observer at $\mathbf{r}_0$:

$$F_M(f,t,\mathbf{r}_o) = \Sigma_{t'} \frac{\Delta\Omega_M}{\Delta f} \int d^3\, V \frac{j_M(f,\mathbf{r},t')}{|\mathbf{r}-\mathbf{r}_o|^2}\,, \tag{23.22}$$

where

$$t = t' + \int d\tau / v_g(\mathbf{r}) \approx t' + |\mathbf{r}-\mathbf{r}_o|/c\,. \tag{23.23}$$

These forms slightly generalize those in Knock et al. (2001, 2003b) and Mitchell et al. (2004). Qualitatively the flux is calculated by integrating the volume emissivity over the source, taking into account the inverse distance squared fall-off of the radiation and the time required to reach the observer, and summing over all possible emission times t'. The first form in Eq. (23.23) assumes integration along the ray path for radiation with spatially-dependent group speed v_g, while the second form assumes straight-line propagation at the speed of light. Refined versions reject contributions from straight-line paths that lie through regions where the local f_p exceeds the radiation frequency f, since this radiation would be reflected and not reach the observer.

The bottom two panels of Fig. 23.26 shows j_F and j_H as functions of foreshock position for parameters appropriate to Bale et al.'s (1999) shock near 1 AU (Knock et al. 2001). Other examples are in Knock et al. (2001), Kuncic et al. (2002), Cairns et al. (2004) and Mitchell et al. (2004). Fundamental radiation is primarily produced where v_b is large, near the tangent field line, due to the strong dependences of ϕ_F, but particularly ζ_F, on v_b. Harmonic radiation is produced over a larger area, but with lower peak emissivity, for these parameters.

How efficient need the radiation processes be? Figure. 23.28 answers this question for Earth's foreshock. The peak values for ϕ_F and ϕ_H are similar and $\approx 10^{-8}$ for nominal conditions. However, ϕ_F is strongly peaked near the upstream edge of the foreshock, where fast beams are found, while ϕ_H varies slowly over a much broader volume albeit peaked near the tangent point. The sharply peaked behavior for fundamental emission is due to the rapid variations of ζ_F in Eq. (23.21) with v_b, which also varies rapidly with x near the foreshock boundary. The peak values for ϕ_F and ϕ_H depend strongly on V_e, v_b/V_e, $\Delta v_b/v_b$, and T_i/T_e and so vary appreciably within the heliosphere's many environments where shocks and associated foreshock emission are expected.

It is pointed out explicitly now that ϕ_F and ϕ_H as specified are averages over the angular spectrum, thereby not retaining the explicit angular dependences of the underlying emission processes. The EM decay, for instance, has an intrinsic dipolar directivity peaking perpendicular to $\mathbf{B}$, while the $2f_p$ coalescence has a quadrupolar directivity with peaks at 45° to $\pm\mathbf{B}$. Both dependences are included when calculating the averaged ϕ_M above. Reasons for not including these dependences are that F radiation is produced only just above f_p and so heavily scattered by density inhomogeneities in the source, while both F and H radiation are scattered in angle by density irregularities and subject to refraction by large scale density inhomogeneities along the myriad paths between source and observer (Riddle 1974; Steinberg et al. 1985; Robinson and Cairns 1998; Thejappa et al. 2007). These effects are believed to modify the intrinsic directivities significantly, most likely dominating them, with scattering tending to isotropize both the F and H radiation. This provides some justification for assuming isotropic emission at a level corresponding to the average over the angular emission rate. However, detailed descriptions of scattering and the effects of large-scale refraction are not included yet in the theory.

Other emission processes exist and were introduced in Sections 23.1 and 23.3.2: linear mode conversion (LMC), antenna radiation from Langmuir eigenstates, and direct emission by ring-beams. None of these have yet been included in the standard foreshock theory, although LMC is poised to be included. The current status of these mechanisms, including issues with extending the foreshock theory to include them, is discussed in detail in Section 23.8 below.

Initial attempts to compare the foregoing theory quantitatively with observational data are reviewed in the next two sections for type II bursts and the 2–3 kHz outer heliospheric radiation. Earth's foreshock is the arguably the optimum source for such

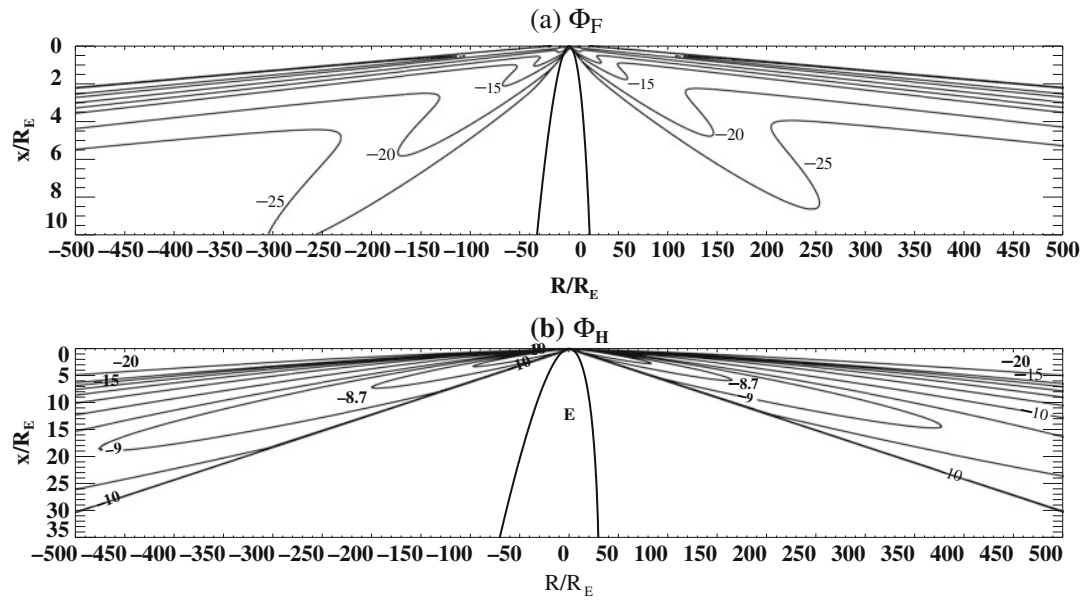

Fig. 23.28 Efficiencies ϕ_F and ϕ_H predicted by Eqs. (23.17) and (23.18) for fundamental and harmonic emission by the standard nonlinear processes, respectively, for Earth's foreshock under nominal conditions (Kuncic et al. 2004)

theory-data comparisons, due to the readier availability of radio data and the detailed plasma parameters in the source and at the shock. While comprehensive studies are still required, initial attempts are very encouraging. Kuncic et al. (2002) find that the theory predicts $2f_p$ fluxes within a factor of 2 of the Geotail spacecraft observations of Kasaba et al. (2000) for the same solar wind conditions. They also reported agreement to within a factor of 3–6 in flux with Lacombe et al. (1988) ISEE-1 observations of $2f_p$ radiation very near the upstream foreshock boundary. Finally, Kuncic et al. (2002) found agreement within a factor of 2 for the peak fluxes of $2f_p$ radiation observed by Cairns (1986b), with the observed radiation sometimes being much weaker, while the predicted flux 4×10^{-17} W m^{-2} Hz^{-1} of f_p radiation lay within the range $\approx 10^{-18} - 10^{-16}$ W m^{-2} Hz^{-1} observed.

23.6 Type II Radio Bursts

This section reviews detailed theoretical predictions for type II bursts, both interplanetary and coronal, and existing attempts to compare theory and observations. The observations and associated context are provided in Section 23.4.1 above. This section proceeds by considering the emission from an individual shock ripple (or equivalently a single, unrippled, macroscopic shock), then dynamic spectra from rippled shocks passing through purely model and then data-driven models for the corona and solar wind. Results and problems are also presented of a recent attempt to combine the type II theory with a global MHD simulation of a coronal shock. The section ends by summarizing outstanding issues and current research activities.

23.6.1 Flux Predictions for a Single Ripple or Unrippled Macroscopic Shock

The radio flux predicted by the theory in Section 23.5 depends sensitively on the shock and plasma parameters, as well as on observer location. This subsection combines Eqs. (23.10)–(23.23) to predict the radio flux at a single time from a single shock ripple, or equivalently an unrippled macroscopic shock with the same parameters, corresponding to a snapshot of the emission from a time-varying shock moving through a plasma. The background plasma is modelled simply in terms of a single electron component described as a gyrotropic kappa distribution with

$$f_\kappa(v_\parallel, v_\perp) = \frac{n_e \Gamma(\kappa+1)}{\Gamma(\kappa-1/2)} \pi^{-3/2} V_e^{-3} \left(1 + \frac{v_\parallel^2 + v_\perp^2}{V_e^2}\right)^{-(\kappa+1)}, \tag{23.24}$$

so that $f_\kappa(v) \propto v^{-2(\kappa+1)}$ for large $v^2 = v_\parallel^2 + v_\perp^2$. For Fig. 23.29 the plasma and shock parameters are appropriate to 1 AU: the paraboloidal ripple has a radius of curvature of 10^9 m at its nose, while the upstream plasma parameters are $T_e = 3T_i = 1.5 \times 10^5$ K, $n_e = 7$ cm^{-3}, $u = U = 300$ km s^{-1}, $B = 6$ nT and is oriented at an angle $\theta_{UB} = 85°$ relative to the ripple's velocity vector, and the observer is located 10^9 m upstream from the ripple's nose along its velocity vector (see the left hand image of Fig. 23.6 for more details).

Figure 23.29 shows that faster shocks are predicted to produce more intense type II bursts while sufficiently slow shocks should not produce observable radio emission (Knock et al. 2003a). This is not inconsistent with observational findings that faster (and larger) CMEs tend to produce brighter type II bursts (Cane and Stone 1984; Cane et al. 1987; Gopalswamy et al. 2001; Cairns et al. 2003). Not unexpectedly, the emission level decreases as the fraction of superthermal background solar wind electrons decreases (as the κ parameter increases from 2 to 5), since the shock-reflected electrons are initially preferentially superthermal due to Eqs. (23.7) and (23.9). Qualitatively, then, shocks moving through regions with enhanced populations of superthermal electrons (e.g., in the vicinity of CIRs or after previous flares or CMEs) are predicted to produce larger levels of radio emission for otherwise identical shock parameters. This is directly relevant to the localized emissions observed when CME shocks and CIRs interact (Reiner et al. 1998; Hoang et al. 2007; Cairns et al. 2003) and to "cannibalization" events and others in which a second CME moving through approximately the same spatial volume produces an observable radio burst whereas the first CME did not (Gopalswamy et al. 2001, 2002; Gopalswamy 2006).

The fluxes in Fig. 23.29 and similar predictions below are only observable if they exceed the background imposed by the galactic background radiation and observing instrument. The flux of the galactic background radiation varies significantly with observing frequency (Dulk et al. 2001; Hillan et al. 2010), being of order $\approx 10^{-19}$, $10^{-20.6\pm0.2}$, and $< 10^{-21.3}$ Wm^{-2}Hz^{-1} at frequencies 1–10 MHz, 300 kHz, and 100 kHz, respectively. In comparison, the Wind spacecraft's noise level is $\approx 10^{-21.4}$ Wm^{-2}Hz^{-1} in the range 100–400 kHz and $10^{-20.7}$ Wm^{-2}Hz^{-1} at 1 MHz (Dulk et al. 2001). Clearly the shock should be fast (high u and M_A) and the plasma have large numbers of superthermal electrons for the type II emission to be observable.

Figure 23.30 shows that shocks for which θ_{UB} is within $\approx 50°$ of being perpendicular are predicted to have higher levels of radio emission (Knock et al. 2003a), with quasiparallel shocks predicted to have weak emission (especially for large κ). While this has been inferred remotely for some coronal type II bursts (e.g., Stewart and Magun, 1980), detailed observational testing of this prediction for in situ type II bursts has not yet been performed. Fig-

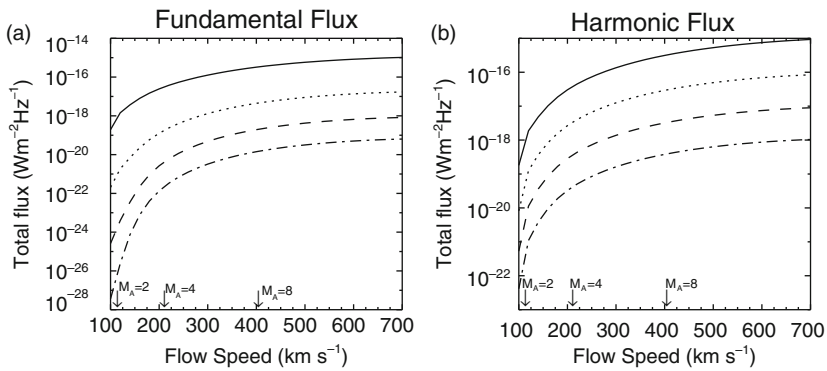

Fig. 23.29 Predicted (**a**) fundamental and (**b**) harmonic flux for a ripple on a type II shock as a function of the shock speed $U = v_{sh} - v_{sw}$ relative to the upstream plasma flow (Knock et al. 2003a). Each line is for a different κ parameter, ranging from 2 (*solid*) to 5 (*dot-dash*) as the relative fraction of nonthermal solar wind electrons decreases. The other shock and plasma parameters are listed in the text

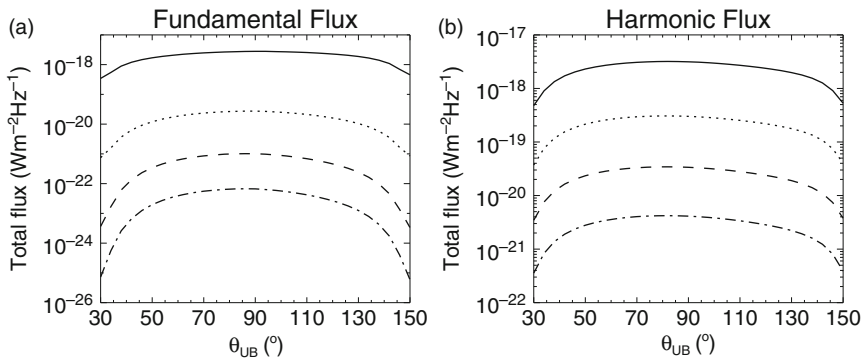

Fig. 23.30 Predicted (**a**) fundamental and (**b**) harmonic flux for a ripple with $U = 300$ km s^{-1} as a function of the angle θ_{UB} between the magnetic field vector and the ripple's relative velocity vector (Knock et al. 2003a). The line styles for κ and the shock and plasma parameters are as in Fig. 23.29

ure 23.30 shows that the dependence is weak, though, for quasiperpendicular orientations of $\mathbf{B}_u$ to the shock velocity vector. The reason is that Section 23.5's theory explicitly includes the radio emission from electrons leaving the shock at all possible local values of θ_{bn}. Accordingly all the shocks considered in Figure 23.30 have a tangent point where $\theta_{bn} = 90°$: what changes with θ_{UB} is the location of the tangent point on the ripple (see Fig. 23.6) and the local shock strength there (since u and so M_A and the shock jumps decrease with increasing distance away from the shock's nose).

The facts that the type II theory includes all reflected electrons and shows no significant variations near $\theta_{UB} = 90°$ in Fig. 23.30 (consistent with the above reasoning), and the absence of two emission regions in Fig. 23.26, provide direct contrary arguments to the elegant ideas of Holman and Pesses (1983) for herringbone bursts and the ordinary type II (backbone) emission. Specifically, instead of shock drift acceleration and the associated electron beams directly producing plasma radiation with the appearance of herringbones and the type II backbone as θ_{bn} and/or θ_{UB} are varied, the calculation naturally includes all θ_{bn} and finds no significant difference in beam or emission character or emission level as θ_{bn} is varied (or θ_{UB} is varied for quasiperpendicular values). Instead, it appears that intrinsic differences are required in the shock character as θ_{bn} is varied for the Holman and Pesses model to survive. An alternative interpretation is that interactions of the type II shock with localized spatial structures (e.g., current sheets) yields enhanced time-localized electron acceleration events and associated radio emission that are observed as herringbone bursts. Both these interpretations require detailed examination.

Figure 23.31 shows that the predicted radio flux scales with $b^{-2} \propto R_c^2$, where b is the curvature of the 3-D paraboloid $X = -b(Y^2 + Z^2)$ modelling the ripple in Figure 23.6 and R_c is the shock's radius of curvature at the nose (Knock et al. 2003a). This can be understood from the combination of $j_M \propto b$ due to the $1/r^2$ dependence in Eq. (23.22) and the volume of emission varying as b^{-3} for a distant observer. Thus, larger shocks should produce more intense radio emission and, moreover, the flux scales with the surface area of the shock. This is consistent with the results of Cane and Stone (1984), Cane et al. (1987) and Gopalswamy et al. (2001) that larger (and faster) shocks are more likely to produce observable type II bursts.

Other trends exist as functions of n_e, T_e, and B_u but are relatively weak compared with those described above (Knock et al. 2003a). In summary, Figs. 23.29, 23.30, and 23.31 demonstrate that stringent conditions exist on the shock and plasma conditions for observable type II emission to be observed. Specifically, the shock should have sufficiently large u, M_A, θ_{UB}, size (small b), and numbers of nonthermal electrons (small κ) and the observer should be sufficiently close. Since the shock and plasma properties should vary significantly in the temporally- and spatially-varying corona and solar wind, type IIs should be intrinsically bursty and time-variable in the corona and solar wind.

23.6.2 Dynamic Spectra and Macroscopic Predictions

This subsection addresses the prediction of dynamic spectra for macroscopic rippled shocks moving through the corona and solar wind. This requires

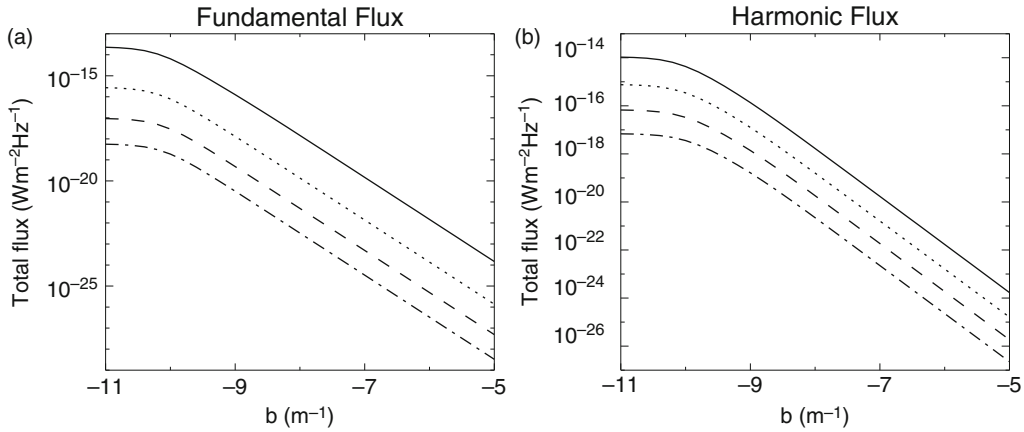

Fig. 23.31 Predicted (**a**) fundamental and (**b**) harmonic flux for a ripple with $U = 300$ km s^{-1} as a function of the curvature parameter b (Knock et al. 2003a). The *line styles* for κ and the shock and plasma parameters are as in Fig. 23.29

the calculation of radio emission for multiple ripples across the macroscopic shock, as well as modelling of the inhomogeneous corona and solar wind and the time-varying 3-D locus of the shock.

When multiple ripples are present on the shock some points in the upstream plasma can be connected to multiple ripples (for electrons with different $v_{\parallel}$, leading to multiple beams being present at these points, while other ripples may obstruct the particle paths leading to particular regions, thereby "shadowing" other ripples. These shadowing and multiple beam effects by neighboring ripples therefore directly affect the particle paths and so the electron distributions predicted upstream of macroscopic shocks (Knock et al. 2003b), in principle potentially modifying the predicted levels of Langmuir and radio waves. Importantly, calculations in Fig. 23.32(Left) show that ripples are independent to a good approximation (Knock et al. 2003b): the flux predicted for multiple realizations of the same seven 2-D ripples randomly located within a spatial interval, when multiple beam and shadowing effects are included, is within $\approx 30\%$ of that predicted assuming the ripples to be independent. Accordingly, it can be assumed that rip-

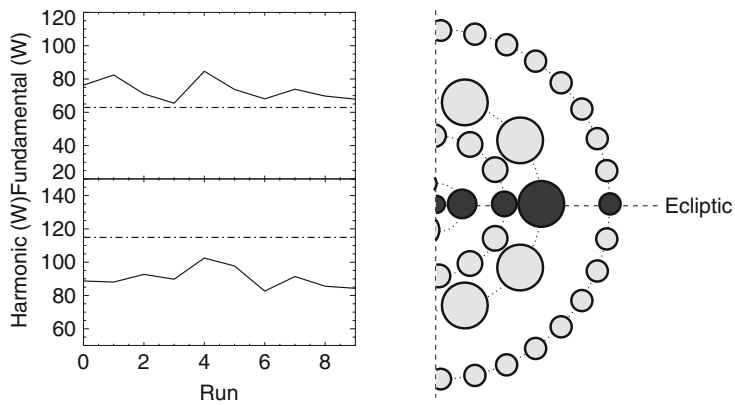

Fig. 23.32 (*Left*) Fundamental and harmonic fluxes predicted for multiple realizations of 7 randomly-located ripples, including multiple beam and shadowing effects on the electron distribution functions (*solid line*), compared with the summed flux from the same 7 ripples when calculated in isolation (*dashed line*) (Knock et al. 2003b). (*Right*) Illustration of how ripples are packed with half-hemispherical symmetry onto the macroscopic shock (Knock and Cairns 2005). See text for more details

ples are independent to within the level of accuracy currently considered necessary, greatly simplifying the calculations and length of the simulation runs. Put another way these calculations show that having multiple simultaneous ripples on the macroscopic shock for a constant density medium does not qualitatively or semiquantitatively affect the overall flux and dynamic spectrum predicted. The effects of an inhomogeneous medium on the dynamic spectrum are considered next.

Prediction of dynamic spectra for rippled shocks moving through the inhomogeneous corona and solar wind requires specification of (1) the properties of ripples considered on the macroscopic shock, (2) the time-evolving radius of curvature, 3-D location, and average velocity of the macroscopic parabolic shock, and (3) the properties of the inhomogeneous solar wind plasma. Two approaches exist to date. The first is to include ripples, use an analytic model for the macroscopic shock's velocity, and prescribe the plasma environment using an analytic or data-driven model (Knock et al. 2003b; Knock and Cairns 2005; Cairns and Knock 2006; Florens et al. 2007). The other is to ignore ripples, prescribe the shock motion and plasma environment using an MHD simulation, and develop approximate analytic formulae to predict the emission associated with the moving macroscopic shock (Schmidt and Gopalswamy 2008). Both are attractive. Most likely the optimum future approach is to include ripples but use an MHD simulation to prescribe the shock motion through an initial plasma model driven by data, thereby containing elements of both existing approaches (Cairns and Knock 2006). Since this optimum approach does not yet exist, the results of the two existing approaches are described next.

Ripples are important because they lead directly to fine structure in the dynamic spectrum, associated both with the intrinsic ripple lifetime and variations in plasma parameters across the macroscopic shock (Knock et al. 2003b; Knock and Cairns 2005; Cairns and Knock 2006), they are observed (Bale et al. 1999; Pulupa and Bale 2008), and they allow emission over the macroscopic shock to be calculated relatively efficiently. Ripples are assumed to be paraboloidal perturbations that evolve (i.e., appearing and disappearing) on a time scale $\tau_{rip} = R_c/V_A$, where R_c is the ripple's radius of curvature and V_A is the Alfven speed. This ripple lifetime provides a direct physical interpretation (with associated predictions) for the intrinsically time- and frequency-localized bursts of emission (sometimes called wisps) that make up coronal and interplanetary type II bursts. Specifically, the burst timescale should be τ_{rip} and the frequency extent $\Delta f \approx R_c f d/dr[\ln n_e(r)]$; their observed variations with f (and so r) should therefore constrain the radial profiles of $R_c(r)$, $V_A(r)$, and $n_e(r)$.

In analyses to date the ripple properties are indeed assumed to vary with r, with R_c Gaussian distributed around the decorrelation length of the magnetic field (Collier et al. 2000; Knock et al. 2003b; Knock and Cairns 2005; Neugebauer and Giacalone 2005). Computational limitations currently prevent the ripples being randomly packed onto the macroscopic shock and the contribution to the dynamic spectrum being calculated exactly. Instead, the ripples are closely packed with modified azimuthal symmetry about the Sunward direction, as shown in Fig. 23.32(Right): looking Sunward with the ecliptic plane horizontal, the eastern and western hemispheres of the macroscopic shock are packed independently and in an azimuthally symmetric fashion with ripples. The ripples are closely packed, with R_c equal to their separation distance, and their properties are chosen in the ecliptic plane. To include solar wind variability on ripple scales, the plasma density, velocity, temperatures, and magnetic field are sometimes perturbed with Gaussian-distributed fluctuations about the plasma model for the ecliptic plane. Then the radiation produced by a given ripple in the ecliptic plane is calculated, assuming no interactions with neighboring ripples. Computational limitations presently require (see Schmidt and Gopalswamy (2008), for an alternative approach) the assumption of azimuthal symmetry about the shock's average velocity vector but with different ripples in the eastern and western hemisphere. Nevertheless the falloff in the radiation flux with distance between the observer and each ripple is calculated exactly along straight line propagation paths. Moreover, if the plasma frequency along the path to the observer for a given ripple exceeds the radiation frequency, then the radiation is "blocked" and is not detected by the observer. As discussed in Section 23.5, isotropic emission patterns are assumed and neither scattering nor large-scale refraction are not included.

The analytic model developed thus far for the shock's motion, 3D locus, and properties is straightforward (Knock et al. 2003b). It assumes the macroscopic

shock to be a paraboloid about the shock's average velocity vector and can include a constant acceleration. The shock's radius of curvature can be constant or can vary with r, thereby allowing the shock to propagate ballistically or to evolve.

The inhomogeneous plasma environment is specified either (1) analytically, including the desired radial and azimuthal variations in the plasma quantities, CIRs, magnetic clouds, and other desired inhomogeneities (Knock et al. 2003b; Knock and Cairns 2005), or (2) using the data-driven model of Florens et al. (2007), itself based on an earlier model of Reiner et al. (1998) for the electron number density only. The data-driven model assumes that the solar wind is constant over a solar rotation, converts the temporal variations in plasma quantities measured by a spacecraft near Earth at 1 AU into azimuthal variations of these quantities, and then uses the monthly-averaged solar wind speed, the Parker solar wind model, and assumed power-law variations for $T_e(r)$ and $T_i(r)$ to obtain models for $n_e(r,\phi)$, $v_{sw}(r,\phi)$, $\mathbf{B}(r,\phi)$, $T_e(r,\phi)$, and $T_i(r,\phi)$ as functions of r and azimuthal angle ϕ relative to Earth's location on a given day. This data-driven model naturally has fast and slow solar wind streams and realistic solar wind structures corresponding to particular type II events. However, it has limitations, particularly related to the assumption of the Parker spiral magnetic field, which means that the macroscopic variations in the direction of **B** are not realistic. Finally, the Rankine-Hugoniot conditions are used to specify M_A, θ_{bn}, etc. over the macroscopic shock and/or each individual ripple. Note that this prescription ignores the magnetic overshoot and reformation. Both these effects are predicted to be quantitatively important at the level of factors of 2–4 (Yuan et al. 2007, 2008a, b).

Figure 23.33 demonstrates the prediction of the dynamic spectrum of a type II burst from 200 MHz to 30 kHz (right) for a model wind (left) that contains two CIRs and two magnetic clouds (Knock and Cairns 2005). The shock is moving directly towards Earth with initial shock height, speed, and acceleration of $1.1R_S$, 1,100 km s^{-1}, and -3.2 m s^{-1}, respectively. Full descriptions of the plasma model are available elsewhere (Fig. 8 in Ref. Knock and Cairns 2005), but the CIRs and magnetics cloud are apparent in maps of $T_e(r,\phi)$ (shown), $v_{sw}(r,\phi)$, $\mathbf{B}(r,\phi)$, $T_i(r,\phi)$, and $\kappa(r,\phi)$, as well as the schematic (shown). Based on Figs. 23.29 and 23.30 and analogs in. Knock et al. (2003a), one predicts theoretically that these structures and spatial variations in plasma parameters should lead directly to frequency fine structures in the dynamic spectrum. This prediction is verified in Fig. 23.33(right), which identifies the spatial structure responsible for each frequency fine structure. The figure also shows a strong burst of metric emission, followed by a substantial gap in frequency and time before interplanetary emission starts below about 2 MHz. This is associated with $V_A(r)$ peaking at a height corresponding to $f_p \approx 4$ MHz, with $M_A \lesssim 2$ for 12 MHz $\leq f_p \leq$ 10 MHz and so not expected to produce observable emission (cf. Figure 23.29).

Figure 23.33 therefore provides strong qualitative support for the interpretations that (i) variations in u/V_A due to a peak in $V_A(r)$ cause gaps between metric and decametric emission for a shock/disturbance (Mann et al. 1999; Gopalswamy et al. 2001; Mann et al. 2003), (ii) multiple lanes and even split-bands can be associated with emission from multiple regions of a shock (McLean 1967; Knock et al. 2003b; Knock and Cairns 2005), and (iii) spatial variations in the plasma and interactions with CIRs, magnetic clouds, previous CMEs, and other coronal and interplanetary structures can give rise to hotspots (or null emission regions) on the shock and cause observable fine structures in the dynamic spectrum (Reiner et al. 1998; Gopalswamy et al. 2001, 2002; Cairns et al. 2004; Knock and Cairns 2005; Cairns and Knock 2006; Florens et al. 2007; Hoang et al. 2007).

It is expected that observers at different locations will observe different dynamic spectra, due to different source-observer distances and frequency blocking for example, and different source locations on the sky. Figures 23.34 and 23.35 show radio dynamic spectra, some information on the solar wind inhomogeneities, and radio source locations (projected into the plane of the sky) for the same shock and plasma model as in Fig. 23.33 for two distinct observers (Cairns and Knock 2006). One observer is well off to the eastern side of the Earth at solar-ecliptic coordinates (100,–100,0) Gm, potentially the STEREO-B spacecraft, and the second is close to the Earth at location (148,1,0) Gm, for instance the Wind spacecraft. The source location corresponds to the direction finding information an ideal observing instrument would have available. Of course, extraction of source information on type II bursts from the dynamic spectra and direction-finding data for two or more widely separated

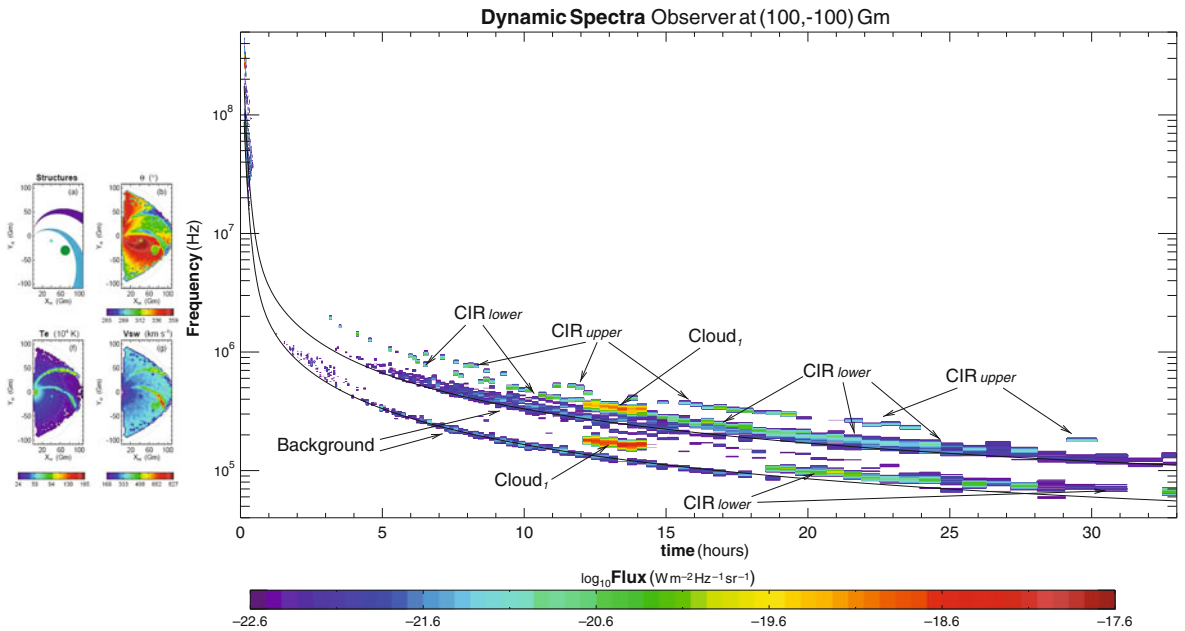

Fig. 23.33 (*Left*) Schematic and $\theta = \theta_{UB}$, T_e and v_{sw} maps of the interplanetary medium, with the Earth at $(X_H,Y_H) = (1.5,0)$ Gm and (*Right*) dynamic spectrum predicted for a shock moving through the coronal and interplanetary plasma environments summarized in (*Left*) (Knock and Cairns 2005)

observers is one major goal of NASA's STEREO mission (e.g., Bougeret et al. 2008).

Clear differences are indeed visible in the dynamic spectra (top panels) for the two observers in Figs. 23.34 and 23.35. These are due to the different relative distances between observers and elements (ripples) of the macroscopic source, as well as frequency blocking effects. Thus, the figures support the theoretical prediction that dynamic spectra observed in multiple locations indeed contain information on relative source-observer locations and the inhomogeneous plasma environment. As in Figure 23.33, some features in the dynamic spectra relate specifically to the interaction of the shock with macroscopic solar wind features. For instance, the intense (red) short-lived features at constant frequency at the times of the vertical and parabolic white lines in the top and leftmost bottom panel, respectively, correspond to the macroscopic shock crossing a magnetic cloud while the multiple long-lived curving features relate to the shock's interaction with CIRs (Reiner et al. 1998; Knock and Cairns 2005; Cairns and Knock 2006; Hoang et al. 2007).

Direction finding, however, may be required to constrain this information, as discussed next. Moreover, other physics related to scattering and directivity patterns may need to be added to better explain the detailed dynamic spectra: angular broadening and time delays due to scattering by density irregularities are likely to smooth fine structure in the dynamic spectrum, while anisotropic intrinsic directivity patterns for either radiation component would further modify the predictions for different observers.

The two rightmost bottom panels of Figs. 23.34 and 23.35 show the source location, projected onto the plane of the sky, for fundamental and harmonic radiation at the time when the macroscopic shock is crossing the first magnetic cloud (vertical and parabolic white lines in the figures' top and leftmost bottom panels). Emission from individual ripples is clearly visible. In addition, Fig. 23.34, for the western observer, shows the 3-D macroscopic source shape to be a paraboloid that is not seen exactly perpendicular to the direction of the source centroid's motion (e.g., ripples at a constant polar angle but not identical azimuthal angles do not project onto a straight line). The theory's predictions therefore suggest that direction-finding with STEREO and other spacecraft might permit the source's 3-D shape, including asymmetries, and direction of motion to be inferred remotely. If achieved

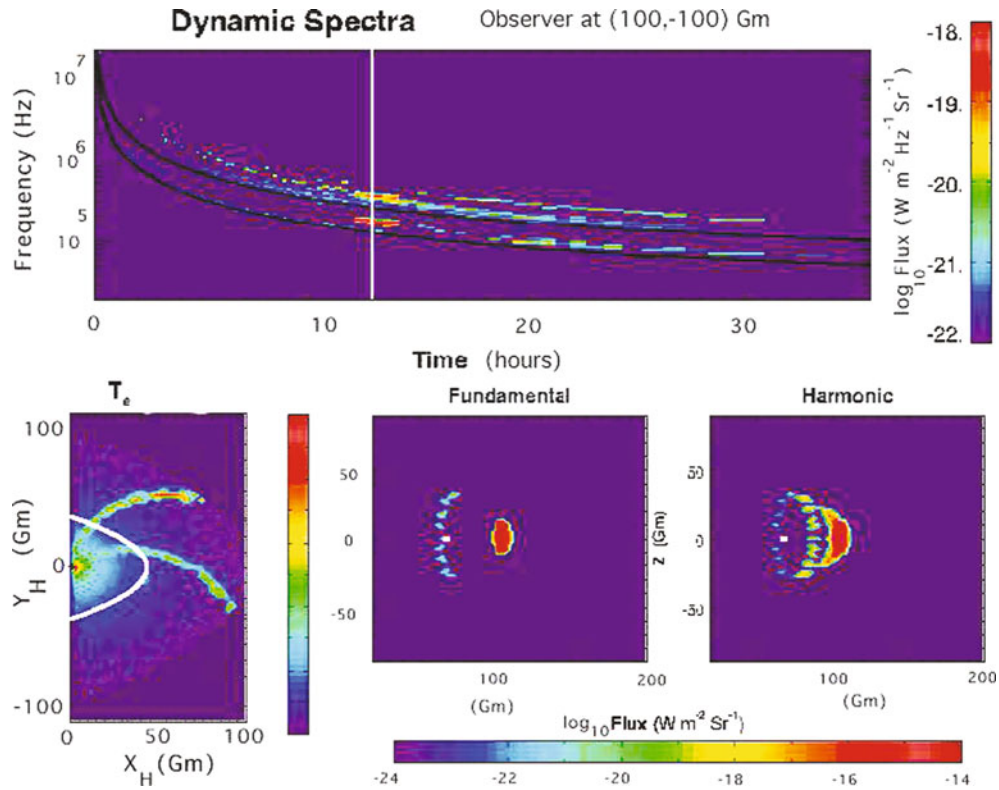

Fig. 23.34 (*Top*) Predicted dynamic spectrum, (*bottom left*) model electron temperature as a function of position in the ecliptic plane, and (*bottom center* and *right*) snapshots of the predicted source locations of fundamental and harmonic radiation, projected into the plane of the sky, for an observer at location (100,–100,0) Gm in solar-ecliptic coordinates (Cairns and Knock 2006). The snapshots are taken for the shock location and time shown by the parabolic and vertical white lines, respectively, in the leftmost and top panels

observationally, this would be extremely useful in predicting the arrival or not of space weather events at Earth.

The source seen by the head-on observer is shown in Fig. 23.35. Complementary information on the shock's 3-D structure from the eastern observer is evident. In particular, the azimuthal ripple-packing symmetries assumed in this theoretical implementation is clear. Despite the symmetry being unrealistic for a real type II shock it does elucidate the role of the macroscopic magnetic field direction: note that the western (right-side) ripples are on average much more intense than the eastern ripples, consistent with the angles between the macroscopic shock normal and Parker spiral field being closest to 90° and so with Fig. 23.30 predicting larger emission for otherwise identical ripple parameters. Put another way, the western hemisphere of the shock (on the right in Fig. 23.35) is quasiperpendicular while the eastern hemisphere is quasiparallel, so that the dominant emission is predicted from the western hemisphere. This appears to be consistent with the bias of radio-loud type IIs in the western hemisphere observed by Gopalswamy et al. (2008).

The foregoing examples have involved analytic models of the corona and solar wind. Since the plasma properties affect the predicted radio emission, it is clearly vital to realistically model the plasma environment for a given event if an accurate prediction of the dynamic spectrum is desired. The data-driven model of Florens et al. (2007), based on solar wind data for the solar rotation before the radio event, appears to be the most advanced available for all the required plasma properties. Figure 23.36 illustrates this model for the 24–26 August 1998 type II event observed by Bale et al. (1999), clearly demonstrating the complex solar wind structure for this event and the need to have

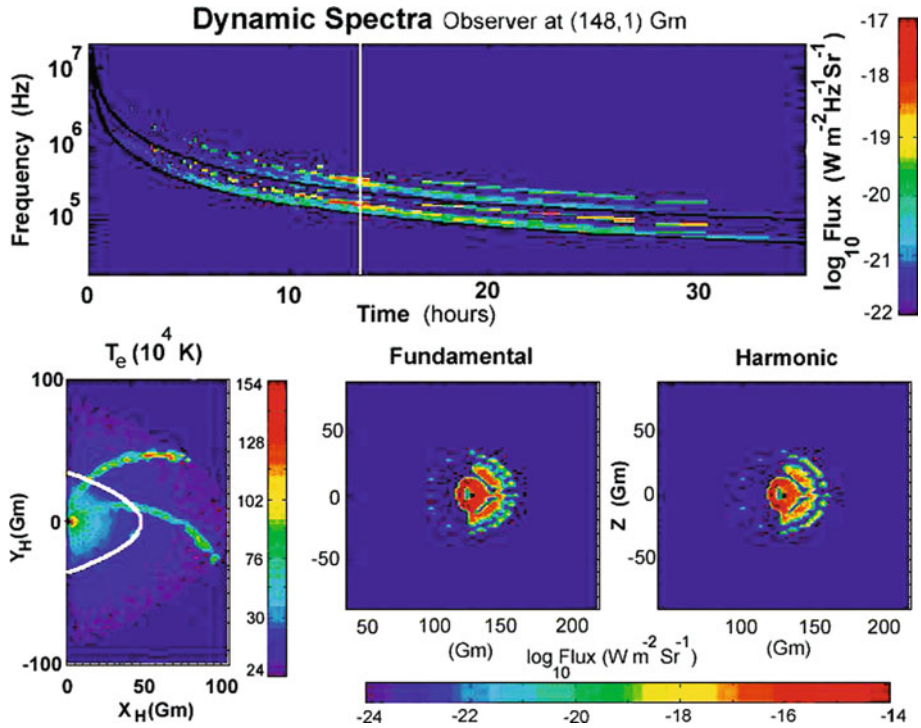

Fig. 23.35 Dynamic spectrum, electron temperature, and snapshots of the source location in Fig. 23.24's format for an observer very close to the Earth, at location (148,1,0) Gm (Cairns and Knock 2006)

event-specific solar wind (and coronal) models. It is pointed out that the more recent data-driven model of Opitz et al. (2009), uses both STEREO spacecraft to better model $n_e(r, \phi)$ and $v_{sw}(r, \phi)$ but does not predict **B**, T_e, and T_i. The Florens et al. (2007) model should be extended beyond the Opitz et al. (2009) model in due course using data from two or more spacecraft (e.g., both STEREOs and one or both of ACE and Wind), also allowing the basic assumption that the coronal sources are time-invariant to be tested.

Figure 23.37 compares the dynamic spectrum observed by the Wind spacecraft near Earth (top panel) with the following theoretical prediction: the dynamic spectrum is predicted using the foreshock type II theory for a shock with the properties identified by Bale et al. (1999) that moves through the inhomogeneous 2D solar wind plasma (Fig. 23.36) calculated using Wind spacecraft data and the Florens et al. (2007) model. Reasonable qualitative agreement with the timing and frequencies of bursts of enhanced emission is apparent: for instance the bursts near 2330, 0100, 0400, and 0600 on 24–25 August and the relatively continuous emission below $\approx$ 60 kHz after 1300 on 25 August (Florens et al. 2007). The upper panel is in dB relative to the spacecraft background while the lower panel is in absolute units, thereby complicating the task of testing quantitative agreement and requiring the spacecraft background to be accurately known for detailed comparisons. In their preliminary analysis Florens et al. (2007) find agreement typically to within a factor of 10 above 200 kHz, where the background is caused by galactic synchrotron emission (Dulk et al. 2001). They note that varying the shock direction significantly can alter the predicted flux by orders of magnitude. Nevertheless the degree of agreement found is very encouraging.

Finally, consider the novel work of Schmidt and Gopalswamy (2008), who used MHD simulations to predict the shock motion and properties through the model corona and combined these with analytic expressions based on the foreshock type II theory of Knock and collaborators (Knock et al. 2001, 2003a, b; Knock and Cairns 2005) to predict the dynamic spectrum and source locations of coronal type II bursts. Figure 23.38 illustrates the dynamic spectrum. It

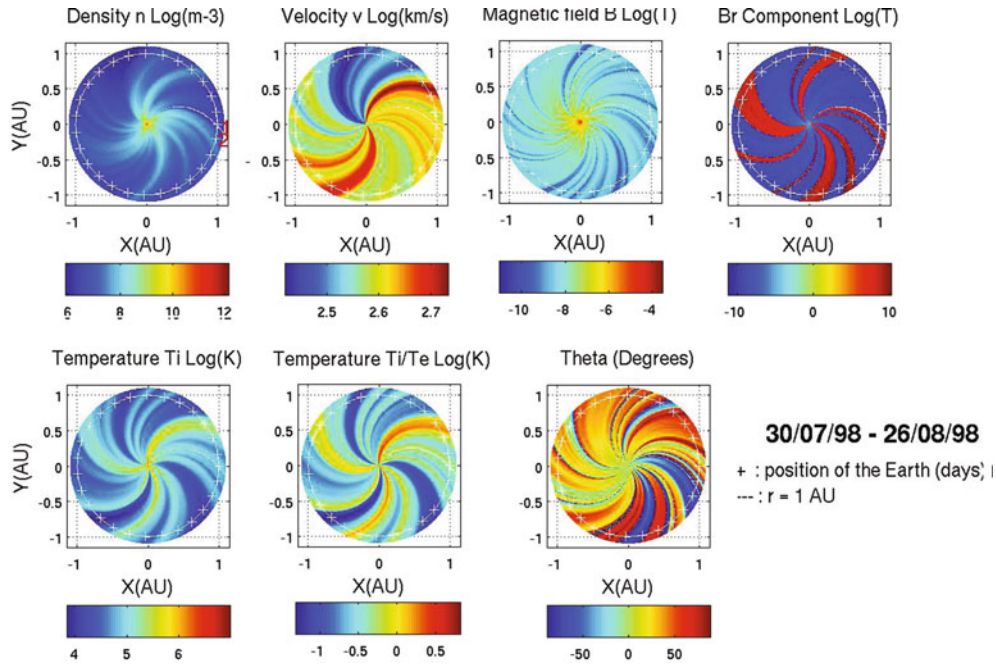

Fig. 23.36 Two-dimensional solar wind model of Florens et al. (2007) for the period 30 July to 26 August 1998 based on Wind spacecraft data (D.S. Hillan, personal communication 2010). The Sun is at $(X,Y) = (0,0)$ and the Earth at (1,0) on 30 July and then moves clockwise one plus sign per day around the white circle through the wind pattern. The *top* panels are (*left to right*) the solar wind density, speed, magnetic field strength $|\mathbf{B}|$, and inwards/outwards sense of the radial component of $\mathbf{B}$, while the *bottom* panels are the ion temperature, ratio of ion to electron temperature, and angle θ between $\mathbf{B}$ and the radial direction. Note that $\theta \approx +45°$ for the Parker solar wind model

appears attractive, with multiple emissions resulting from different areas of the shock interacting with model loops and other structures, and fluxes that correspond with the observed ranges. The problem is that the authors find that both the peak emission and the bulk of the emission are produced behind the shock (e.g., their Figs. 2, 3, and 4 and Sections 5.3, 5.6, and 5.7). This is a contradiction, since the foreshock theory can only produce electron beams and associated radio emission upstream of the shock. It is also inconsistent with all the available data for Earth's foreshock and type II bursts where we have *in situ* data, with the possible exception of the Hoang et al. (1992) interplanetary events (which are also arguably best explained in terms of remote or upstream emission – see Section 23.3.2 above).

Thus, while combining analytic approximations to the emission model with MHD simulations that model the shock motion and plasma structures is very attractive and almost certainly a viable way forward, it appears that the execution of this idea is flawed in Schmidt and Gopalswamy (2008). A necessary improvement is to require that the emission is zero downstream of shocks. It is possible that this condition was not imposed because otherwise the predicted emission was weak, plausibly because the authors assumed the plasma electrons to have a Maxwellian rather than a kappa distribution function. This severely reduces the number of fast electrons and so the levels of emission predicted in the simulation: see the strong dependence of the flux in Figs. 23.29 and 23.30 on κ, where strongly nonthermal distributions with $\kappa = 2$ and 5 yield fluxes that differ by 4 orders of magnitude (Knock et al. 2003a).

23.6.3 Outstanding Issues and Future Work

The fundamental limitation of work to date on type II bursts, both coronal and interplanetary, is the lack of detailed quantitative comparisons between observa-

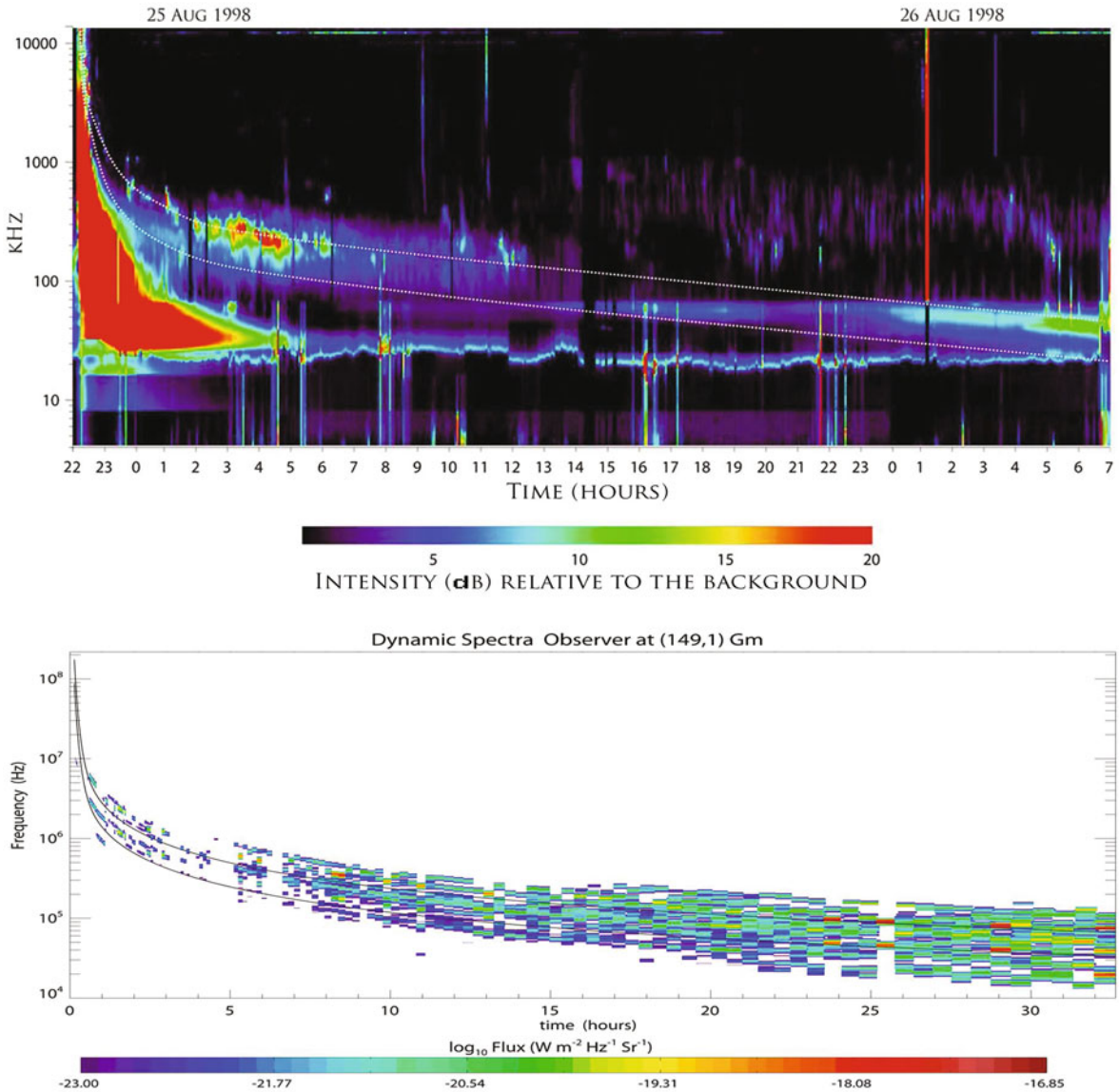

Fig. 23.37 Dynamic spectra for the 24–26 August 1998 type II burst of Bale et al. (1999): (*top*) observed and (*bottom*) predicted (Florens et al. 2007)

tions and theory for well-observed events. These can only be performed using a quantitative type II theory that uses reasonable models of the actual coronal and solar wind plasma properties, only recently available (Knock and Cairns 2005; Cairns and Knock 2006; Florens et al. 2007), the instrumental background from galactic radiation and thermal plasma waves (Dulk et al. 2001; Hillan et al. 2010), and accurate information and constraints on the shock's 3D time-varying locus (e.g., velocity, acceleration, shape, size, and expansion) from either simulations or an analytic model driven by coronal and interplanetary observations. This information is only available for a few events.

Nevertheless the time is now ripe for such detailed testing of available theories for type II bursts, especially because the direction-finding and triangulation capabilities of the two STEREO spacecraft and the

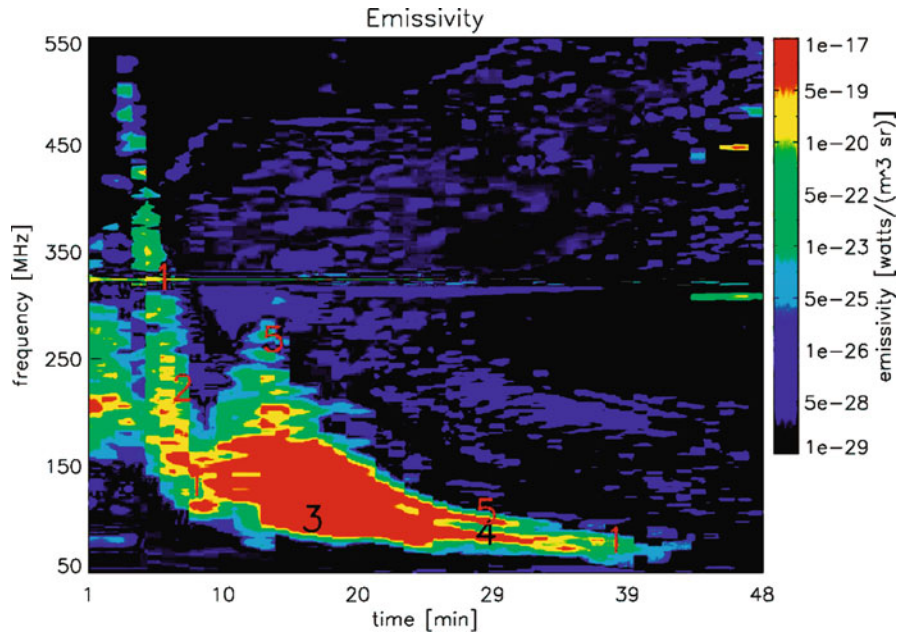

Fig. 23.38 Simulated type II burst of Schmidt and Gopalswamy (2008), using the combination of analytic approximations to the emission theory with MHD simulations of the shock motion and plasma structures. The numerical labels identify fine structures cause by the interaction of the shock with different coronal structures

Wind spacecraft (Bougeret et al. 2008) should enable the 3D location of the source and its emission hotspots to be determined better than ever before, while the coronagraph and other solar instruments on STEREO, TRACE, Solar Dynamics Observatory, and on the ground should permit CMEs, flares, and other disturbances to be characterized better than before. As a preliminary example of what is to come, Fig. 23.39 compares Wind data with the type II theory (including the data-driven solar wind model for this event) for the type II of 3 December 2004 (D.S. Hillan, personal communications, 2009, 2010). Visually there is reasonable semiquantitative agreement, with good agreement in morphology – there are two main bands, with intensifications at similar frequencies and times) – and in magnitude – observations and theory are plotted on the same intensity scale, in dB relative to the instrumental background, and typically the agreement is within 5–10 dB. Quantitatively, a cross-correlation analysis of this event yields a coefficient of order 50% with small offsets in frequency and time. Clearly detailed data-theory comparisons are still required, but efforts to date suggest that the existing theory is attractive and able to account broadly for some type II phenomena.

Once an accurate data-tested theory becomes available for type II bursts it will allow us to unlock the great potential that exists for predicting space weather events (at Earth and elsewhere in the solar system) that are driven by CMEs, their shocks, and the associated changes in magnetic field, plasma flow speed, and energetic particles based on solar and interplanetary radio data. In particular, iteratively comparing theory and data for the radio dynamic spectrum (as well coronagraph and energetic particle data) should allow extraction of the 3-D time-varying shock locus, including its velocity and acceleration, and so prediction of whether and when the shock and CME will impact Earth's magnetosphere. As an adjunct to this, robust automatic identification systems exist for type II and III bursts in coronal (metric) radio data (Lobzin et al. 2009, 2010) and could be usefully extended to STEREO and other interplanetary spacecraft datasets.

It should now be clear that the interaction of a shock with the inhomogeneous coronal and solar wind plasma is demonstrated to produce radio emission that is strongly reminiscent of coronal and interplanetary type II bursts, including the intensity and qualitative patterns of dynamic spectrum from $\approx$ 300 MHz to 10 kHz and many of the observed fine structures.

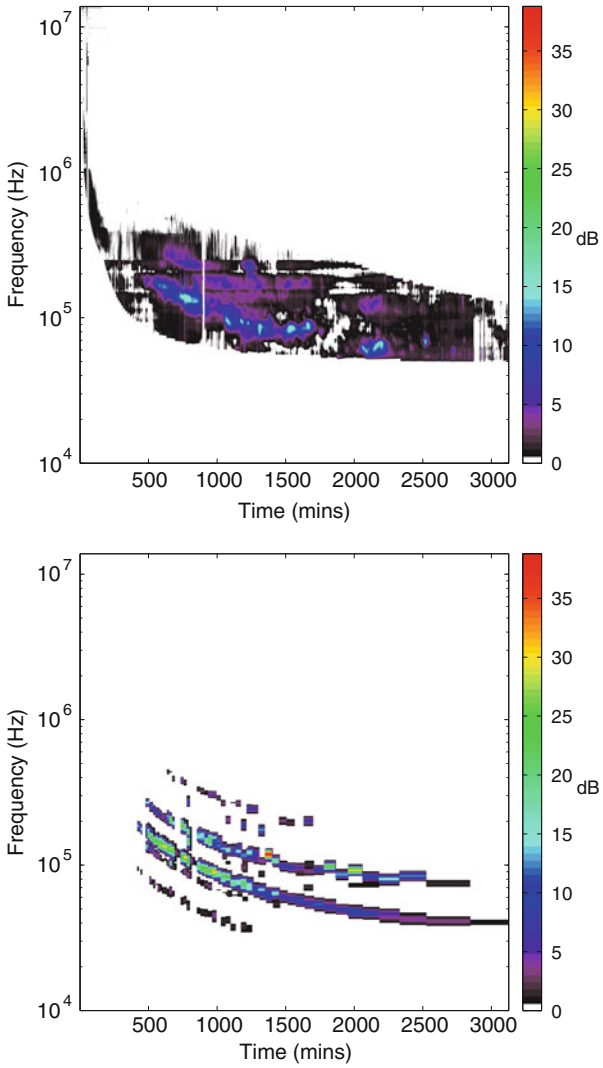

Fig. 23.39 Dynamic spectra for the interplanetary type II burst of 3 December 2004: (*above*) Wind spacecraft observations, restricted to events of interest, and (*below*) theoretical predictions based on the type II foreshock theory with the data-driven model for the solar wind (Florens et al. 2007) and shock parameters from LASCO (D.S. Hillan, personal communications, 2009, 2010)

However, equally evident is the fact that a significant number of outstanding issues exist, both in terms of theory/simulation and observations. The observational issues include the following:

- Are ripples at intermediate scales on the macroscopic shock vital to type II bursts or not, and do they cause the intrinsic blobs/burstiness/wispiness of type IIs due to their finite lifetime and spatial (frequency) extent? If not, then what causes the intrinsic blobs/burstiness/wispiness?
- Are metric type IIs all driven by blast-wave shocks, with interplanetary type IIs all produced by CME-driven shocks, or are some metric type IIs produced by CME-driven shocks and some by blast-wave shocks? At one level this is almost irrelevant for the type II theory, since all that is required is a shock wave and an upstream plasma environment that can be modelled. However, in more detail, the radio dynamic spectrum will depend on the shock's time-varying strength, velocity, and 3-D location, which all depend on whether the shock is a blast-wave (e.g., presumably weakening and slowing with time) or piston-driven (e.g., the CME provides a kinetic energy and momentum reservoir for the shock and may be accelerated outwards). Future comparisons of type II radio data with predictions based on coupling the type II theory with MHD simulations of shock evolution, cf. Schmidt and Gopalswamy (2008), may allow useful constraints to be set. These questions are also clearly important for observers and for understanding the correlations with CMEs and flares. See Section 23.4.1.2 for more discussion.
- Are herringbone fine structures caused by the shock interacting with (upstream) current sheets or other coronal structures, by special conditions for a part of the shock that are currently unknown, or are they caused by fast electrons from the flare site or CME that impulsively follow magnetic field lines (temporarily connected, for instance, by magnetic reconnection or instabilities of the CME's contact discontinuity) through the shock and into the foreshock where they produce bursts of radio emission via the type II theory? In this latter possibility the electrons would not have loss cone features in their distribution function, while in the first and third intuitively there would be much larger numbers of electrons with speeds above $c/3$ by analogy with type III bursts and their likely origin in magnetic reconnection sites. These possibilities can all be modelled quantitatively with small modifications of the existing type II theory.
- Are split-band type IIs best understood in terms of emission from two regions upstream of the shock with different f_p (and other plasma parameters), as can be explained simply and naturally by the

foreshock type II theory (McLean 1967; Knock and Cairns 2005; Cairns and Knock 2006; Florens et al. 2007) or are some actually due to simultaneous emission upstream and downstream of the shock (Smerd et al. 1974; Vrsnak et al. 2002)? Given the current absence of any theoretical justification for plasma emission downstream of the shock, the simplest test would be to ascertain whether the type II theory can predict suitable split-band-like structures for the events considered by Vrsnak et al. (2002). If so, then the upstream-downstream interpretation for type II bursts should be considered disproven unless future theoretical work provides a viable theoretical model or definitive observational evidence becomes available.

- Another interpretion for split-band type IIs involves fine structures spaced by $f_{ce}/2$ and f_{ce} for the fundamental and harmonic bands, respectively, based on observations of such splitting in f_p radiation produced in Earth's foreshock (Cairns 1994). Given that the observations in Earth's foreshock sometimes show 3 or more regularly-spaced bands in f_p radiation (Cairns 1994), coronal type II data should be examined for evidence of 3 or more bands in split-band events. In addition, the profile $B(r)$ obtained from fitting the observed bands should be compared with magnetic profiles obtained from photospheric measurements and associated modeling.
- Observations of slow-drift type II-like features composed of fast-drift bursts (Cane and Erickson 2005; Mel'nik et al. 2004) and type III bursts whose intensity changes as their electrons cross type II shocks (MacDowall 1989) need to be compared with theoretical predictions (Li et al. 2010) for type III electrons encountering localized temperature increases behind shock waves. It needs to be established whether the qualitative variations in intensity with frequency are consistent between theory and observations. If not, then alternative explanations for intensification of weak type III bursts near shocks need to be developed.
- Are the Langmuir waves in type II foreshocks well described by SGT, is Eq. (23.13) a good approximation, and what proportion of Langmuir energy with fields above the ES decay threshold is found in ordinary wavepackets versus the Langmuir eigenstates (Ergun et al. 2008) sometimes called Intense Localized Structures or ILSs (Nulsen et al. 2007)?

Significant theoretical issues exist and should be examined; many can be considered minor extensions and generalizations of the basic foreshock model for type II bursts described above. They relate to the fundamental question that started this subsection, as to whether the type II theory can go beyond its qualitative and even semiquantitative successes and actually quantitatively explain the observations. Issues with the basic theory include the following, the first three involving microphysics and the next three shock ripples and intermediate scale physics (issues with data-driven models for the solar wind and corona are discussed separately):

- The current theory calculates the electron reflection and acceleration under the assumption that the shock's magnetic mirror and potential jump are specified by the Rankine-Hugoniot predictions, thereby ignoring both the existence of significant overshoots in B and ϕ_{cs} and the effects of shock reformation (which also appears to increase the maximum values of B and ϕ_{cs}). Test-particle calculations suggest that inclusion of these effects will increase the energy flux into the foreshock electron beams and radio emissions by factors of 2–4 (Yuan et al. 2007, 2008a, b).
- Theoretical calculations of the evolution of electron beam - Langmuir wave systems with inhomogeneous plasma backgrounds should study the evolution to an SGT state, the fraction of Langmuir energy found in Langmuir eigenstates (ILS), and quantitatively justify the use of Eq. (23.13).
- Other emission mechanisms should be considered quantitatively and included in the theory, including linear mode conversion, emission from Langmuir eigenstates, direct linear processes, and frequency fine structures near $f_{ce}/2$ and f_{ce}. These options are discussed in detail in Section 23.8.1 below.
- The current numerical implementation of the theory packs ripples on the macroscopic shock assuming azimuthal symmetry about the shock's velocity vector within each of the eastern and western hemispheres, with the ripple parameters determined in the ecliptic plane. The azimuthal symmetry then means that ripples out of the ecliptic plane have parameters different than would be predicted directly from the current 2-D (cylindrical) data-driven solar wind model. Removing this symmetry would make the predictions more consistent

with the 2-D solar wind model currently used and eventually allow a 3-D solar wind model to be used.

- Detailed studies of shock ripples on intermediate scales should be performed to test how ripples develop and whether the decorrelation length of the magnetic field is the most appropriate predictor for the ripple scale, extending initial studies (Neugebauer and Giacalone 2005). While the current model is intuitive and attractive, more complete theoretical justifications should be sought. In addition, at present shock ripples are evolved statistically, not deterministically, representing another approximation.
- For a rippled curved shock electrons reflected by one ripple may be able to move upstream and cross another region of the shock, thereby potentially entering the downstream region and even producing Langmuir waves and radio emission downstream. This process has not been investigated theoretically yet. Difficulties anticipated include scattering by the downstream magnetic turbulence and the reduced contrast of the beam electrons compared with the heated downstream electron distribution. Overall this option appears unattractive due to the lack of evidence for downstream Langmuir waves and radio emission at Earth's foreshock or, especially, interplanetary type II bursts (Bale et al. 1999; Pulupa and Bale 2008).
- The effects of intrinsic directivity patterns and scattering of radiation by density irregularities, and refraction by large-scale variations in plasma density, can reduce the observed flux significantly and need consideration. This is discussed further in Section 23.5.4.
- Accurate mixed analytic-numerical implementations should be developed for the type II theory that can be "bolted-on" to global MHD (and other) simulations of the corona and solar wind. The work of Schmidt and Gopalswamy (2008) is an important first step in this direction that needs to be corrected and extended (see Section 23.6.2 for details). Such future implementations will likely need to include nonthermal particle distributions, ripple physics, intermediate scale turbulence, and the basic type II foreshock theory. The global simulation code will need to be initialized with coronal and solar wind structures provided by data-driven models like that of Florens et al. (2007).

Data-driven models for the corona and solar wind are of primary importance and need further development. While currently essentially state of the art, the model of Florens et al. (2007) needs to be extended along the following lines.

- The magnetic field remains Parker-like in the wind model and type II theory, despite observations (e.g., Fig. 23.36) often showing this to be a poor approximation to **B** and despite the type II predictions depending significantly on the angle between **B** and the shock ripple's normal (see Fig. 23.30) (Knock et al. 2003a; Knock and Cairns 2005). More realistic data-driven modelling of **B** is thus important, for instance by modelling the radial and tangential components of **B** separately and so allowing non-Parker magnetic field directions across the macroscopic shock.
- Presently the average solar wind speed (over a solar rotation) is used to relate longitude and time, potentially leading to significant errors in the positions of wind structures and so in the frequency, timing, and flux of radio emission. The 2-spacecraft approach of Opitz et al. (2009) can be used to directly test the persistence of structures (in time and longitude) between spacecraft, and so to better locate structures in (r,ϕ) space.
- The assumed stationarity of the solar wind parameters over 27 days is not always reasonable. The combination of Wind and STEREO will allow three-point assessment of this assumption and the development of more accurate plasma models for the range of longitude surveyed by the STEREO spacecraft.
- Currently solar wind turbulence and other short-spatial scale variations in the solar wind parameters are smoothed in the data-driven model, yet are likely to be especially important close to the Sun because random variations in ripple parameters (e.g., due to turbulence) can modify the frequency and flux of bursts by factors of at least two (Knock and Cairns 2005). Turbulence in the important wind parameters on intermediate and macroscopic scales could be identified observationally using the 2- or 3-spacecraft approach of Opitz et al. (2009), and then used to better model turbulence and plasma inhomogeneities in the theory.
- Last but not least, coronal parameters are necessary to make better predictions above 10 MHz, espe-

cially to understand the herringbone and other fine structures on type II bursts and to evolve our understanding of type II bursts towards predictive capability for (i) the corona's plasma environment and structures and (ii) the properties and motion of coronal shocks.

At first sight the lists of substantial issues above may appear daunting. However, they actually represent great progress over the last 20 years since they are almost all detailed questions that had to wait until a broadly viable quantitative theory for type II bursts was developed.

23.7 Outer Heliospheric Emissions

As reviewed in Section 23.4.3, the Voyager spacecraft have observed episodic bursts of radio emissions at 2–3 kHz in association with global merged interaction regions (GMIRs) reaching the vicinity of the heliopause. This section reviews the existing "GMIR/Priming" theory for the emissions, including comparisons with the observations. Earlier theories involving emission from the foreshock Sunwards of the termination shock (Macek et al. 1991; Cairns et al. 1992) or the inner heliosheath are reviewed elsewhere (Cairns and Zank 2001).

The GMIR/Priming theory combines Gurnett et al.'s (1993) GMIR model for the radiation events with the theory reviewed in Sections 23.5 and 23.6 for radio emission upstream of a shock and a theory for priming the outer heliosheath for subsequent triggering of a radiation event by the GMIR shock (Cairns and Zank 2001, 2002). The combined theory (Cairns and Zank 2002; Cairns et al. 2004; Mitchell et al. 2004) provides a quantitative theoretical basis for Gurnett et al.'s GMIR model. It involves the following primary concepts:

1. The observed radio emission is f_p radiation produced in foreshock regions upstream of a rippled GMIR shock (Cairns and Zank 2001, 2002; Cairns et al. 2004; Mitchell et al. 2004).
2. The radiation turns on (or is triggered) when the GMIR shock enters a region primed with an enhanced superthermal electron tail just beyond and near (within ≈ 50 AU of) the heliopause nose (Cairns and Zank 2001, 2002; Cairns et al. 2004; Mitchell et al. 2004).
3. The priming mechanism involves pickup ions that generate lower hybrid (LH) waves which then resonantly accelerate the electron tail by a process called lower hybrid drive (LHD) (Cairns and Zank 2001, 2002).
4. The pickup ions result from charge-exchange in the outer heliosheath of Region 3 neutrals produced originally in the solar wind (Mitchell et al. 2009) (formerly the neutrals were from the inner heliosheath (Cairns and Zank 2002)).
5. Constraints on LHD localize the priming to the outer heliosheath near the magnetic draping region (Cairns and Zank 2001, 2002; Mitchell et al. 2009).

As summarized in Section 23.4.3, the basic reason why a priming mechanism is required is that the GMIR shock does not produce observable emission in the solar wind, as evidenced by Voyager spacecraft observations when the GMIR shocks pass them and by the lack of observable radiation so far at frequencies consistent with f_p or $2f_p$ in the solar wind at distances beyond about 10 AU. Instead, the emission turns on when the GMIR shock reaches a suitably primed region beyond the heliopause. Questions that must be resolved by the GMIR/Priming theory include why and where does the radiation turn on, why does the GMIR shock not produce detectable radiation in the solar wind and inner heliosheath, and what region primed to emit radiation, and what is the priming mechanism?

Recently the IBEX spacecraft observed a ribbon of energetic neutral atoms (ENAs) that snakes across the sky between the locations of the two Voyager spacecraft and encloses (but off-center) the direction to the nose of the heliopause (McComas et al. 2009). One interpretation of this ribbon is that the ENAs result from pickup ions in the outer heliosheath (with energies of characteristic solar wind-VLISM interactions) and that the ribbon's location determines the direction of **B** in the outer helioseath (McComas et al. 2009; Heerikhuisen et al. 2010). These data and interpretation provide an independent line of evidence for pickup ions in the outer heliosheath, supporting previous strong theoretical arguments (e.g., review by Zank 1999, and references therein).

This section proceeds by reviewing the priming mechanism and the predictions for the radio flux and dynamic spectrum, before summarizing recent work

on the strength and direction of the VLISM magnetic field (associated with the priming mechanism and the observed source locations). Outstanding observational and theoretical issues are then identified.

23.7.1 The Priming Mechanism

The priming mechanism is a result of charge-exchange interactions in the outer heliosheath between protons from the VLISM (Very Local Interstellar Medium) and neutral hydrogen atoms ("neutrals") coming from either the inner heliosheath (Cairns and Zank 2001, 2002) or the solar wind (Mitchell et al. 2009), sometimes called Region 3 and 2 neutrals (Zank 1999), respectively. These two sets of neutrals both result from charge-exchange of VLISM neutrals but involve protons from regions with very different properties (Zank 1999; Izmodenov et al. 2004): either cool protons ($T \approx 10^4$ K) with large bulk speed $\approx$ 400–800 km s^{-1} from the undisturbed solar wind or else hot protons ($T \approx 10^5 - 10^6$ K) with relatively small bulk speeds $\approx$ 100 km s^{-1} from the inner heliosheath (due to the termination shock). The importance here of charge-exchange is that it changes the distribution function (and momentum) of the plasma's protons, potentially leading to the generation of waves, and the acceleration and heating of particles, as explained next.

Charge-exchange involves an electron instantaneously moving from a hydrogen atom to a proton, ideally with no change in velocity of the proton or atom, i.e.,

$$H(\mathbf{v}_n) + p^+(\mathbf{v}_p) \rightarrow p^+(\mathbf{v}_n) + H(\mathbf{v}_p)\,. \qquad (23.25)$$

The newly charge-exchanged protons experience the plasma's convection electric field $\mathbf{E}$ and magnetic field $\mathbf{B}$ and are said to be "picked up" by the plasma, changing their previous straight-line motion into a gyromotion and developing an $\mathbf{E} \times \mathbf{B}$ plasma drift at the plasma's bulk velocity perpendicular to $\mathbf{B}$. If $\mathbf{v}_n \cdot \mathbf{B} \approx 0$ and the distribution of $\mathbf{v}_n$ is narrow then the pickup ions have a ring distribution in velocity space perpendicular to $\mathbf{B}$ with ring speed $v_r \approx v_n$. (If $|\mathbf{v}_n \cdot \mathbf{B}| \neq 0$, then the proton distribution is more properly a ring-beam distribution, but this complication is ignored below.)

The proton distribution $f_{pu}(\mathbf{v}, \mathbf{r}, t)$ obeys a Boltzmann (or Liouville) equation with source and loss terms corresponding to charge-exchange. It can be solved as an integral along particle paths that reach the observation point $\mathbf{r}$ at time t, including the $\mathbf{E} \times \mathbf{B}$ drift, magnetic mirroring, draping of $\mathbf{B}$ across the heliopause surface, and propagation along $\pm\mathbf{B}$ (Zank 1999; Mitchell et al. 2009). Figure 23.40 presents a contour plot of $f_{pu}(v_\perp, v_\parallel)$ and a reduced distribution $f_r(v_\perp) = \int dv_\parallel\, f_{pu}(v_\perp, v_\parallel)$ at a point in the outer heliosheath about 30 AU from the heliopause nose. Both the contour plot and reduced distribution show that the charge-exchanged solar wind neutrals form a clear ring-beam with $v_r \approx v_\perp \approx v_{sw} = 500$ km s^{-1} and $v_\parallel \lesssim 100$ km s^{-1}. However, neutrals from the inner heliosheath only form a broad shoulder for $v_\perp \approx$ 50–200 km s^{-1} and not a ring-beam. Thus while it is confirmed that pickup ions should produce a strong ring-beam in the outer heliosheath (Cairns and Zank 2001, 2002), contrary to earlier expectations it is the solar wind (Region 3) neutrals that form the ring-beam and not inner heliosheath (Region 2) neutrals (Mitchell

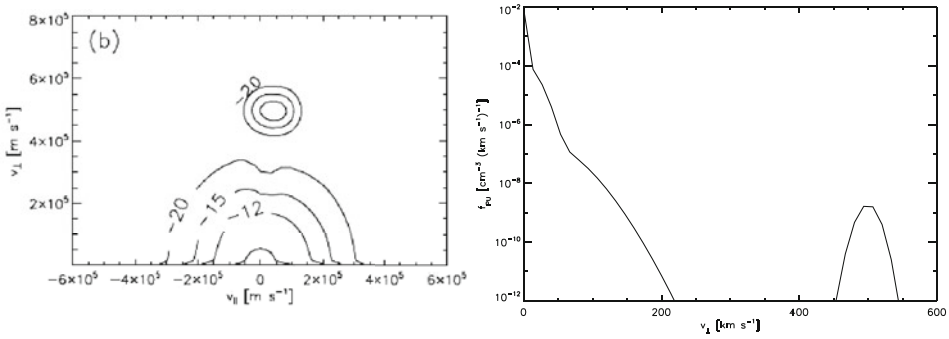

Fig. 23.40 (*Left*) Contour plot of $f_{pu}(v_\perp, v_\parallel)$ and (*Right*) the reduced distribution $f_r(v_\perp)$ for pickup protons in the outer heliosheath about 30 AU from the heliopause nose (Mitchell et al. 2009). Charge-exchanged solar wind neutrals form a clear ring-beam with $v_r \approx v_\perp \approx v_{sw} = 500$ km s^{-1} and $v_\parallel \lesssim 100$ km s^{-1} but neutrals from the inner heliosheath do not

et al. 2009). Thus, the theory proceeds as before, but with a change in the detailed source of pickup ions. This change turns out to be beneficial on balance, since although v_r is a factor ≈ 4 larger and the ring number density n_r a factor ≈ 10 lower, the kinetic energy available from the pickup ions goes up by a factor of ≈ 1.6. The full consequences of this change in the source of pickup protons have not yet been explored.

The reason that pickup ions are important in this context is that when the ring is sufficiently narrow and slow in velocity space and the plasma β (equal to the ratio of the thermal pressure to the magnetic pressure) is sufficiently low, then the ring is unstable to the growth of LH waves which can then accelerate electrons and heat the pickup ions via a process sometimes called lower-hybrid drive (LHD) (McBride et al. 1972; Omelchenko et al. 1989; Cairns and Zank 2002). LH waves have low frequencies $f \approx f_{LH} \approx (f_{ce} f_{ci})^{1/2}$), are primarily electrostatic, and propagate almost perpendicular to $\mathbf{B}$ with $k_\perp/k_\parallel \approx (m_i/m_e)^{1/2}$. Their phase fronts then move very fast along $\mathbf{B}$, and the associated parallel electric fields can accelerate electrons to large speeds via the Cherenkov resonance. Ring distributions can effectively drive LH waves that resonate with both the ion and electron distributions, with $\omega \approx \omega_{LH} \approx k_\perp v_r \approx k_\parallel v_{\parallel,e}$. Under these conditions the LH waves accelerate a plateau-like superthermal tail out of the thermal electron distribution (McBride et al. 1972; Omelchenko et al. 1989; McClements et al. 1993; Shapiro et al. 1998; Cairns and Zank 2001, 2002), with maximum speed

$$v_m = (m_i/m_e)^{1/2} v_r \, . \tag{23.26}$$

For the ring-beam in Fig. 23.40 LHD in the outer heliosheath should lead to $v_m \approx 15 V_e \approx 1.6 \times 10^7$ m s^{-1}, where $V_e \approx 10^6$ m s^{-1} is the electron thermal speed, and a total tail fraction $\approx 10^{-6}$ of the background electron number density (Mitchell et al. 2009).

Constraints on LHD localize the priming mechanism to the outer heliosheath but near the heliopause, where interstellar magnetic field lines are draped over the heliopause (Cairns and Zank 2002). (Recent suggestions that $\mathbf{B}_{VLISM}$ is closely aligned with $\mathbf{v}_{VLISM}$ mean that the heliopause nose need not be close to the draping region (Opher et al. 2009a; Pogorelov et al. 2009)). Specific reasons include: (1) Simulations show that LHD is only efficient when

$$v_r/V_A \lesssim 5 \tag{23.27}$$

(Omelchenko et al. 1989; Shapiro et al. 1998); (2) the LH waves must have minimal damping by thermal ions and electrons. Figure 23.41 shows estimates of the ratio v_r/V_A (Cairns and Zank 2002) along the Sun-heliopause nose axis, calculated assuming charge-exchange of inner heliosheath neutrals ($v_r = 100$ km s^{-1}), n_e obtained from a plasma-neutral simulation (Zank et al. 1996), and values for B calculated using the convected field approximation for $\mathbf{B}_{VLISM}$ (assumed perpendicular to $\mathbf{v}_{VLISM}$ with $B_{VLISM} = 0.15$ nT). Magnetic draping and flow stagnation at the heliopause lead to v_r/V_A decreasing from values ≈ 10 in the VLISM to values $\lesssim 5$ close to the heliopause nose, before increasing again in the solar wind. Enhanced lower hybrid damping precludes effective LHD occurring in the inner heliosheath. The reason is that $T_i \gtrsim 10^6$ K and $T_e \gtrsim 10^5$ K there, due to heating at the termination shock, whence $v_r \lesssim V_i$ and $v_m \lesssim 2V_e$ so that growth of LH waves is quenched. Thus Fig. 23.41 predicts that the LH instability and enhanced superthermal electron tail are limited to the magnetic field draping region of the outer heliosheath, presumably within $\lesssim 50$ AU of the heliopause nose.

The calculation in Fig. 23.41 is explicitly for neutrals from the inner heliosheath and not the solar wind, despite the new results in Fig. 23.40, but can be generalized by increasing v_r to suitable values. Indeed, exactly the same figure would follow for solar wind neutrals with $v_r = 400$ km s^{-1} if B_{VLISM} were

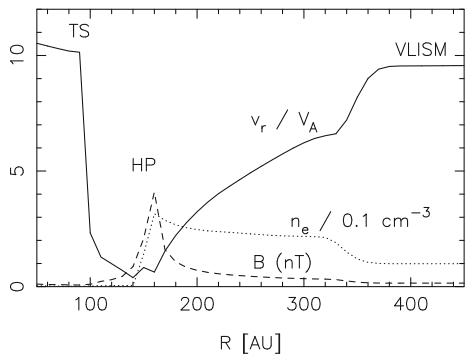

Fig. 23.41 Spatial variations of v_r/V_A, B, and n_e along the Sun-heliopause nose axis based on plasma-neutral simulations and the convected field approximation for Region 2 neutrals (Cairns and Zank 2002). The locations of the termination shock and heliopause are marked by symbols TS and HP, respectively

increased by a factor of 4 to 0.6 nT. The basic result is that Eq. (23.27) can still be satisfied for solar wind neutrals but requires higher values of B_{VLISM}. Recent global heliospheric simulations are independently coming to similar values $\gtrsim 0.4$ nT by considering where the Voyager spacecraft crossed the termination shock, the directions of the downstream flow velocities, and energetic particle observations upstream of the termination shock (Opher et al. 2009a; Pogorelov et al. 2009). Better calculations of the magnetic draping also allow such figures to be refined. An appropriate conclusion is that analogs of Fig. 23.41 imply that the GMIR-Priming theory remains viable, and able to explain the localization of the priming to the outer heliosheath near the heliopause, provided B_{VLISM} is $\gtrsim 0.4$ nT (Cairns et al. 2006; Mitchell et al. 2009; Pogorelov et al. 2009).

23.7.2 Predicted Radio Fluxes and Dynamic Spectra

Predictions for the properties of electron beams, Langmuir waves and radio waves produced upstream of the GMIR shock can now be obtained (Cairns et al. 2004; Mitchell et al. 2004, 2009) by combining Section 23.7.1's priming mechanism with the foreshock radio theory in Sections 23.5 and 23.6 for a plasma environment specified by independent global simulations of the solar wind – VLISM interaction (e.g., Zank et al. 1996; Zank 1999; Izmodenov et al. 2004; Opher et al. 2009a; Pogorelov et al. 2009). Put another way, the priming theory predicts the existence (or not) and properties of the superthermal electron tail produced by LHD that is superposed onto the background electron distribution for a given location of the shock, and the shock then reflects and accelerates the local electron distribution to form electron beams that drive Langmuir waves and radio emission. The theory presently predicts 6 quantities for a single paraboloidal ripple on the global shock at a given location: the reduced electron distribution $f_r(v_\parallel, \mathbf{r})$, gyrotropic electron distribution $f_r(v_\parallel, v_\perp, \mathbf{r})$ and volume emissivities $j_F(\mathbf{r})$ and $j_H(\mathbf{r})$ of radiation throughout the 3D foreshock, and the fundamental and harmonic radiation fluxes $F_F(\mathbf{r}_{ob})$ and $F_H(\mathbf{r}_{ob})$ at an observer location $\mathbf{r}_{ob}$, respectively. The fluxes are calculated by integrating the volume emissivities throughout the 3-D source while taking into account the $|\mathbf{r} - \mathbf{r}_{ob}|^{-2}$ falloff and straight-line propagation from each source element to the observer. Of course, the dynamic spectrum at a given location can be calculated by allowing the shock to move into regions with different $n_e(\mathbf{r})$ and analysing the time-varying frequency and flux.

Before proceeding it is stated that the calculations below are all for priming using the parameters appropriate to inner heliosheath neutrals, rather than the solar wind neutrals that should be used (Mitchell et al. 2009). These calculations therefore need to be redone for solar wind neutrals. The qualitative implications of these changes are expected to be small, but are summarized at the end of this subsection.

The background electron distribution before priming is assumed to be a generalized kappa distribution given by Eq. (23.24). Values for κ, n_e, T_e, and B are specified in Table 23.1. The axis of the ripple is assumed parallel to $\mathbf{U}$ and perpendicular to $\mathbf{B}$. The properties of the LHD tail are given by Eq. (23.26) and the ratio $n_T/n_e = 10^{-5}$ predicted assuming the pickup ions have number density $n_{ce} = 10^{-4}$ cm^{-3} appropriate to the inner heliosheath. Finally, it is relevant that $f_p = 2.6$ kHz for $n_e = 0.1$ cm^{-3}.

Table 23.1 Nominal shock and plasma parameters for the outer heliosheath

U	R_c	T_e	n_e	κ	B
600 km s^{-1}	0.42 AU	8,000 K	0.1 cm^{-3}	5	0.1 nT

The importance of priming is demonstrated first. Figure 23.42 compares $f_r(v_\parallel)$ at two foreshock locations for the following situations: shock acceleration of background electrons with no LH priming (dotted curves), LH priming but no shock acceleration (dashed curves), and both shock acceleration and LH priming (solid curves). The calculations are due to J.J. Mitchell (personal communication, 2004) and assume inner heliosheath neutrals (Cairns 2004). The foreshock locations are $(R,x) = (100,15)$ Gm and (50,3) Gm for the left and right panels, in terms of the usual foreshock coordinate system, with the latter case having larger $v_c \approx v_d R/x$. Comparing the solid and dotted curves it is evident that priming increases the number of reflected electrons by many orders of magnitude, while differences between the solid and dashed curves

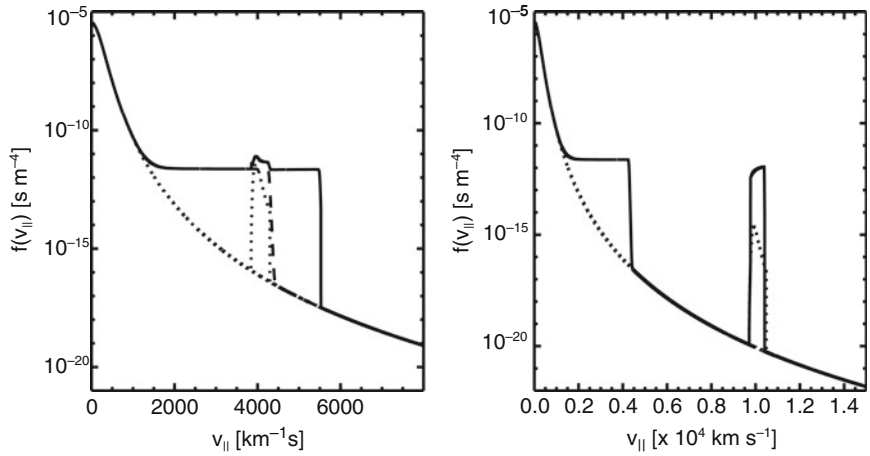

Fig. 23.42 Distributions $f(v_{||})$ predicted at two foreshock locations upstream of the GMIR shock with both LH priming and shock acceleration (*solid curves*), LH priming but no shock acceleration (*dotted curves*), and shock acceleration by no LH priming (*dashed curves*): [*left*] $(x,R) = (15,100)$ Gm and [*right*] (3,50) Gm. (Cairns 2004)

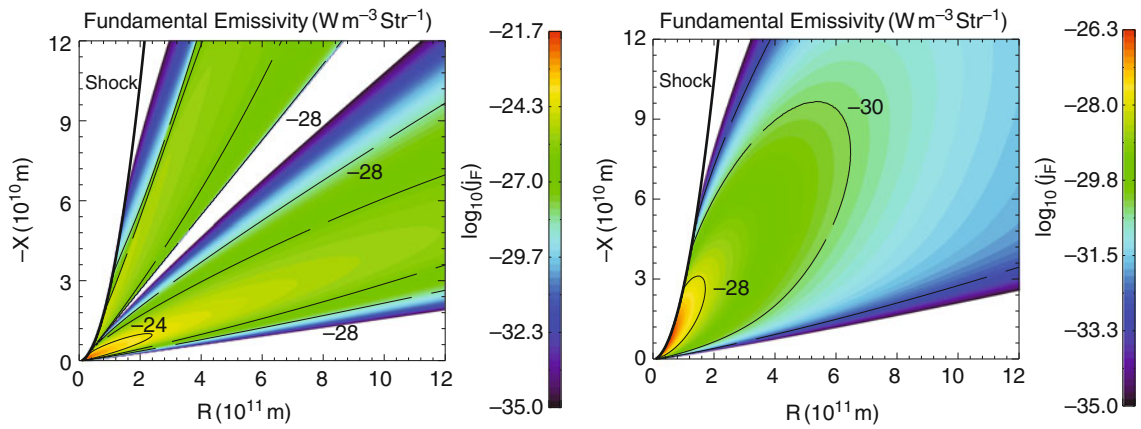

Fig. 23.43 Volume emissivity $j_F(R,x)$ for f_p radiation (*left*) with and (*right*) without LHD priming for the plasma parameters in Table 23.1 (Cairns et al. 2004). The color bar shows $\log_{10} j_F(R,x)$. The shock is solid black line and the calculation is for the plane defined by **U** and **B**

demonstrate the importance of the shock in accelerating electrons and forming beam distributions that drive Langmuir waves. Moreover, the larger number of fast seed electrons available in the primed case at large $v_{||}$ means that priming increases the relative beam number density proportionately more at the larger $v_{||}$ found closer to the foreshock boundary than at smaller $v_{||}$. Eq. (23.20) then predicts that priming will favor f_p radiation over $2f_p$ radiation (Cairns and Zank 2001, 2002), as shown below.

The importance of LH priming to the production of radiation is demonstrated in Fig. 23.43, by plotting $j_F(\mathbf{r})$ with and without LH priming for the central plane of the 3D foreshock. Priming increases the maximum values of j_F by a factor $\approx 10^4$ and causes two regions with significant j_F to develop (Cairns et al. 2004; Mitchell et al. 2004; Cairns 2004): the region with large v_b near the foreshock boundary ($x = 0$) corresponds to shock-accelerated tail electrons while the other corresponds to accelerated background electrons.

Priming is vital for $2f_p$ radiation, as shown in Fig. 23.44. However, the primary reason for Fig. 23.44 is to compare the volume emissivities of f_p and $2f_p$ radiation: the maximum value of j_H is 3–4 orders of magnitude less than for j_F, providing a very strong argument that fundamental radiation should dominate harmonic radiation by 3–4 orders of magnitude for the 2–3 kHz radiation. This conclusion follows in both the primed and unprimed cases, with the enhancement factor due to priming larger for fundamental radiation due to Eq. (23.20) and the larger number of fast electrons

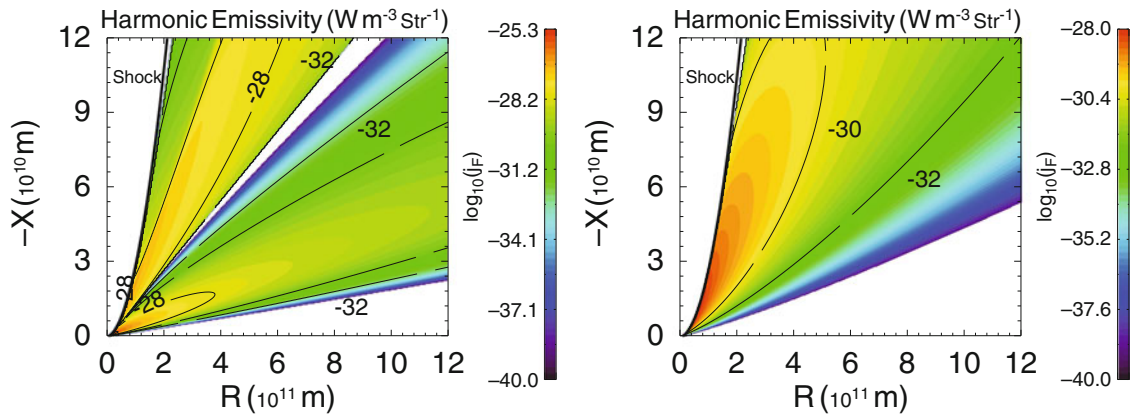

Fig. 23.44 Volume emissivity $j_H(R, x)$ for $2f_p$ radiation (*left*) with and (*right*) without LHD priming, in the same format and with the same shock and plasma parameters as Fig. 23.43 (Mitchell et al. 2004)

in the primed case. Analyses for other plasma parameters shows that the lack of $2f_p$ radiation is primarily due to the low value of $T_e = 8{,}000$ K assumed for the outer heliosheath (Mitchell et al. 2004). Thus, the theory provides a strong argument that the 2–3 kHz radiation should be exclusively f_p radiation (Cairns and Zank 2001, 2002; Cairns et al. 2004; Mitchell et al. 2004), consistent with the interpretation of the abrupt lower frequency edge of the 2 kHz component in Figure 23.21 as a cutoff at f_p for the outer heliosheath (Gurnett et al. 1993; Cairns and Zank 2002).

The fluxes predicted for a remote observer can now be calculated by integrating the predictions for $j_F(R, x)$ and $j_H(R, x)$ over the 3-D foreshock as in Eq. (23.22). The results are summarized in Table 23.2 and the important qualitative implications are: (1) The flux of f_p radiation should dominate the $2f_p$ flux by over 4 orders of magnitude. Accordingly harmonic structure is unlikely to be observed for the 2−3 kHz radiation and the observed radiation is almost certainly f_p radiation. (2) Priming is critical, since it increases the predicted flux of f_p radiation by a factor $\approx 10^4$ for these parameters. This can plausibly account for the radiation turning on beyond the heliopause once the GMIR shock enters the primed region. (3) The predicted f_p flux for this single ripple of characteristic size 1 AU is of order that observed by the Voyager spacecraft, $\approx 1.8 \times 10^{-17}$ $\mathrm{Wm^{-2}Hz^{-1}}$ (Gurnett et al. 1993), for these parameters. These results confirm the theoretical predictions of Cairns and Zank (2001, 2002).

Table 23.2 Fluxes predicted for an observer in the ecliptic plane 50 AU from the Sun along the Sun - heliopause nose axis for the shock and plasma parameters in Table 23.1

	f_p flux ($\mathrm{Wm^{-2}Hz^{-1}}$)	$2f_p$ flux ($\mathrm{Wm^{-2}Hz^{-1}}$)
Tail	3×10^{-17}	1×10^{-22}
No Tail	8×10^{-22}	7×10^{-25}

Consider now the dynamic spectrum predicted (Fig. 23.45) as the GMIR shock travels through the solar wind and inner heliosheath before entering the primed region and eventually the VLISM (Mitchell et al. 2004). The calculation assumes the spatial profiles in density, flow speed, and ion and electron temperature given by the two-shock, cylindrically-symmetric, plasma-neutral, 4-fluid (3 neutral fluids and 1 plasma fluid coupled by charge-exchange and ordinary collisions) simulation of Zank et al. (1996). For simplicity, the shock is assumed to have constant speed and shape (U and R_c are specified in Table 23.1), **U** is directed along the Sun – heliopause nose line which is the symmetry axis of the shock and system, and **B** is always perpendicular to **U**. Priming is assumed to occur in the outer heliosheath only, consistent with the theory above.

In Fig. 23.45 from early times until about day 300 the frequency bands drifting downwards from 8 kHz to about 200 Hz are f_p (primarily) and $2f_p$ radiation produced when the GMIR is in the solar wind. The

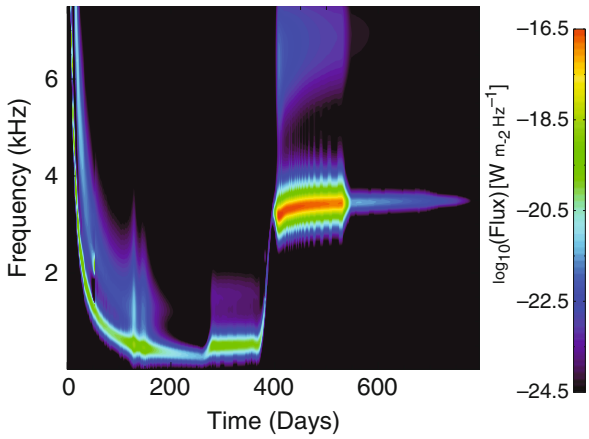

Fig. 23.45 Dynamic spectrum predicted for the GMIR shock described in the text, with the logarithm of the flux color-coded for an observer located 50 AU from the Sun and just off the Sun-heliopause nose axis (Mitchell et al. 2004). The vertical ribbing from days 400–550 is a plotting artifact

time origin corresponds to the GMIR leaving the Sun. (The enhancement near day 150 is when the GMIR passes near the observer.) The radiation produced in the solar wind is predicted to be very weak, typically well below about $10^{-18.5}$ $Wm^{-2}Hz^{-1}$, whereas the Voyager threshold is near 10^{-17} $Wm^{-2}Hz^{-1}$. The GMIR is in the inner heliosheath from about day 250 to day 400, primarily producing f_p radiation, after which the rapidly rising tone corresponds to f_p emission from the heliopause density ramp. When the GMIR enters the outer heliosheath the f_p radiation intensity is predicted to increase by ≈ 4 orders of magnitude, to values in excess of the Voyager threshold. Moreover, this emission remains almost constant in frequency and lasts for approximately 150 days, starting shortly after day 400. The GMIR enters the VLISM near day 550 and the emission then becomes very weak.

The following predictions and results follow from Fig. 23.45. First, the radiation should be too weak to be observable by the Voyager spacecraft when the GMIR is in the solar wind, the inner heliosheath, and the VLISM. Second, the radiation should turn on when the GMIR enters the primed outer heliosheath, because the radiation flux is predicted to increase above the Voyager threshold. Third, the f_p radiation predicted for the primed outer heliosheath closely resembles the 2 kHz component (compare Figs. 23.21 and 23.45). Fourth, the GMIR shock is not predicted to produce $2f_p$ radiation in the outer heliosheath or any other region that is observable above the Voyager threshold. Fifth, the timing and frequencies of the radio event predicted above the Voyager threshold are semiquantitatively consistent with the observations. (The densities, and so radiation frequencies, are slightly high in the outer heliosheath and VLISM for this simulation.)

The flux, frequency, and timing of the radio emissions are predicted to vary with the properties of the GMIR, neutral population leading to LHD, and the source plasmas (particularly the outer heliosheath plasma). Specifically the flux increases with increasing U, tail speed v_m, n_T, n_e, and R_c, and with decreasing κ (Mitchell et al. 2004), analogous to Figs. 23.29, 23.30, and 23.31 above for type II bursts. Changing the pickup ion source to solar wind neutrals from inner heliosheath neutrals is predicted to increase v_m and decrease n_T and initial calculations predict that the radio fluxes should increase by a factor ≈ 30 (Mitchell et al. 2009) (primarily due to the increased number of fast tail electrons available for the GMIR shock to accelerate), although detailed calculations remain to be done.

In summary, the combination of the priming mechanism, the foreshock emission theory, and the GMIR shock described in Fig. 23.45 provide an underlying and semiquantitative theoretical basis for Gurnett et al.'s (1993) GMIR model for the radiation (Cairns et al. 2004; Mitchell et al. 2004). Specifically, this GMIR/Priming theory can account semiquantitatively for (Cairns and Zank 2002; Cairns et al. 2004; Mitchell et al. 2004, 2009): the radiation's turn-on in the outer heliosheath; the apparent lack of emission when the GMIR is in the solar wind, inner heliosheath, and the VLISM; the lack of harmonic structure in the observed radio emissions; the characteristic flux of the observed emission; and the characteristics of the 2 kHz component. Nevertheless the theory is not complete, with several issues requiring resolution, including the lack of strong drifting emissions analogous to the observed transient emissions in Fig. 23.45, the propagation of radiation into the inner heliosphere, and a fully quantitative study of the radio flux (Cairns et al. 2004; Cairns 2004). These issues are discussed in more detail in Section 23.7.4 below.

23.7.3 Orientation and Strength of the VLISM Magnetic Field

Figure 23.24 shows that the source regions inferred for the 2–3 kHz emissions (specifically the transient emissions) lie on an approximately linear band in the plane of the sky that is almost parallel to the galactic plane and contains the direction to the heliopause nose (Kurth and Gurnett 2003). Kurth and Gurnett (2003) then interpreted the linear band in terms of the direction of the VLISM magnetic field $\mathbf{B}_{VLISM}$, with $\mathbf{B}_{VLISM}$ then being parallel to the galactic plane. This finding appears to be consistent with results for the large-scale magnetic field in the Milky Way (Frisch 2003).

Subsequently draping of the interstellar magnetic field over the heliopause was studied to see whether the priming mechanism would strongly localize the emission source near the heliopause, for instance via Eq. (23.27) and spatial variations in the Alfven speed $V_A(\mathbf{r}) \propto B(\mathbf{r})/n_e(\mathbf{r})$ (Cairns 2004; Mitchell et al. 2008). While draping does indeed lead to a linear band of enhanced B and so reduced v_r/V_A on the plane of the sky that is parallel to $\mathbf{B}_{VLISM}$, the enhancement is typically only about 10% compared with a surrounding roughly circular region (Cairns 2004; Cairns et al. 2006; Mitchell et al. 2008). Accordingly, draping alone does not appear to explain the observed band of source locations.

A very attractive idea is that the emission region is a band on the sky where $\mathbf{B} \cdot \mathbf{n} \approx 0$ where $\mathbf{n}$ is the normal vector to the GMIR shock and $\mathbf{B}$ is the magnetic field just upstream of the shock (Gurnett et al. 2006). The foreshock theory naturally incorporates this constraint since the constraint $\mathbf{B} \cdot \mathbf{n} = 0$ just identifies the location of the tangent point on the shock (e.g., Fig. 23.1) and the foreshock electrons with large values of $v_\parallel$ are connected to regions of the shock where $\mathbf{B} \cdot \mathbf{n} \approx 0$. Moreover, since each plane defined by $\mathbf{U}$ and $\mathbf{B}$ that passes through the shock has a point where $\mathbf{B} \cdot \mathbf{n} = 0$ there is a band of locations on the 3D shock where $\mathbf{B} \cdot \mathbf{n} = 0$ that is approximately perpendicular to $\mathbf{B}$ in the plane of the sky (Gurnett et al. 2006). Gurnett et al. (2006) therefore interpreted the observed band as being perpendicular to $\mathbf{B}_{VLISM}$.

The $\mathbf{B} \cdot \mathbf{n} \approx 0$ idea can actually lead to the source being elongated parallel to $\mathbf{B}_{VLISM}$ or perpendicular to $\mathbf{B}_{VLISM}$ (Mitchell et al. 2008). The reason is that the relevant question is whether the region where quasilinear relaxation of foreshock electron beams and significant emission occurs has a size parallel to $\mathbf{B}$ that is small or large compared with the size of the perpendicular domain on the shock where $\mathbf{B} \cdot \mathbf{n} = 0$ (Mitchell et al. 2008). The calculations in Figs. 23.43 and 23.44, and analogs elsewhere (Cairns et al. 2004; Mitchell et al. 2004) show that the volume emissivity of radiation is only large for distances $\lesssim 10^{11}$ m ≈ 1 AU parallel to $\mathbf{B}$. Viewed from the Sun this is a distance of about 0.4°. In comparison, the domain on the macroscopic GMIR shock where $\mathbf{B} \cdot \mathbf{n} \approx 0$ extends at least 30° from the heliopause nose (Mitchell et al. 2008). Thus, recognizing the importance of the $\mathbf{B}.\mathbf{n} \approx 0$ idea, the GMIR/Priming theory quantitatively predicts that the observed band is perpendicular to $\mathbf{B}_{VLISM}$ in the plane of the sky.

An independent means to obtain the direction of $\mathbf{B}$ in the outer heliosheath, and thence in the VLISM, is provided by the IBEX spacecraft's observations (McComas et al. 2009) of a ribbon of ENAs on the sky with energies and directions characteristic of the solar wind-VLISM interaction. In one interpretation the ribbon shows where ENAs are produced from pickup ions that have a ring distribution in the outer heliosheath and resulted from charge-exchange of solar wind neutrals, exactly as in the revised GMIR/Priming theory (Mitchell et al. 2009). Moreover, the simulations of Heerikhuisen, McComas and colleagues (McComas et al. 2009; Heerikhuisen et al. 2010) show that the ring must not be scattered into a shell if the ribbon is to be observable. In this interpretation the ring should be where $\mathbf{B}_{OS} \cdot \mathbf{r} \approx 0$ (Heerikhuisen et al. 2010), essentially identical to the $\mathbf{B} \cdot \mathbf{n}$ interpretation for the radio sources (Gurnett et al. 2006). Heerikhuisen et al. (2010) have estimated the direction of $\mathbf{B}_{OS}$ from the IBEX ENA data (it originates from close to ecliptic coordinates (224,41)), but this direction has not yet been compared with other estimates (Gurnett et al. 2006; Frisch 2003; Pogorelov et al. 2009; Opher et al. 2009a). It remains to be seen whether these are all consistent.

The IBEX data and their pickup ion interpretation also offer a way to constrain the magnitudes of B_{OS} and B_{VLISM}. This is because pickup ion rings subject to LHD and the constraint $v_r/V_A \lesssim 5$ of Eq. (23.27) are not expected to scatter into a shell but instead to fill the ring to lower $v_\perp$ (Omelchenko et al. 1989;

McClements et al. 1993; Shapiro et al. 1998; Cairns and Zank 2001, 2002), whereas pickup rings that do not satisfy Eq. (23.27) are expected to drive MHD waves and isotropize the ring into a shell distribution (see Zank 1999, and references therein). Importantly, a ring filled towards lower $v_\perp$ still satisfies the geometric constraint $\mathbf{B}_{OS} \cdot \mathbf{r}$ for the ribbon's creation, whereas a shell does not. Accordingly, the existence of the IBEX ribbon and associated ENA simulations (McComas et al. 2009; Heerikhuisen et al. 2010) provides an independent argument that the conditions for LHD, the priming mechanism, and the GMIR/Priming theory are met, whence $V_A \gtrsim v_{sw}/5$ in the outer heliosheath.

The magnitudes of B_{OS} and B_{VLISM} are thus constrained by Eq. (23.27). This leads to $B_{OS} \approx B_{VLISM} > 0.2$ nT for solar wind neutrals (Mitchell et al. 2009). (The constraint is a factor ≈ 4 weaker for inner heliosheath neutrals; Cairns 2004, Mitchell et al. 2008.) Another constraint is that the plasma beta be less than 1 for LH wave growth to be favored, yielding $B_{VLISM} > 0.03$ nT (Cairns 2004). These large values of B_{VLISM} make it likely that M_A in the VLISM is less than 1 so that an outer bow shock appears increasingly unlikely.

Recent global heliospheric simulations are independently yielding $B_{VLISM} \approx 0.4$–0.6 nT by considering where the Voyager spacecraft crossed the termination shock, the directions of the downstream flow velocities, and energetic particle observations upstream of the termination shock (Opher et al. 2009a; Pogorelov et al. 2009). These analyses should be considered more direct and stronger arguments for large values of B_{VLISM} than the arguments above based on the GMIR/Priming model. Perhaps more importantly, the large values of $B_{VLISM} > 0.4$ nT obtained by comparing the global simulations with non-radio data provide a strong argument that the constraint of Eq. (23.27) is satisfied for the outer heliosheath and so that the proposed priming mechanism and GMIR/Priming theory are viable. Another argument is provided above based on the existence and properties of the IBEX ENA ribbon.

23.7.4 Issues and Future Research Directions

The theoretical predictions for the 2–3 kHz radiation are not in as advanced a state as for type II bursts. A number of important issues exist, all of which can be resolved with further research.

The primary issue can be considered the lack of detailed quantitative predictions for the dynamic spectrum for a macroscopic GMIR shock moving through realistic asymmetric models for the inhomogenous plasma structures of the heliopause and outer heliosheath. Recent global neutral-plasma simulations show that the plasma and magnetic fields become strongly asymmetric when highly tilted and strong $\mathbf{B}_{VLISM}$ are considered (Opher et al. 2009a; Pogorelov et al. 2009). By analogy with theoretical predictions for type II bursts (McLean 1967; Knock and Cairns 2005; 2006; Florens et al. 2007), these asymmetries can be expected to produce emissions reminiscent of split-band and multiple-lane type II bursts that might explain the existence of both the 2 kHz component and transient emissions, the multiplicity of transient emissions, and fine structures in the 2 kHz component. Specifically, the hope is that some portions of the shock will encounter regions of almost constant plasma density while others will encounter regions with positive density gradients that have appropriate length scales (several to 20 AU) to yield the upwards drifting transient emissions as the shock moves up the density ramp. Slowing of the shock as it moves from the solar wind to the outer heliosheath is also expected to be vital but is yet to be included.

The next issue to do with making the theory fully quantitative is that existing calculations (Cairns et al. 2004; Mitchell et al. 2004) only consider a single ripple with $R_c = 0.42$ AU (and projected length ≈ 1 AU in the plane of the sky) whereas the macroscopic GMIR shock has a characteristic scale of over 100 AU near the heliopause, if approximately spherical, and so should have over $100^2 = 10^4$ active ripples of this size that might produce radio emission (Cairns et al. 2004). Restricting the active ripples to the region of the outer heliosheath where the plasma is primed and strong magnetic draping occurs will restrict the number of ripples over the above estimate, but not by more than an order of magnitude. Accordingly, scaling up the existing flux predictions to the macroscopic shock means that the flux may be underestimated by a factor $\approx 10^4$ (since the flux is proportional to R_c^2 and the number of ripples (Knock et al. 2003a; Cairns et al. 2004)). Since the existing calculations yield fluxes of order those observed, this is a significant quantitative problem that requires an effective loss mechanism to bring

the scaled up predictions into balance with the observations. One such mechanism is discussed next.

Propagation of the radiation into the inner heliosheath and solar wind is a major issue for the GMIR/Priming theory: the radiation is predicted to be produced near f_p upstream of a shock that is moving away from the Sun, thereby being prevented from immediately propagating Sunwards by the density increase behind the shock (Cairns and Zank 2001, 2002). This has a qualitative explanation that has not been quantified. The qualitative explanation (Cairns and Zank 2001, 2002) is that scattering by density irregularities diffuses the f_p radiation around the sides of the GMIR shock until it reaches locations where the GMIR shock has not crossed the heliopause, where the radiation frequency is now much greater than the local plasma frequency and so the radiation can propagate directly across the shock and into the inner heliosphere. Existing calculations predict that scattering should be important in the solar wind and inner heliosheath (Cairns 1995, 1996; Armstrong et al. 2000).

Quantitative ray tracing calculations are needed to calculate the fraction of the emitted radiation that can reach the inner heliosphere by diffusing around the GMIR shock. Intuitively, this fraction is expected to be much less than 1% (Cairns and Zank 2001), meaning that the majority of the radiation moves out into the VLISM; this allows and allowing the flux predictions for multiple active ripples on the GMIR shock to possibly lead to fluxes of order those observed (Cairns et al. 2004). Accordingly, radiation from GMIR-like shocks leaving the myriad active stars in the Galaxy like the Sun may well be a major contributor to the galactic background below about 100 kHz. Another point is that the apparent necessity for the radiation to leak around the sides of the GMIR shock before entering the inner heliosheath, rather than moving directly across near the nose of the shock, means that there must be a geometric "shadow zone" immediately behind the portion of the GMIR shock that has crossed the heliopause. Spacecraft inside the shadow zone will observe only weak radiation that has been scattered into the region. This shadow zone concept may explain why the radio events observed after 2002 (see Fig. 23.19) have been weaker than the earlier events despite the Voyager spacecraft being closer to the heliopause nose and so the predicted source regions.

Detailed simulations of the LHD process and the constraint of Eq. (23.27) are required for parameters relevant to the outer heliosheath, including the effects of both charge-exchange and ordinary collisions. While Eq. (23.27) is consistent with previous simulations (e.g., of Omelchenko et al. 1989; McClements et al. 1993; Shapiro et al. 1998), this constraint needs to be confirmed and to be developed as a function of β.

Solar cycle variability may also affect the likelihood of producing radio emissions and may produce density structures in the outer heliosheath relevant to transient emissions. Specifically, the 11-year solar cycle injects periodic variations in the numbers of solar wind and inner heliospheric neutrals plus density waves that propagate into the outer heliosheath (Zank and Muller 2003; Scherer and Fahr 2003). Mitchell et al. (2005) showed that there should be a solar cycle dependence on the priming, with maximum priming 2–3 years after solar maximum, and so optimum conditions to produce radio emissions. While this is consistent with the radio data, the predictions need to be redone for solar wind neutrals and the consequences explored of the density waves injected into the outer heliosheath. Qualitatively, these density structures provide natural density ramps over a restricted range of heliolatitudes and heliolongitudes for the shock to move up and produce upwards-drifting radio emissions like the transient emissions.

The strong dependence of the predicted radio emission on the shock speed is another issue that requires more careful consideration. This is relevant in at least 2 ways. The first is that shocks are predicted to slow markedly in the inner and outer heliosheaths (e.g., Gurnett et al. 1993; Zank 1999), leading theoretically to substantially lower amounts of radio emission via analogs of Fig. 23.29, but this effect has not been considered in the dynamic spectra and other quantitative calculations of the radio emission (Cairns et al. 2004; Mitchell et al. 2004). Secondly, this may explain why the 2003–2004 emission event is much weaker than the 1983–1984 and 1992–1994 events (Cairns 2004): the lower GMIR speed inferred for the 2003–2004 radiation event (≈ 560 km s^{-1}) compared with the 1983-1984 and 1992-1994 events (≈ 850 km s^{-1}) should lead to a smaller radiation intensity by a factor ≈ 2, thereby potentially moving much of the radio emission produced below the detection thresholds of the Voyager plasma wave instruments. (Note that the most

intense radio emissions observed to date have intensities only a factor ≈ 3 above the Voyager thresholds.)

Attractive future modifications to the foreshock theory were identified in Sections 23.5 and 23.6.3 in the contexts of Earth's foreshock radiation and type II bursts. Some of these apply also to the 2–3 kHz emissions. Further discussion of these is deferred to the next section.

23.8 Discussion

Detailed applications of the foreshock theory to Earth's foreshock, type II bursts (both coronal and interplanetary), and the 2–3 kHz radio emissions are shown in Sections 23.5, 23.6, and 23.7 to broadly be in good qualitative and even semiquantitative agreement with available observations. Nevertheless, these same sections identified a number of areas of improvement for the basic theory itself as well as for the detailed applications of the theory. Rather than repeat those here, this section instead focuses on issues involving the emission mechanisms for the radiation and on future applications of the theory.

23.8.1 Improvements to the Foreshock Theory

Section 23.6.3 describes a number of important revisions proposed for the foreshock theory, including the reflection of electrons at the shock (principally the inclusion of overshoots in the magnetic field and cross-shock potential), inclusion of other emission processes, the modelling of ripples on the macroscopic shock, better modeling the directivity patterns, propagation, and scattering of the radiation, and the development of "bolt-on" numerical implementations of the theory that can be combined easily with advanced numerical, data-driven models for the background plasma and evolution of the shock. Attention is focused here on emission processes other than the standard ES decay, EM decay, and $2f_p$ coalescence processes. These include linear mode conversion (LMC) (Forslund et al. 1975; Budden 1985; Yin et al. 1998; Cairns and Willes 2005; Kim et al. 2007, 2008), radiation from localized Langmuir eigenstates (Malaspina et al. 2010), direct radiation via electron cyclotron maser emission (Farrell 2001), and fine structures at $f_{ce}/2$ in f_p radiation from Earth's foreshock (Cairns 1994). These are not included in the basic foreshock theory, but are now discussed in turn.

Before starting, however, an important point is made: the current foreshock theory yields predictions in reasonable semiquantitative agreement (typically a factor of order 3–10) with available observations, implying that these other processes are not likely to be crucial unless a basic building block of the theory (like the power flux into the Langmuir waves) is not estimated accurately. Moreover, strong arguments exist for favoring the standard processes (Sections 23.3 and 23.5). Nevertheless, it is important to thoroughly explore and develop these non-standard emission processes. Reasons include the fundamental nature of the physics, the need to extend the foreshock theory so that it can quantitatively explain the observed radiation to better than a factor of 2, and the possibility that these processes will apply to other radio emissions.

Recent work has almost placed LMC in a suitable state for insertion into Eq (23.17) and consideration on an equal basis to the standard nonlinear processes. The reasons are as follows. Recent simulations (Kim et al. 2007, 2008) have established the energy and power conversion efficiencies for a specified incoming wavevector (shown to differ by the ratio of the group speeds of the electrostatic and electromagnetic waves, thereby being a quantitatively important difference) and reconciled previous analytic and simulation work in (Forslund et al. 1975; Yin et al. 1998), while analytic and numerical calculations have shown how to average the power (or energy) conversion efficiencies over the angular and length scale distributions of incoming Langmuir waves and density irregularities (Cairns and Willes 2005). The averaged efficiencies are commensurate with those for the nonlinear processes above, sometimes being larger and sometimes smaller depending on the beam parameters, and are smaller than the unaveraged efficiencies by factors of order $(V_e/c)^2$ (Cairns and Willes 2005). This provides a robust argument that LMC needs to be fully considered (Cairns and Willes 2005) – as argued previously on the less secure grounds of the unaveraged power conversion efficiencies being $\approx 50\%$ and so orders of magnetitude larger than required to explain the observed fluxes. Future work should therefore involve the addition of the averaged LMC efficiencies

into Eq. (23.17) on an equal basis to the nonlinear efficiencies.

The newly discovered Langmuir eigenstates (Ergun et al. 2008; Malaspina and Ergun 2008), sometimes called Intense Localized Structures or ILSs (Nulsen et al. 2007), have significant nonlinear currents j_{NL} and electric fields E_{NL} at both f_p and $2f_p$ that are associated with the time varying Langmuir fields at f_p and their spatial gradients. These currents can drive radio waves at f_p and $2f_p$ due to coupling between the current and wave fields leading to non-zero power input $\mathbf{j}_{NL} \cdot \mathbf{E}_{NL}$. Effectively the eigenstate radiates as an antenna. A similar mechanism was tried earlier (Papadopoulos et al. 1978; Goldman et al. 1980) for Langmuir wave packets subject to the process of wave collapse in strong turbulence, in which nonlinear self-focusing dominates wave dispersion and wavepackets intensify and collapse to spatial scales of order $10\lambda_D$ (Zakharov 1972; Robinson 1997), but found to be unimportant. The critical difference in the new calculations is that the eigenstate (or ILS) has a length scale larger than or commensurate with the wavelength of $2f_p$ radiation ($\lambda \approx c/2f_p$), so that the source cannot be assumed to be small compared with the wavelength: this results in survival of the dipole contribution to the radiated fields (Malaspina et al. 2010), unlike the antennas for collapsing wavepackets considered previously (Papadopoulos et al. 1978; Goldman et al. 1980).

Malaspina et al. (2009) calculated the $2f_p$ power radiated by an ILS (Fig. 23.46 and found it to be sufficient to contribute significantly to the radiation observed in Earth's foreshock, perhaps even dominating the standard nonlinear processes. The predicted power depends sensitively, though, on the number, characteristic fields, and length scales of the ILS in the foreshock, which are not yet known observationally or predictable theoretically. Further work is required on this antenna mechanism for ILS, which needs to be incorporated into the standard foreshock theory and its applications to solar system shocks.

Now consider cyclotron maser mechanisms for direct generation of f_p and $2f_p$ radiation (Wu et al. 1985; Farrell 2001). This requires careful tuning of parameters to obtain emission near the observed frequencies of $\approx 1.9f_p - 2.1f_p$ rather than $1.4f_p$, $2.5f_p$ or any other frequency, since $f_{ce} \ll f_p$ and the observed emission is at high harmonics

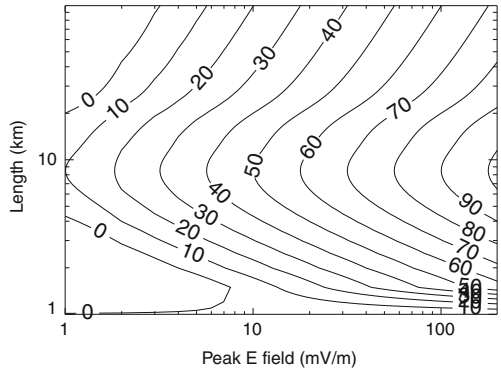

Fig. 23.46 Prediction of the $2f_p$ power in dB radiated by a Langmuir eigenstate (ILS) in Earth's foreshock as a function of the ILS peak electric field and length scale (Malaspina et al. 2010). The contour labelled 0 corresponds to a power of 2×10^{-11} W

($\approx$ 50–200) of f_{ce} in most source regions of interest in this paper (and specifically for Earth's foreshock). Furthermore, the process requires an energetic ring-beam distribution, with characteristic perpendicular speeds at least $0.1c$. While such ring-beam distributions can be produced by mirror reflection (Yuan et al. 2007, 2008a), they have very low number densities ($n_b/n_e \leq 10^{-6}$) at such large $v_\perp \approx v_\parallel$ (see Fig. 23.25 and the papers of Fitzenreiter et al. (1990) and Cairns et al. 1997). These two problems must be resolved before direct cyclotron maser emission can be considered a viable competitor to the standard nonlinear processes or the other alternative processes above.

Finally, no detailed or accepted theoretical explanation exists for splitting at $f_{ce}/2$ for f_p radiation in Earth's foreshock (Cairns 1994), which may also be relevant to split-band type II bursts and fine structures in the transient component of the 2–3 kHz outer heliospheric radiation. Mechanisms involving linear growth of oblique Langmuir waves due to loss cone or ring-beam features in the reflected electron distribution (Lobzin et al. 2005), followed by LMC or nonlinear conversion processes to radiation, or direct cyclotron maser emission may be attractive. Alternatively, magnetization effects on the standard nonlinear processes for f_p and $2f_p$ radiation need to be investigated for frequency fine structures, as opposed to the polarization analyses performed prevously.

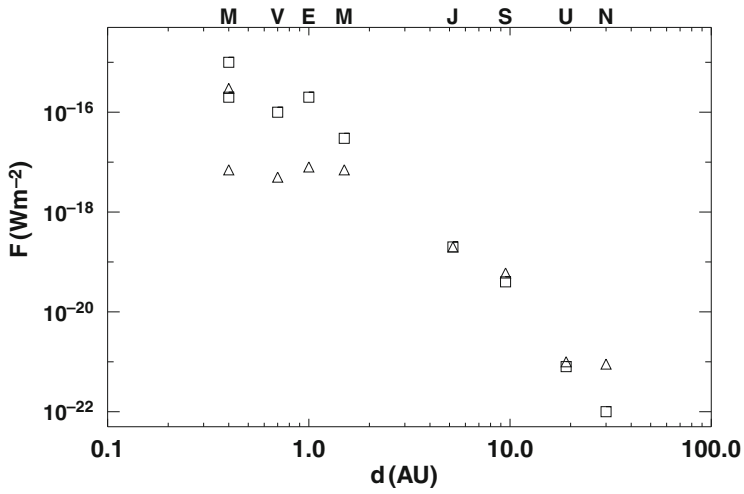

Fig. 23.47 Total fluxes (W m^{-2}) of f_p (*triangles*) and $2f_p$ (*squares*) radiation from planetary foreshocks for an observer O located a distance $2a_s$ upstream from each planet along the Sun–planet line, where a_s is the bow shock's standoff distance (Kuncic and Cairns 2005). The radio fluxes are calculated for nominal solar wind conditions, except for Mercury, where the fluxes are calculated for $\theta_{BU} = 90°$ and 130° (lower values)

23.8.2 Other Applications

The foreshock theory for radio emissions at f_p and $2f_p$ has numerous other applications in the solar system and in astrophysics. These include the foreshocks of other planets, mini-magnetospheres on the Moon, Mars, and the moons of other planets, the radio background of the interstellar medium, and emission from supernova shocks.

It is evident that the theory developed for Earth's foreshock can be generalized to any planet or moon with a bow shock. Kuncic and Cairns (2005) have performed these calculations for the planets, finding (Fig. 23.47) that Mercury is a particularly attractive target for observing foreshock radiation (e.g., with Bepi-Colombo). Similar figures for spacecraft at a fixed absolute distance from the planet's bow shock suggest that Jupiter should produce the largest flux, followed by Earth.

Localized and strong magnetic fields on moons can form a mini-magnetosphere and directly reflect the solar wind (or superalfvenic corotation flow within some planetary magnetospheres) – see Harnett and Winglee (2003) and references therein – and form a bow shock that then reflects electrons and give rise to radio emissions via the standard foreshock model (Kuncic and Cairns 2004). Figure 23.48 shows the foreshocks predicted for various orientations of the mini-magnetosphere to the solar wind for the Moon, with the shading proportional to the volume emissivity of radiation (Kuncic and Cairns 2004). Observable fluxes of radio emission are predicted for the Moon (Kuncic and Cairns 2004), perhaps accounting for some of the signals observed near f_p when the Wind spacecraft traversed the Moon's wake (Kellogg et al. 1996).

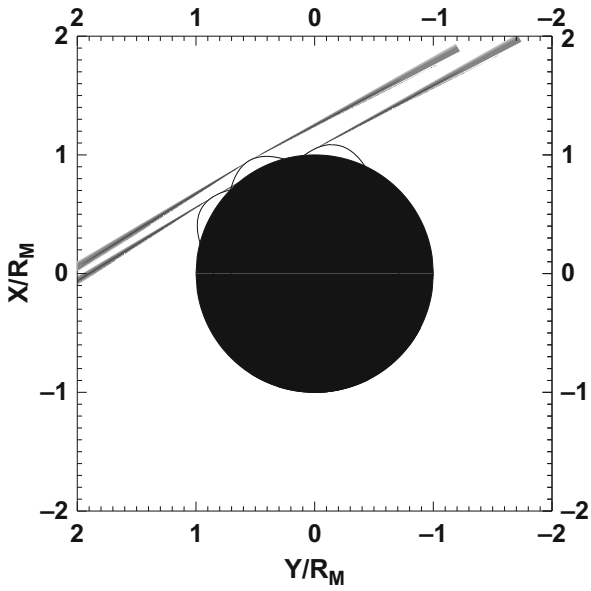

Fig. 23.48 Predicted volume emissivities and source regions for $2f_p$ radiation for three different locations of mini-magnetospheres (or magnetic anomalies) on the surface of the Moon when in the solar wind (Kuncic and Cairns 2004)

Similar situations may be applicable to moons in the Jovian or Saturnian magnetospheres (e.g., Ganymede) and to perturbations of the bow shocks of Mars and

Venus due to remnant magnetic fields. Further research is needed to quantify these ideas.

Finally, supernova shocks are a very attractive target for prediction of f_p and $2f_p$ radiation in a classic astrophysical context. Radiation over a broad frequency range can be expected when the shock overtakes ejecta from earlier periods of the star's evolution or reaches the system's termination shock and heliopause, since a broad range of densities is expected. It remains to be seen whether coherent foreshock emission will be predicted to have observable levels and whether it will be a significant contributor to the galactic background radiation at low frequencies $\lesssim 100$ kHz (Dulk et al. 2001; Hillan et al. 2010). Of course, emission from GMIR shocks for other stars, like the 2–3 kHz radiation for our Sun, may also be large contributors to the galactic background radiation, as commented in Section 23.7.4.

23.9 Concluding Remarks

Many powerful coherent radio emissions are associated with shocks in our solar system, from the deep corona to the solar wind to the outer heliosheath and perhaps the very local interstellar medium. All are produced near the electron plasma frequency f_{pe} and/or $2f_{pe}$. Emissions definitely driven by shocks include interplanetary type II bursts, radiation from Earth's foreshock, and rare emissions from CIRs. Emissions likely driven by shocks, but without definitive observational evidence, include drifting pulsating structures at GHz frequencies from the deep corona, coronal type II bursts, and the 2–3 kHz emissions from the outer heliosphere. Analogous emissions are also predicted, but not yet observed, from the foreshocks of the other planets (particularly Mercury and Jupiter, which are predicted to have the most easily observable emissions after Earth), mini-magnetospheres and associated bow shocks on the Moon and other moons that can move into the solar wind or exist in super-alfvenic, corotating, flows in planetary magnetospheres (e.g., Ganymede). Foreshock f_p and $2f_p$ radiation is also expected upstream of supernova shocks and also for the equivalent of GMIRs from other active stars, perhaps being a major contributor to the galactic background radiation at low frequencies $\lesssim 1$ MHz.

A detailed theory exists for foreshock f_p and $2f_p$ radiation, based on reflection and acceleration of electrons into the foreshock by the shock's magnetic mirror, the formation of electron beams (with loss cone features that can have many attributes of ring-beam distributions) in the foreshock due to imposition of a minimum parallel velocity to reach a given foreshock location by two effects (one imposed at the shock and one by time-of-flight effects) that typically coincide, the generation of intense electrostatic Langmuir waves by the electron beams, and the conversion of Langmuir energy into radiation by standard nonlinear processes involving Langmuir waves. This theory couples multiple physical processes from microscales to macroscales, with the foregoing processes being microscale physics, the creation of ripples on the shock with sizes of order the decorrelation length of the magnetic field and scattering of radiation by density irregularities being intermediate scale physics, while the macroscale physics includes 3D spatiotemporal variations of the plasma and the shock motion, as well as integration of emission from individual shock ripples over the entire shock.

This theory has been implemented analytically and numerically and applied in some detail to Earth's foreshock radiation, type II bursts, and the 2–3 kHz outer heliospheric radiation. The predictions appear to be in good qualitative and even semiquantitative agreement with available observations, explaining the electron properties well and typically accounting for the observed Langmuir fields and radiation fluxes to within a factor of 3–10.

A number of improvements and tests have been identified for the microphysics of the theory, such as including overshoots in the magnetic field and cross-shock potential for the electron reflection and beam formation, observational testing of the assumption of marginal stability and SGT for the waves, simulation-based testing of the energy transfer rate into the waves from the beams based on marginal stability, and incorporation of additional radiation mechanisms such as linear mode conversion and emission from Langmuir eigenstates and ILSs. The physics of ripple formation and evolution needs to be understood better, so as to better model the characteristic sizes and packing of ripples onto the macroscopic shock. Scattering and intrinsic directivity effects for the radiation are also acknowledged to be important and require inclusion. Another area requiring improvement is the modeling

of inhomogeneities of the background plasma (density, magnetic field, flow speed, temperatures, and the fraction and distribution function of nonthermal particles) and the 3D motion and location of the shock. Initial 2D models for the solar wind and high corona, driven by spacecraft data at 1 AU, exist but improvements have been identified. These types of data-driven models and accurate shock models are increasingly important for the modelling of type II bursts and the 2–3 kHz radiation, since the levels and frequency-time fine structures of the radiation are predicted to depends strongly on the local properties of the shock and plasma. Within the next few years it is believed that theory-data comparisons for type II bursts will be useful in constraining the properties of CME-driven shocks in the solar wind: these will allow prediction of whether, when, and with what properties a CME will impact Earth's magnetosphere and produce space weather events. Similarly, modelling a large-scale 3D GMIR shock interacting with realistic asymmetric models for the solar wind – LISM interaction may naturally explain the two classes and detailed properties of the 2–3 kHz outer heliospheric emission. It is recognized that major progress in testing the theory, and making associated refinements, will occur with the advent of reliable bolt-on versions of the foreshock theory that can be combined with advanced, data-driven, global simulations of both the background plasma and shock properties.

Unresolved theoretical and observational issues for type IIs, Earth's foreshock radiation, and the 2–3 kHz radiation are described in detail in Sections 23.5, 23.6.4, and 23.7.4. These include the one- versus two-shock debate for coronal and interplanetary type IIs, regarded here as of minor relevance (because the foreshock theory requires a shock but is agnostic as to its origin) although the evidence appears to favor a blast-shock for most metric type IIs and a CME-driven shock for almost all interplanetary type IIs. Others are the nature of the fine structures on type II bursts and the 2–3 kHz emissions, and the importance of scattering and propagation effects. Avenues to resolve these issues appear to exist and should be pursued. Resolving them may well lead to progress in understanding coronal structures and the interaction between the solar wind and VLISM, as well as the orientation and strength of the magnetic field in the VLISM.

Advanced ground-based instruments like the Frequency Agile Solar Radiotelescope (FASR), LOw Frequency ARray (LOFAR), and Murchison Widefield Array (MWA) will produce high dynamic range and high time- and frequency-resolution dynamic spectra, as well as images with higher time and angular resolution than before. In addition, the new Solar Dynamics Observatory spacecraft (SDO) and the existing Solar and Heliospheric Orbiting (SOHO), STEREO, and Wind spacecraft have excellent capabilities for observing many solar and interplanetary phenomena, including those related to type II bursts, CIR shocks, and Earth's foreshock radiation. The Voyager spacecraft continue to operate well and move towards the heliopause and the outer heliosheath, thereby being well poised to answer questions related to the origin of the 2–3 kHz radiation. Novel, high quality data will therefore be available to answer many unresolved issues raised in this review.

A major conclusion of this review is that the time is now ripe for making major progress on coherent radio emissions from shocks, since an attractive, apparently viable, and widely applicable theory exists, as do abundant high quality observational data. Put another way, a primary focus of current and future research should be on developing quantitative predictions of the theory, comparing these with observational data, and refining the theory as required. In this regard, quantitative testing and refining of the theory for Earth's foreshock should perhaps be of highest priority, due to the wealth of observational data on the electrons, Langmuir waves, radio emission and the solar wind properties, plus well-tested models for the location and basic properties of the bow shock.

In conclusion, it appears that the basic foreshock theory for radio emission from shocks (electron reflection and acceleration, development of electron beams, growth of Langmuir waves, and production of f_{pe} and $2f_{pe}$ radiation for a macroscopic, rippled, shock) appears likely to explain semiquantitatively the primary observations for the three best-observed and modelled applications, that many solar system radio emissions appear to be associated with shocks and qualitatively consistent with the basic theory, and that many observational details and theoretical limitations remain but do not appear likely to fundamentally alter the theory. The next 10 years ought to be an exciting time that sees theory and observations brought together quantitatively, and type II bursts and the 2–3 kHz radiation become important in predicting space weather at Earth and the impacts of solar activity on the local interstellar medium.

Acknowledgements The author thanks the Referee, colleagues D.S. Hillan, B. Li, V.V. Lobzin, and P.A. Robinson for constructive comments, Editors M.P. Miralles and J. Sanchez Almeida for patience and encouragement, and D.S. Hillan, S.A. Knock, and J.J. Mitchell for providing unpublished figures. Funding from the Australian Research Council is gratefully acknowledged.

References

Allen CW (1947) Interpretation of electron densities from corona brightness. Mon Not R Soc 107:426

Anderson RR, Parks GK, Eastman TE, Gurnett DA, Frank LA (1981) Plasma waves associated with energetic particles streaming into the solar wind from the Earth's bow shock. J Geophys Res 86:4493

Armstrong JW, Coles WA, Rickett BJ (2000) Radio wave scattering in the outer heliosphere. J Geophys Res 105:5149

Bale SD, Burgess D, Kellogg PJ, Goetz K, Monson SJ (1997) On the amplitude of intense Langmuir waves in the terrestrial electron foreshock. J Geophys Res 102:11281

Bale SD, Reiner MJ, Bougeret J-L (1999) The source region of an interplanetary type II radio burst. Geophys Res Lett 26:1573

Bale SD, Larson DE, Lin RP, Kellogg PJ, Goetz K, Monson SJ (2000) On the beam speed and wavenumber of intense electron plasma waves near the foreshock edge. J Geophys Res 105:27353

Ball L, Melrose DB (2001) Shock drift acceleration of electrons. Publ Astron Soc Aust 18:361

Bastian TS, Benz AO, Gary DE (1998) Radio emission from solar flares. Annu Rev Astron Astrophys 36:131

Bastian TS, Pick M, Kerdraon A, Maia D, Voulidas A (2001) The coronal mass ejection of 1998 April 20: direct imaging at radio wavelengths. Astrophys J 558:L65

Baumbach S (1937) Strahlung, ergiebigkeit und elektronendichte der sonnenkorena. Astron Nachr 263:131

Bougeret J-L, Goetz K et al (2008) S/Waves: the radio and plasma wave investigation on the STEREO mission. Space Sci. Rev 136:487

Budden KG (1985) The propagation of radio waves. Cambridge University Press, New York, NY

Burgess D (1995) Collisionless shocks. In: Kivelson MG, Russell CT (eds) Introduction to space physics. Cambridge University Press, New York, NY, p 129

Burgess D, Harvey CC, Steinberg J-L, Lacombe C (1987) Simultaneous observation of fundamental and second harmonic radio emission from the terrestrial foreshock. Nature 330:732

Cairns IH (1986a) The source of free energy for Type II solar radio bursts. Proc. Astron. Soc. Aust 6:444

Cairns IH (1986b) New waves at multiples of the plasma frequency upstreamof the Earth's bow shock. J Geophys Res 91:2975

Cairns IH (1987a) The electron distribution upstream from the Earth's bow shock. J Geophys Res 92:2315

Cairns IH (1987b) A theory for the Langmuir waves in the Earth's foreshock. J Geophys Res 92:2329

Cairns IH (1988) A semiquantitative theory for the $2f_p$ radiation observed upstreamfrom the Earth's bow shock. J Geophys Res 93:3958

Cairns IH (1994) Fine structure in plasma waves and radiation near the plasma frequency in Earth's foreshock. J Geophys Res 99:2975

Cairns IH (1995) Radio wave scattering in the outer heliosphere: Preliminary calculations. Geophys Res Lett 22:23433

Cairns IH (1996) On radio wave scattering in the outer heliosphere. In: Winterhalter D et al (eds) "Solar wind eight", AIP Conference Proceedings 382, p 582

Cairns IH (2000) Role of collective effects in dominance of scattering off thermal ions over Langmuir wave decay: analysis, simulations, and space applications. Phys Plasmas 7:4901

Cairns IH (2004) Radiation from the outer heliosphere and beyond. In: Poletto G, Suess S (eds) The sun and the heliosphere as an integrated system, Astrophysics and Space Science Library, vol 317. Kluwer, Dordrecht, p 65

Cairns IH, Fung SF (1988) Growth of electron plasma waves above and below the electron plasma frequency in the foreshock. J Geophys Res 93:7307

Cairns IH, Kaiser ML (2002) Solar system radio emissions. In Russ Stone W (ed) The review of radio science 1999–2002. IEEE Press, Piscataway, p 749

Cairns IH Knock SA (2006) Predictions for dynamic spectra and source regions of type II radio bursts in the inhomogeneous corona and solar wind. In: Rucker HO, Kurth WS, Mann G (eds) Planetary radio emissions VI proceedings. Verlag. Ost. Akad. Wissenschaften, p 419

Cairns IH, Melrose DB (1985) A theory for the $2\ f_p$ radiation upstream of the Earth's bow shock. J Geophys Res 90:6637

Cairns IH, Robinson RD (1987) Herringbone bursts associated with type II solar radio emission. Solar Phys 111:365

Cairns IH, Robinson PA (1995) Ion acoustic wave frequencies and onset times during type III solar radio bursts. Astrophys J 453:959

Cairns IH Robinson PA (1997) First test of stochastic growth theory for Langmuir waves in Earth's foreshock. Geophys Res Lett 24:369

Cairns IH, Robinson PA (1999) Strong evidence for stochastic growth theory of Langmuir-like waves in Earth's foreshock. Phys Res Lett 82:3066

Cairns IH, Robinson PA (2000) Roles played by electrostatic waves in producing radio emissions. In: Stone RG, Weiler KW et al (eds) Radio astronomy at long wavelengths, Geophysics Monograph Series 119. American Geophysical Union, Washington, DC, p 37

Cairns IH, Willes AJ (2005) Angle-averaged efficiencies for linear mode conversion between Langmuir waves and radiation in an unmagnetized plasma. Phys Plasmas 12:052315

Cairns IH Zank GP (2001) Theories for radio emissions from the outer heliosphere. In: Scherer K, Fichtner H et al (eds) The outer heliosphere: the next frontiers. Pergamon, Amsterdam, p 253

Cairns IH, Zank GP (2002) Turn-on of 2–3 kHz radiation beyond the heliopause. Geophys Res Lett 29, 2001GL014112

Cairns IH, Robinson PA, Anderson RR (2000) Thermal and driven stochastic growth of Langmuir-likewaves in the solar wind and Earth's foreshock. Geophys Res Lett 27:61

Cairns IH, Kurth WS, Gurnett DA (1992) The outer heliospheric radio emissions: (2) Foreshock source models. J Geophys Res 97:6245

Cairns IH, Knock SA, Robinson PA, Kuncic Z (2003) Type II solar radio bursts: theory and space weather implications. Space Sci Rev 107:27

Cairns IH, Mitchell JJ, Knock SA, Robinson PA (2004) Towards a quantitative theory for 2–3 kHz emission from beyond the heliopause. Adv Space Res 34(1):88

Cairns IH, Mitchell JJ, Pogorelov N, Zank GP (2006) Magnetic draping, 2–3 kHz radio emissions, and constraints on the interstellar magnetic field. In: AIP Conference Proceedings 858, p 329

Cairns IH, Robinson PA, Anderson RR, Strangeway RG (1997) Foreshock Langmuir waves for unusually constant solar wind conditions: data and implications for foreshock structure. J Geophys Res 102:24249

Cane HV, Erickson WC (2005) Solar type II radio bursts and IP type II events. Astrophys J 623:1180

Cane HV, Stone RG (1984) Type II solar radio bursts, interplanetary shocks, and energetic particle events. Astrophys J 282:339

Cane HV, Sheeley NR Jr, Howard RA (1987) Energetic interplanetary shocks, radio emission, and coronal mass ejections. J Geophys Res 92:9869

Cane HV, Stone RG, Fainberg J, Stewart RT, Steinberg J-L, Hoang S (1981) Radio evidence for shock acceleration of electrons in the solar corona. Geophys Res Lett 8:1285

Cane HV, Stone RG, Fainberg J, Steinberg J-L, Hoang, S (1982) Type II solar radio events observed in the interplanetary medium. I - General characteristics. Solar Phys 78:187

Cane HV, Erickson WC, Prestage NP (2003) Solar flares, type III radio bursts, coronal mass ejections, and energetic particles. J Geophys Res 107:2001JA000320

Cliver EW, Webb DF, Howard RA (1999) On the origin of solar metric type II bursts. Solar Phys 187:89

Cliver EW, Kahler SW, Reames DV (2004) Coronal shocks and solar energetic proton events Astrophys J 605:902

Collier MR, Szabo A, Slavin JA, Lepping RP (2000) IMF length scales and predictability: the two length scale medium. Int J Geopmag Aeron 2:3

Dulk GA, Erickson WC, Manning R, Bougeret J-L (2001) Calibration of lowfrequency radio telescopes using the galactic background radiation. Astron Astrophys 365:294

Dulk GA, Leblanc Y, Robinson PA, Bougeret J-L, Lin RP (1998) Electron beams and radio waves of solar type III bursts. J Geophys Res 103:17223

Dunckel N (1974) Low frequency radio emissions from the Earth and Sun. PhD thesis, Stanford University, Palo Alto

Ergun RE, Malaspina DM, Cairns IH et al (2008) Eigenmode structure in solarwind Langmuir waves. Phys Rev Lett 101:051101

Farrell WM (2001) Direct generation of o-mode emission in a dense, warm plasma: applications to interplanetary type II emissions and others in its class. J Geophys Res 106:15701

Feldman WC, Anderson RC, Bame SJ, Gary SP, Gosling JT et al (1983) Electron velocity distributions near the Earth's bow shock. J Geophys Res 88:96

Filbert PC, Kellogg PJ (1979) Electrostatic noise at the plasma frequency beyond the Earth's bow shock. J Geophys Res 84:1369

Fitzenreiter RJ, Scudder JD, Klimas AJ (1984) Detection of bump-on-tail electron reduced electron velocity distributions at the electron foreshock boundary. Geophys Res Lett 11:496

Fitzenreiter RJ, Scudder JD, Klimas AJ (1990) Three dimensional analyticmodel for the spatial variation of the foreshock electron distribution: Systematics and comparisons with ISEE observations. J Geophys Res 95:4155

Fitzenreiter RJ, Ogilvie KW, Bale SD, Vinas AF (2003) Modification of the solar wind electron velocity distribution at interplanetary shocks. J Geophys Res 108:1415

Florens MSL, Cairns IH, Knock SA, Robinson PA (2007) Data-driven solar wind model and prediction of type II bursts. Geophys Res Lett 34:L04104

Forslund DW, Kindel JM, Lee K, Lindman EL, Morse RL (1975) Theory and simulation of resonant absorption in a hot plasma. Phys Rev A 11:679

Frisch PC (2003) Boundary conditions of the heliosphere. J Geophys Res 108(10):LIS 11-1

Goldman MV, Reiter GF, Nicholson DR (1980) Radiation from a strongly turbulent plasma: Application to electron beam-excited solar emissions. Phys Fluids 23:388

Gopalswamy, N (2006) Coronal mass ejections and Type II radio bursts. In: Gopalswamy N, Mewaldt R, Torsti J (eds) Solar eruptions and energetic particles, AGU Monograph Series 165, p 207

Gopalswamy N, Kaiser ML, Thompson BJ, Burlaga LF et al (2000) Radio-rich solar eruptive events. Geophys Res Lett 27:1427

Gopalswamy N, Yashiro S, Kaiser ML., Howard RA, Bougeret J-L (2001) Radio signatures of coronal mass ejection interaction: coronal mass ejection cannibalism? Astrophys J 548:L91

Gopalswamy N, Yashiro S, Kaiser ML, Howard RA, Bougeret J-L (2001) Characteristics of coronalmass ejections associated with long-wavelength type II radio bursts. J Geophys Res 106:29219

Gopalswamy N, Yashiro S, Kaiser ML., Howard RA, Bougeret J-L (2002) Interplanetary radio emission due to interaction between two coronal mass ejections. Geophys Res Lett 29:106

Gopalswamy N, Yashiro S, Xie H, Akiyama S, Aguilar-Rodriguez E et al (2008) Radio-quiet fast and wide coronal mass ejections. Astrophys J 674:560

Grognard RJ-M (1985) Propagation of electron streams. In: McLean DJ, Labrum NR (eds) Solar radiophysics, Cambridge University Press, Cambridge, New York, p 173

Grzedzielski S, Lazarus AJ (1993) 2- to 3-kHz continuum emissions as possible indications of global heliospheric breathing. J Geophys Res 98:5551

Gurnett DA (1975) The Earth as a radio source: the non-thermal continuum. J Geophys Res 80:2751

Gurnett DA (1995) Heliospheric radio emissions. Space Sci Rev 72:243

Gurnett DA, Kurth WS (1995) Heliospheric 2–3 kHz radio emissions and their relationship to large Forbush decreases. Adv Space Res 16(9):279

Gurnett DA, Kurth WS (1996) Radio emissions from the outer heliosphere. Space Sci Rev 78:53

Gurnett DA, Allendorf SC, Kurth, WS (1998) Direction-findingmeasurements of heliospheric 2–3 kHz radio emissions. Geophys Res Lett 25:4433

Gurnett DA, Kurth WS, Allendorf SC, Poynter RL (1993) Radio emission from the heliopause triggered by an interplanetary shock. Science 262:199

Gurnett DA, Kurth WS, Cairns IH, Mitchell JJ (2006) The local interstellar magnetic field direction from direction-fnding measurements of heliospheric 2–3 kHz radio emissions. In: AIP conference proceedings 858, 129

Harnett EM, Winglee, R (2003) 2.5D fluid simulations of the solar wind interacting with multiple dipoles on the surface of the Moon. J Geophys Res 108(A2):1088

Heerikhuisen J, Pogorelov NV, Zank GP, Crew GB, Frisch PC et al (2010) Pickup ions in the outer heliosheath: a possible mechanism for the Intestellar Boundary Explorer ribbon. Astrophys J Lett 708:L126 [Erratum 710, L172 (2010)]

Hellinger P, Travnicek P, Matsumoto, H (2002) Reformation of perpendicular shocks: hybrid simulations. Geophys Res Lett 29:2234

Hellinger P, Travnicek P, Lembege B, Savoini P (2007) Emission of nonlinear whistler waves at the front of perpendicular supercritical shocks: hybrid versus full particle simulations. Geophys Res Lett 34:L14109

Henri P, Briand C, Mangeney A, Bale SD, Califano F, Goetz K, and Kaiser ML (2009) Evidence for wave coupling in type III emissions. J Geophys Res 114:A03103

Hillan DS, Cairns IH, Robinson PA, Mohamed A (2010) Prediction of background levels for the Wind/WAVES instrument and implications for the galactic background radiation. J Geophys Res 115:A061012

Hoang S, Fainberg J, Steinberg J-L, Stone RG, Zwickl RH (1981) The 2 f_p circumterrestrial radio emission as seen from ISEE 3. J Geophys Res 86:4531

Hoang S, Pantellini F, Harvey CC, Lacombe C, Mangeney A et al (1992) Interplanetary fast shock diagnosis with the radio receiver on Ulysses. In: Marsch E, Schwenn R (eds) Solar wind seven, 465. COSPAR Colloquium series 3

Hoang S, Lacombe C, MacDowall RJ, Thejappa, G (2007) Radio tracking of the interplanetary coronal mass ejection driven shock crossed by Ulysses on 10 May 2001. J Geophys Res 112:A09102

Holman GD, Pesses ME (1983) Solar type II radio emission and the shock drift acceleration of electrons. Astrophys J 267:837

Hull AJ, Scudder JD, Frank LA, Paterson WR, Kivelson MG (1998) Electron heating and phase space signatures at strong and weak quasi-perpendicular shocks. J Geophys Res 103:2041

Hull AJ, Scudder JD, Fitzenreiter RJ, Ogilvie KW, Newbury JA et al (2000) Electron temperature and de Hoffman - Teller potential change across the Earth's bow shock: new results from ISEE 1. J Geophys Res 105:20,957

Izmodenov VV (2004) The heliospheric interface: models and observations. In: Poletto G, Suess S (eds) The sun and the heliosphere as an integrated system, Astrophysics and Space Science Library, vol 317. Kluwer, Dordrecht, p 23

Karlicky M (2003) High-frequency radio signatures of solar-eruptive flares. Space Sci Rev 107:81

Karlicky M, Barta M (2004) Diagnostics of solar flare reconnection. Nonlin Proc Geophys 11:471

Kasaba Y, Matsumoto H, Omura Y, Anderson RR, Mukai T et al (2000) Statistical studies of plasma waves and Backstreaming electrons in the terrestrial electron foreshock observed by Geotail. J Geophys Res 105:79

Kellogg PJ (2003) Langmuir waves associated with collisionless shocks: a review. Planet Space Sci 51:681

Kellogg PJ, Goetz K, Monson SJ, Bougeret J-L, Manning R, Kaiser ML (1996) Observations of plasma waves during a traversal of the Moon's wake. Geophys Res Lett 23:1267

Kennel CF, Edmiston JP, Hada, T (1985) A quarter century of collisionless shock research. In: Stone RG, Tsurutani BT (eds) Collisionless shocks in the heliosphere: a tutorial review, , Geophysical Monograph 34, p 1

Khan J, Aurass H (2002) X-ray observations of a large-scale solar coronal shock wave. Astron Astrophys 383:1018

Kim, E-H, Cairns IH, Robinson PA (2007) Extraordinary-mode radiation produced by linear-mode conversion of Langmuir-waves. Phys Rev Lett 99:015003

Kim, E-H, Cairns IH, Robinson PA (2008) Mode conversion of Langmuir to electromagnetic waves at magnetic field-aligned density inhomogeneities: simulations, theory, and applications to the solar wind and corona. Phys Plasmas 15:102110

Klassen A Aurass H, Klein K-L, Hofmann A, Mann G (1999) Radio evidence on shock wave formation in the solar corona. Astron Astrophys 343:287

Kliem B, Krueger A, Treumann RA (1992) Third plasma harmonic radiation in type II bursts. Solar Phys 140:149

Klimas AJ, Fitzenreiter RJ (1988) On the persistence of unstable bump-on-tail electron velocity distributions in the Earth's foreshock. J Geophys Res 93:9628

Knock SA, Cairns IH (2005) Type II radio emission predictions: Sources of coronal and interplanetary spectral structure. J Geophys Res 110:A01101

Knock SA, Cairns IH, Robinson PA, Kuncic Z (2001) Theory of type II solar radio emission from the foreshock region of an interplanetary shock. J Geophys Res 106:25041

Knock SA, Cairns IH, Robinson PA, and Kuncic,Z Theoretically predicted properties of type II radio emission from an interplanetary foreshock. J. Geophys. Res 108, 2002JA009508 (2003a)

Knock SA, Cairns IH, Robinson PA (2003b) Type II radio emission predictions: multiple shock ripples and dynamic spectra. J Geophys Res 108, 2003JA009960

Krasnoselskikh VV, Lembege B, Savoini P, Lobzin VV (2002) Nonstationarity of strong collisionless shocks: theory and full particle numerical simulations. Phys Plasmas 9:1192

Krasnoselskikh VV Lobzin VV, Musatenko K, Soucek J, Pickett JS, Cairns IH (2007) Beam-plasma interaction in randomly inhomogeneous plasmas and statistical properties of small-amplitude Langmuir waves in the solar wind and electron foreshock. J Geophys Res 112:A10109.

Kuncic Z, Cairns IH (2004) Radio emission from mini-magnetospheres on the Moon. Geophys Res Lett 31:L11809

Kuncic Z, Cairns IH (2005) Planetary foreshock radio emissions. J Geophys Res 110:A07107

Kuncic Z, Cairns IH, Knock S, Robinson PA (2002) A quantitative theory for terrestrial foreshock radio emissions. Geophys Res Lett 29:1161

Kuncic Z, Cairns IH, Knock S (2002) Analytic model for the electrostatic potential jump across collisionless shocks, with application to Earth's bow shock. J Geophys Res 107:1218

Kuncic Z, Cairns IH, Knock S (2004) A quantitative theory for terrestrial foreshock radio emissions: 1. Predicted properties. J Geophys Res Lett 109:A02108

Kurth WS, Gurnett DA (2003) On the source location of low-frequency heliospheric radio emissions. J Geophys Res 108(10):LIS 2-1

Kurth WS, Gurnett DA, Scarf FL, Poynter RL (1984) Detection of a radio emission at 3 kHz in the outer heliosphere. Nature 312:27

Kurth WS, Gurnett DA, Scarf FL, Poynter RL (1987) Long-period dynamic spectrograms of low-frequency interplanetary radio emissions. Geophys Res Lett 14:49

Lacombe C, Harvey CC, Hoang S, Manganey A, Steinberg J-L, Burgess D (1988) ISEE observations of radiation at twice the solar wind plasma frequency, Ann. Geophys 6:113

Leblanc Y, Dulk GA, Cairns IH, Bougeret J-L (2000) Type II-flare continuum in the corona and solar wind. J Geophys Res 105:18215

Lembege B, Dawson JM (1987) Self-consistent study of a perpendicular collisionless and nonresistive shock. Phys Fluids 30:1767

Lembege B et al (2004) Selected problems in collisionless shock physics. Space Sci Rev 110:161

Lembege B, Savoini P, Hellinger P, Travnicek PM (2009) Nonstationarity of a two-dimensional perpendicular shock: competingmechanisms. J Geophys Res 114:A03217

Leroy M, Winske D, Goodrich CC (1982) The structure of perpendicular bow shocks. J Geophys Res 87:5081

Li B, Cairns IH, Robinson PA (2008a) Simulations of coronal type III solar radio bursts: 1. Simulation model. J Geophys Res 113:A06104

Li B, Cairns IH, Robinson PA (2008b) Simulations of coronal type III solar radio bursts: 2. Dynamic spectrum for typeical parameters. J Geophys Res 113:A06105

Li B, Cairns IH, Robinson PA (2010) Imprints of coronal temperature disturbances on type III bursts. Astron Astrophys 510:L6

Lobzin VV, Cairns IH, Robinson PA (2008) Evidence for wind-like regions, acceleration of shocks in the deep corona, and relevance of 1/f dynamic spectra to coronal type II bursts. Astrophys J Letts 677:L129

Lobzin VV, Krasnoselskikh VV, Schwartz S, Cairns IH, Lefbvre B, Decreau P (2005) Generation of downshifted oscillations in the electron foreshock: a loss-cone instability. Geophys Res Lett 32(18):L18101

Lobzin VV, Krasnoselskikh VV, Bosqued JM et al (2007) Nonstationarity and reformation of high-Mach-number Quasiperpendicular shocks: Cluster observations. Geophys Res Lett 34:L05107

Lobzin VV, Cairns IH, Robinson PA, Steward G, Patterson G (2009) Automatic recognition of type III solar radio bursts: themethod and first observations. Space Weather 7:S04002

Lobzin VV, Cairns IH, Robinson PA, Steward G, Patterson G (2010) Automatic recognition of coronal type II radio bursts: the automated radio burst identification system method and first observations. Astrophys J Lett 710:L58

Macek WM, Cairns IH, Kurth WS, Gurnett DA (1991) Plasma wave generation near the inner heliospheric shock. Geophys Res Lett 18:357

MacDowall RJ (1989) Effects of interplanetary shocks on kilometric type III radio bursts. Geophys Res Lett 16:923

Maia D, Pick M, Vourlidas A, Howard RA (2000) Development of coronal mass ejections: radio shock signatures. Astrophys J 528:L49

Malaspina DM, Ergun RE (2008) Observations of three-dimensional Langmuir wave structure. J Geophys Res 113:A12108

Malaspina DM, Li B, Cairns IH, Robinson PA, Ergun RE (2009) Terrestrial foreshock Langmuir waves: STEREO observations, theoretical modelling, and quasi-linear simulations. J Geophys Res 114:A12101

Malaspina DM, Cairns IH, Ergun RE (2010) The 2fp radiation from localized Langmuir waves. J Geophys Res 115:A01101

Mancuso S (2007) Coronal transients and metric type II radio bursts II. Accelerations at low coronal heights. Astron Astrophys 463:1137

Mancuso S, Raymond JC (2004) Coronal transients and metric type II radio bursts I. Effects of geometry. Astron Astrophys 413:363

Mann G, Klassen A, Aurass H, Classen HT (2003) Development of shock waves in the solar corona and the interplanetary space. Astron Astrophys 400:329

Mann G, Aurass H, Klassen A, Estel C, Thompson BJ (1999) Coronal transient waves and coronal shock waves. In: Vial J-C, Kaldeich-Schmann B (eds) 8th SOHO workshop: plasma dynamics and diagnostics in the solar transition region and corona, ESA Special Publication 446, p 477

Matsukiyo S, Scholer M (2006) On microinstabilities in the foot of high Mach number perpendicular shocks. J Geophys Res 111:A06104

McBride JB, Ott E, Boris JP, Orens JH (1972) Theory and simulation of turbulent heating by the modified two-stream instability. Phys Fluids 15:2367

McComas DJ, Allegrini F, Bochsler P, Bzowski M, Christian ER et al (2009) Global observations of the interstellar interaction from the interstellar boundary explorer (IBEX). Science 326:959

McClements KG, Bingham R, Su JJ, Dawson JM, Spicer DS (1993) Lower hybrid resonance acceleration of electrons and ions in solar flares and the associated microwave emission. Astrophys J 409:465

McLean DJ (1967) Band splitting in type II solar radio bursts. Proc Astron Soc Aust 12:401

McNutt RL Jr (1988) A solar-wind 'trigger' for the outer heliosphere radio emissions and the distance to the terminal shock. Geophys Res Lett 15:1307

Mel'nik VN, Konovalenko AA, Rucker HO, Stanislavsky AA, Abranin EP et al (2004) Observations of solar Type II bursts at frequencies 10–30 MHz. Solar Phys 222:151

Melrose DB (1980) The emission mechanisms for solar radio bursts. Space Sci Rev 26:3

Melrose DB (1985) Instabilities in space and laboratory plasmas. Cambridge University Press, Cambridge, New York

Mitchell JJ, Cairns IH, Robinson, PA (2004) Theory for 2–3 kHz radiation from the outer heliosphere. J Geophys Res 109:A06108

Mitchell JJ, Cairns IH, Heerikhuisen, J (2009) Pick-up ions and the 2–3 kHz radio emissions, Geophys Res Lett 36: L12109

Mitchell JJ, Cairns IH, Muller H-R, Zank GP (2005) Prediction of the timing of the 2–3 kHz radio emission within the solar cycle. Geophys Res Lett 32(7):L07101

Mitchell JJ, Cairns IH, Pogorelov, N, Zank GP (2008) Draping of the local interstellar mediummagnetic field over the heliopause. J Geophys Res 113:A04102

Moreton GE (1960) Hα observations of flare-initiated disturbances with velocities 1000 km/sec. Astron J 65:494

Moses D, Clette F, Delaboudineiere JP, Artzner GE et al (1997) EIT observations of the extreme ultraviolet Sun. Solar Phys 175:571

Narukage N, Hudson HS, Morimoto T, Akiyama S et al (2002) Simultaneous observation of aMoreton wave on 3 November 1997 in Hα and soft X-rays. Astrophys J 572:L109

Nelson GJ, Melrose DB (1985) Type II bursts. In: McLean, Labrum NR (eds) Solar radiophysics, Cambridge University Press, Cambridge, New York, p 333

Neugebauer M, Giacalone J (2005) Multispacecraft observations of interplanetary shocks: nonplanarity and energetic particles. J Geophys Res 110:A12106

Nulsen AL, Cairns IH, Robinson PA (2007) Statistics and shape of Langmuir wave packets observed by Ulysses in an interplanetary type III radio source. J Geophys Res 112:A05107

Omelchenko YA, Sagdeev RA, Shapiro VD, Shevchenko VI (1989) Numerical simulation of quasilinear relaxation of an ion ring and production of superthermal electrons. Sov J Plasma Phys 15:427

Onsager TG, Holzworth RH, Koons HC, Bauer OH, and Gurnett DA (1989) High-frequency electrostatic waves near Earth's bow shock. J Geophys Res 94:13397

Opher M, Alouani Bibi F, Toth G, Richardson JD, Izmodenov VV, Gombosi TI (2009a) A strong, highly-tilted interstellar magnetic field near the solar system. Nature 462:1036

Opitz A, Karrer R, Wurz P, Galvin AB et al (2009b) Temporal evolution of the solar wind bulk velocity at solar minimum by correlating the STEREO A and B PLASTIC measurements. Solar Phys 256:365

Papadopoulos KD, Freund HP (1978) Solitons and second harmonic radiation in type III bursts. Geophys Res Lett 5:881

Pogorelov NV, Heerikhuisen J, Mitchell JJ, Cairns IH, Zank GP (2009) Heliospheric asymmetries under strong interstellar magnetic field conditions and their impact on the 2–3 kHz radio emission. Astrophys J 695:L31

Prestage N (1994) IPS Radio and Space Services Technical Report TR-94-01, IPS, Haymarket

Pulupa M, Bale SD (2008) Structure on interplanetary shock fronts: type II radio burst source regions. Astrophys J 676:1330

Reiner MJ (2000) Interplanetary type II radio emissions associated with CMEs. In: Stone RG, Weiler KW et al (eds) Radio astronomy at long wavelengths, Geophysical Monograph Series 119. American Geophysical Union, Washington, DC, p 137

Reiner MJ, Kaiser ML (1999) High-frequency type II radio emissions associated with shocks driven by CMEs. J Geophys Res 104:16979

Reiner MJ, Kaiser ML, Bougeret J-L (2001) Radio signatures of the origin and propagation of coronal mass ejections from the solar corona and interplanetary medium. J Geophys Res 106:29989

Reiner MJ, Kasaba Y, Kaiser ML, Matsumoto H, Nagano I et al (1997) Terrestrial 2 f_p radio source Location determined from wind/Geotail triangulation. Geophys Res Lett 24:919

Reiner MJ, Kaiser ML, Fainberg J, Stone RG (1998) A new method for studying remote type II radio emission from coronal mass ejection-driven shocks. J Geophys Res 103:29651

Reiner MJ, Kaiser ML, Fainberg J, Bougeret J-L, Stone RG (1997) On the origin of radio emission associated with the January 6–11, 1997, CME. Geophys Res Lett 25:2493

Riddle AC (1974) On the observation of scattered radio emission from sources in the solar corona. Solar Phys 35:153

Roberts JA (1959) Solar radio bursts of spectral type II. Aust J Phys 11:215

Robinson PA (1995) Stochastic wave growth. Phys Plasmas 2:1466

Robinson PA (1997) Nonlinear wave collapse and strong turbulence. Rev Mod Phys 69:507

Robinson PA, Cairns IH (1995) Maximum Langmuir fields in planetary foreshocks determined from the electrostatic decay threshold. Geophys Res Lett 22:2657

Robinson PA, Cairns IH (1998) Fundamental and harmonic emission in type III solar radio bursts: 1. Emission at a single location or frequency. Solar Phys 181:363

Robinson PA, Cairns IH (2000) Theory of type III and type II solar radio emissions. In: Stone RG, Weiler KW et al (eds) Radio astronomy at longwavelengths, Geophysical Monograph Series 119. American Geophysical Union, Washington, DC, p 37

Robinson PA, Cairns IH, Gurnett DA (1993) Clumpy Langmuir waves in type III radio sources: Comparison of stochastic-growth theory with observations. Astrophys J 407:790

Robinson PA, Cairns IH, Willes AJ (1994) Dynamics and efficiency of type III radio emission. Astrophys J 422:870

Robinson PA, Li B, Cairns IH (2006) New regimes of stochastic wave growth: theory, simulation, and comparison with data. Phys Plasmas 13:112103

Rodriguez P, Gurnett DA (1975) Electrostatic and electromagnetic turbulence associated with the Earth's bow shock. J Geophys Res 80:19

Russell CT (1985) Planetary bow shocks. Collisionless shocks in the heliosphere: reviews of current research. American Geophysical Union, Washington, DC, p 109

Scherer K, Fahr HJ (2003) Solar cycle induced variations of the outer heliospheric structures. Geophys Res Lett 30(2):17–1

Schmidt JM, Gopalswamy N (2008) Synthetic radio maps of CME-driven shocks below 4 solar radii. J Geophys Res 113:A08104

Scholer M, Matsukiyo S (2004) Nonstationarity of quasi-perpendicular shocks: a comparison of full particle simulations with different ion to electron mass ratios. Ann Geophys 22:2345

Scudder JD, Mangeney A, Lacombe C, Harvey CC, Wu CS, Anderson RR (1986) The resolved layer of a collisionless, high β, supercritical, quasiperpendicular shock wave 3. Vlasov electrodynamics. J Geophys Res 91:11075

Shapiro VD, Bingham R, Dawson JM, Dobe Z et al (1998) Electron energization by lower-hybridwaves as a possible source for X-ray emission from comets. Phys Scr T75:39

Sigsbee K, Kletzing CA, Gurnett DA, Pickett JS et al (2004) The dependence of Langmuir wave amplitudes on position in Earth's foreshock. Geophys Res Lett 31:L07805

Smerd SF, Sheridan KV, Stewart RT (1974) On split-band structure in type II radio bursts from the Sun. In: Newkirk G (ed) Coronal disturbances: proceedings of the IAU symposium. Springer, New York, NY, p 389

Steinberg J-L, Hoang S, Dulk GA (1985) Evidence of scattering effects on the sizes of interplanetary type III radio bursts. Astron Astrophys 150:205

Stewart RT, Magun A (1980) Radio evidence for electron acceleration by transverse shock waves in herringbone type II solar radio bursts. Proc Astron Soc Aust 4(1):53

Stone EC, Cummings AC, McDonald FB, Heikkila BC et al (2005) Voyager 1 explores the termination shock region and the heliosheath beyond. Science 309:2017

Stone EC, Cummings AC, McDonald FB, Heikkila BC et al (2008) An asymmetric solar wind termination shock. Nature 454:71

Suzuki S, Dulk GA (1985) Bursts of type III and V. In: McLean DJ, Labrum NR (eds) Solar radiophysics. Cambridge University, Cambridge, New York, p 289

Thejappa G, Wentzel DG, MacDowall RJ, Stone RG (1995) Unusual wave phenomena near interplanetary shocks at high latitudes. Geophys Res Lett 22:3421

Thejappa G, MacDowall RJ, Kaiser ML (2007) Monte Carlo simulation of the directivity of interplanetary radio bursts. Astrophys J 671:894

Thompson BJ, Plunkett SP, Gurman JB, Newmark JS, St Cyr OC et al (1998) SOHO/EIT observations of an Earth-directed coronal mass ejection on 12 May 1997. Geophys Res Lett 25:2465

Tidman DA, Krall NA (1971) Shock waves in collisionless plasmas. Wiley-Interscience, New York, NY

Toptyghin IN (1980) Acceleration of particles by shocks in a cosmic plasma. Space Sci Rev 26:157

Uchida Y (1974) Behavior of the flare produced coronal MHD wavefront and the occurrence of type II radio bursts. Solar Phys 39:431

Vrsnak B, Cliver E (2008) Origin of coronal shock waves. Solar Phys 253:215

Vrsnak B, Magdalenic J, Aurass H, Mann G (2002) Band-splitting of coronal and interplanetary type II bursts: coronal magnetic field and Alfven velocity. Astron Astrophys 396:673

Wang SJ, Yan Y, Zhao RZ, Fu Q, Tan CM et al (2001) Broadband radio bursts and fine structures during the great solar event on 14 July 2000. Solar Phys 204:155

Warmuth A, Mann G (2005) The application of radio diagnostics to the study of the solar drivers of space weather. In: Scherer K, Fichtner H, Heber B, Mall U (eds) Space weather, Lecture Notes Phys. 656. Springer, p 51

Warmuth A, Vrsnak B, Magdalenic J, Hanslmeier A, Otruba W (2004a) A multiwavelength study of solar flare waves. I Observations and basic properties. Astron Astrophys 418:1101

Warmuth A, Vrsnak B, Magdalenic J, Hanslmeier A, Otruba W (2004b) A multiwavelength study of solar flare waves. II Perturbation characteristics and physical interpretation. Astron Astrophys 418:1117

Wild JP (1950) Observations of the spectrum of high-intensity solar radiation at meter wavelengths. Aust J Sci Res Ser A 3:399

Wild JP, McCready LL (1950) Observations of the spectrum of high-intensity solar radiation at metre wavelengths. I. The apparatus and spectral types of solar burst observed. Aust J Sci Res A 3:387

Wild JP, Smerd SF (1972) Radio bursts from the corona. Annu Rev Astron Astrophys 10:159

Wild JP, Smerd SF, Weiss AA (1963) Solar bursts. Annu Rev Astron Astrophys 1:291

Wu CS (1984) A fast fermi process: energetic electrons accelerated by a nearly perpendicular bow shock. J Geophys Res 89:8857

Wu CS, Lee LC (1979) A theory of terrestrial kilometric radiation. Astrophys J 230:621

Wu CS, Gaffey JD, Zhou GC (1985) Induced emission of radiation near $2\omega e$ by a synchrotron-maser instability. Phys Fluids 28:846

Yan Y, Deng Y, Karlicky M, Fu Q, Wang S, and Liu, Y (2001) The magnetic rope structure and associated energetic processes in the 2000 July 14 solar flare. Astrophys J 551:L115

Yin L, Ashour-Abdalla M, El-Alaoui M, Bosqued JM, and Bougeret J-L (1998) Generation of electromagnetic f_{pe} and $2\,f_{pe}$ waves in the Earth's electron foreshock via linear mode conversion. Geophys. Res Lett 25:2609

Yuan X, Cairns IH, Robinson PA (2007) Simulation of electron bursts upstream of reforming shocks. Astrophys J 671:439

Yuan X, Cairns IH, Robinson PA (2008a) Numerical simulations of electron distributions upstream and downstream of high Mach number quasi-perpendicular collisionless shocks. J Geophys Res 113:A08109

Yuan X, Cairns IH, Robinson PA, Kuncic Z (2007) Effects of overshoots on electron distributions upstream and downstream of quasiperpendicular collisionless Shocks. J Geophys Res 112:A05108

Yuan X, Cairns IH, Trichtchenko L, Rankin R (2008b) Effects of shock parameters on upstream energetic electron burst events. J Geophys Res 113:A09106

Yuan X, Cairns IH, Trichtchenko L, Rankin R, Danskin DW (2009) Confirmation of shock reformation in two-dimensional hybrid simulations. Geophys Res Lett 36:L05103

Zakharov VE (1972) Collapse of Langmuir waves. Sov Phys JETP, Engl Trans 35:908

Zank GP (1999) Interaction of the solar wind with the local interstellar medium: a theoretical perspective. Space Sci Rev 89(3/4):1

Zank GP, Muller H-R (2003) The dynamical heliosphere. J Geophys Res 108(A6):SSH7

Zank GP, Pauls HL,Williams LL, Hall DT (1996) Interaction of the solar wind with the local interstellar medium: a multifluid approach. J Geophys Res 101:21639